ABSTRACT

Title of thesis: ANALYSIS OF THE AERODYNAMICALLY DEPLOYABLE WINGS AND PAYLOAD SUPPORT STRUCTURE OF THE MONO TILTROTOR

John J. Samsock, Master of Science, 2007

Thesis directed by: Professor J. Gordon Leishman
Department of Aerospace Engineering

The Mono Tiltrotor (MTR) is a new vertical takeoff and landing (VTOL) rotorcraft concept. The premise of the MTR is a tilting coaxial rotor system for lifting and propulsion, along with aerodynamically deployable fixed-wings for long-range cruise. The symmetric and controlled self-deployment of these wings is a critical design feature of the MTR concept. A mathematical model was developed to predict the optimal wing hinge geometry to obtain satisfactory wing deployment. The wing hinge design was then used to design and build a functional model that was tested in the University of Maryland's Glenn L. Martin wind tunnel. The measurements showed that with suitable design features, the symmetric and controlled deployment of the wings are possible using aerodynamic actuation alone. The mathematical model has also been shown to be capable of predicting the dynamic, time-dependent behavior of the wings, as well as being able to predict the overall nonlinear lift, drag, and pitching moments on the MTR wing and tail configuration with good correlation to measured data. A finite element method (FEM)

model of the payload support structure was also developed to analyze forces, bending moments and displacements of the structure under load. Initial results show that significant bending moments will be present throughout the entire support structure. This FEM model can be incorporated into a full dynamic model of the MTR to study its dynamic behavior during flight maneuvers while carrying a payload.

ANALYSIS OF THE AERODYNAMICALLY DEPLOYABLE WINGS AND PAYLOAD SUPPORT STRUCTURE OF THE MONO TILTROTOR

by

John J. Samsock

Thesis submitted to the Faculty of the Graduate School of the
University of Maryland, College Park in partial fulfillment
of the requirements for the degree of
Master of Science
2007

Advisory Committee:

Professor J. Gordon Leishman, Chair/Advisor
Professor Roberto Celi
Professor James Baeder

DEDICATION

To my parents for their sacrifice, help and support in keeping me on the right path in pursuing a college education. To my friends who have helped me along the way.

ACKNOWLEDGMENTS

This work was supported through Baldwin Technology Company. I would like to acknowledge Mr. Douglas Baldwin, Dr. Manikandan Ramasamy, and Dr. Roberto Celi for their contributions made to this work. Dr. Celi helped me greatly in guiding me through the development of the dynamic mathematical model and also the FEM model. The wind tunnel model was constructed by Eagle Aircraft. Appreciation is extended to Dr. Jewel Barlow and the staff of the Glenn L. Martin wind tunnel for their support during the tests of the MTR model. Thanks Dr. Baeder for being part of my thesis committe. I would also like to thank Professor Leishman for all the help and guidance he has given to me over the course of this work and the opportunity to pursue a Masters degree in engineering.

Table of Contents

List of Figures

NOMENCLATURE

PRINCIPAL SYMBOLS

A	acceleration, $\mathrm{ft\,s^{-2}}$
A	cross sectional area, $\mathrm{in^2}$
c	chord length, ft
C_D	drag coefficient
C_L	lift coefficient
C_M	moment coefficient
D	drag, lb
E	modulus of elasticity, $\mathrm{lb\,in^{-2}}$
F	force, lb
G	modulus of rigidity, $\mathrm{lb\,in^{-2}}$
H	Hermite polynomial
I	FEM element moment of inertia, $\mathrm{in^4}$
I	inertia, $\mathrm{slug\,ft^2}$
J	polar moment of inertia, $\mathrm{in^4}$
K	FEM stiffness matrix
K	total number of sections
L	lift, lb
L_w	elemental width, ft
ℓ	length of FEM element, in
L_e	length, ft
M	moment, ft lb
M_A	elemental mass, slug
N	normal force, lb
N_T	normal and tangential forces matrix
p	roll rate, $\mathrm{rad\,s^{-1}}$
q	pitch rate, $\mathrm{rad\,s^{-1}}$
q_∞	dynamic pressure, $\mathrm{slug\,ft\,s^{-2}}$
r	yaw rate, $\mathrm{rad\,s^{-1}}$
R	position vector
S	transformation matrix
t	time, s
T	FEM transformation matrix
T	tangential force, lb
U	axial displacement, in
V	out-of-plane displacement, in
V	velocity, $\mathrm{ft\,s^{-1}}$
W	in-plane displacement, in
W	weight, lb
Y	distance along the y-axis of wing, ft
α	angle of attack, rad

β	tail section angle of incidence, rad
δ	wing twist, rad ft^{-1}
θ	rotation angle about y-axis, rad
Λ	wing sweep angle, rad
ρ	air density, slug ft^{-3}
ϕ	rotation angle about x-axis, rad
ϕ	torsional rotation, rad
ψ	rotation angle about z-axis, rad
Ω	angular velocity of a vector, rad s^{-1}

ABBREVIATIONS

CAD	Computer Aided Design
FEM	Finite Element Method
MTR	Mono Tiltrotor
PRM	Parametric Research Model
VTOL	Vertical Takeoff and Landing

SUBSCRIPTS

AC	aerodynamic center
B	body
BW	wing-to-body coordinates
CG	associated with gravity
$FRIC$	friction
G	global coordinate system
H	wing hinge
HT	tail-to-wing hinge coordinates
HW	wing-to-wing hinge coordinates
L	left side of element
LD	lift and drag forces
LG	global-to-local coordinates
PT	point on tail
PW	point on wing
R	right side of element
T	tail
TB	body-to-tail coordinates
TH	tail hinge
TOT	total
TW	wing-to-tail coordinates
T_1, T_2, T_3	tail sections 1,2 and 3, respectively
W	wing
WB	body-to-wing coordinates
WH	wing hinge-to-wing coordinates
WT	tail-to-wing coordinates
X	x-direction in coordinate system
Z	z-direction in coordinate system

Chapter 1

Introduction

The interest in developing heavy-lift rotorcraft concepts has spanned several decades [1, 2, 3, 4, 5]. Recently the U.S. Army has proposed requirements for a Future Transport Rotorcraft (FTR) that must be capable of carrying a 20 ton payload over a mission radius of 500 km (270 nm) under "hot and high" (95°F, 4,000 ft), conditions [6]. These are unprecedented ranges and payloads for a conventional helicopter, or even for a conventional tiltrotor. A vertical lift aircraft capable of meeting these requirements would increase the tatical capablility of any military by allowing them operations from small landing zones, yet transport more cargo over greater distances than conventional rotorcraft concepts.

A tiltrotor aircraft is ideal to meets these requirements, because of its ability to takeoff and land vertically but also be able to cruise with the much higher aerodynamic efficiencies that are associated with airplanes. Airplanes are more efficient than rotorcraft in cruise because of their much higher lift to drag (L/D) ratios. Helicopters tend to produce more drag, with a majority of it being as a result of the airframe, rotor hub and exposed rotor shaft. Airplanes can also fly faster and over longer ranges than helicopters. But, current VTOL aircraft lack the ability to take off and land vertically and hover with large heavy payloads for any significant amount of time. The thrust vectoring systems on VTOL aircraft tend to burn a

great deal of fuel, limiting aircraft range and hover time. Thus, an aircraft that has both the VTOL capabilities of a helicopter and the high cruise efficiencies of an airplane, is ideal.

(a)

(b)

Figure 1.1: Conceptual sketches of the MTR: (a) In hover with payload unit attached; (b) Forward flight with wings and tail fully deployed. (Images courtesy of Baldwin Technology Company.)

To meet these requirements, the Mono Tiltrotor (MTR), shown in Fig. 1.1, is a proposed innovative vertical takeoff and landing (VTOL) rotorcraft concept that integrates a tilting coaxial proprotor, aerodynamically deployable wings system, and a

suspended streamlined cargo handling unit. The MTR has been undergoing conceptual development over the past few years [6, 7]. The MTR design is characterized by a coaxial proprotor system that converts (tilts) from a lifter to a propulsor between vertical flight and forward flight modes. A lower disk loading and better power loading in comparison to current tiltrotors allows for efficient hovering capability. Using a coaxial rotor system, no tail rotor is required for anti-torque; roll, pitch, and yaw control is provided using cyclic and differential blade pitch control.

An aerodynamically deployable folding wing system is a key design feature of the MTR. Both the wings and tail fold down and rest vertically while in hover to minimize aerodynamic download. This is a key advantage for the MTR over current tiltrotor concepts, which all have large download penalties. Large download penalties lead to higher engine power requirements and lower payload capabilities. When the MTR is in the airplane configuration, the wings are deployed and locked into position. A relatively high aspect ratio wing allows for high efficiency in cruising flight and a higher L/D ratio than for a helicopter. Using solely aerodynamic forces to deploy the wings minimizes the weight that would be associated with any heavy mechanical actuation devices. In airplane mode, roll is controlled by conventional ailerons and pitch and yaw control is provided by the elevator and rudder on the tail, respectively. During wing deployment, the ailerons and flaps on each wing may be deployed to control the wing deployment rate, and also to ensure symmetric wing deployment.

For efficient payload deployment, the MTR utilizes a crane-type, aerodynamically streamlined suspended payload unit, which allows the aircraft to rapidly ac-

quire and deploy a diverse range of payloads that include standard MILVAN containers. Illustrations of the MTR with its payload unit attached are shown in hover and forward flight in Fig. 1.1. Note how the payload unit is fully encapsulated in a drag reducing fairing.

A series of sizing and performance studies have been conducted under prior research to evaluate the feasibility of the MTR design concept. The research focused on lift-to-drag estimation, wing sizing, mission parameter studies, and point optimization for long range missions. The research showed that the MTR can be designed to be capable of carrying 20 tons of payload over 1,000 nm. In comparison to the same requirements for a conventional helicopter the MTR concept is 50% smaller and 65% lighter [6]. However, this research assumes the technical feasibility of the coaxial tiltrotor, aerodynamically deployable wings, and the suspended payload unit.

The design methodology used was based upon a conceptual rotorcraft design code developed over several years at the University of Maryland [8]. The methodology uses as inputs the mission requirements and design parameters to converge on a solution for performance characteristics and weight breakdowns. A flow chart of the methodology is shown in Fig. 1.2. The weight breakdown is calculated based, in part, from historical weight data for rotorcraft and fixed-wing aircraft. For initial sizing estimates, the mission requirements that include payload weight, range, atmospheric conditions, and hover times are used, along with rotor and engine design inputs to perform initial aircraft sizing calculations. These initial estimates are fed into the equations that calculate power requirements and fuel efficiency to calculate

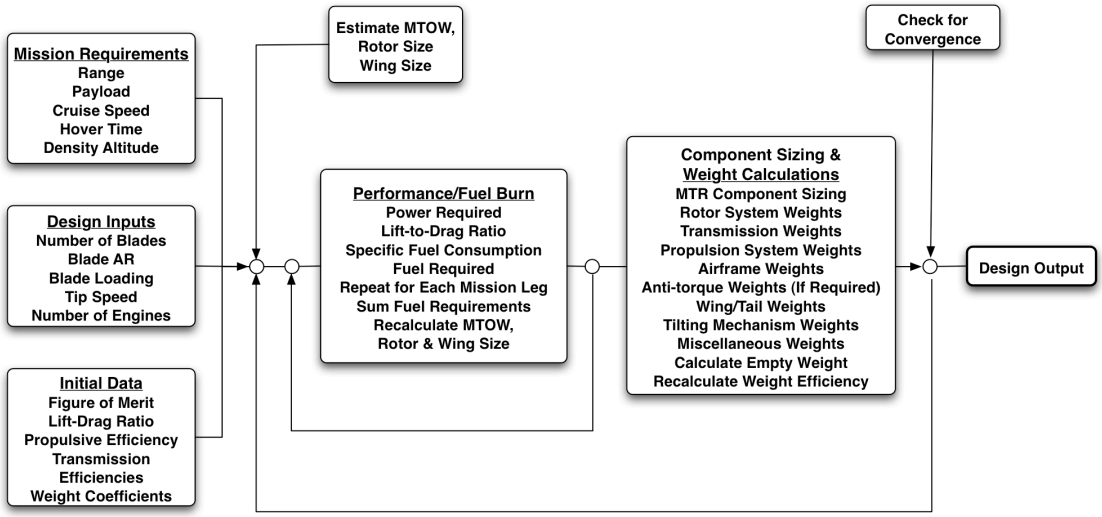

Figure 1.2: MTR flow chart methodology.

fuel burn. Fuel burn calculation is accomplished by iterating the initial sizing values until an aircraft size is acquired that matches the calculated fuel requirements. Once a convergence is reached on fuel burn, the initial sizing and performance results led to a detailed component weight breakdown. The total empty weight of the vehicle can then be calculated. This entire process is iterated until converging on a weight efficiency that matches the overall vehicle size and weight.

Three different mission profiles were studied [8]. Each mission profile can used to evaluate changes in parameters such as hover times, design cruise speed, density altitudes and flight range on each mission leg. The first mission profile corresponds to the MTR transporting a payload in a long range cruise. The second mission profile is for a radius of action mission as shown in Fig. 1.3, here the MTR transports a payload to a destination, hovers for sometime over the destination to deliver the payload and then returns with an optional payload unit attached. The third mission profile is where the MTR is in helicopter mode originally to fly to a

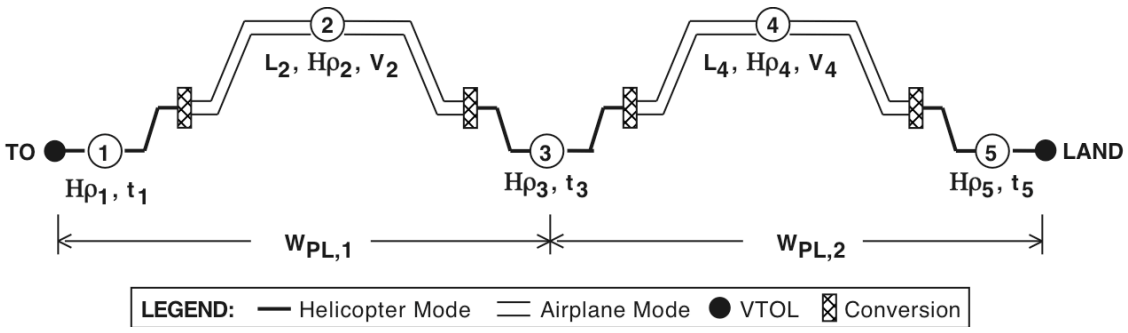

Figure 1.3: MTR radius of action mission profile.

destination to pick up a payload unit and then enters the airplane mode to deliver the payload unit to a destination.

An L/D estimation of the MTR is shown in Fig. 1.4, for both helicopter and airplane flight modes. These calculations were for a radius of action mission with the MTR carrying 20 tons of payload over 500 nm. It is shown that in helicopter mode the L/D is relatively low, as expected, and is comparable to conventional helicopters. In airplane flight modes however, L/D ratios as high as 14 can be obtained. This demonstrates the significant advantage the MTR over conventional rotorcraft concepts in terms of L/D ratio.

Figure 1.5 shows the empty weight of the MTR and hypothetical single and coaxial rotor helicopters required to travel 1,000 nm with a given payload. It is shown that the MTR's empty weight is up to 65% less that of a conventional helicopter concept for the same range and payload carrying requirements. The reason for this is that significantly less installed engine power is required for flight. This significant reduction in empty weight when compared to other rotorcraft concepts allows the MTR to have much higher payload and range capabilities then other rotorcraft concepts.

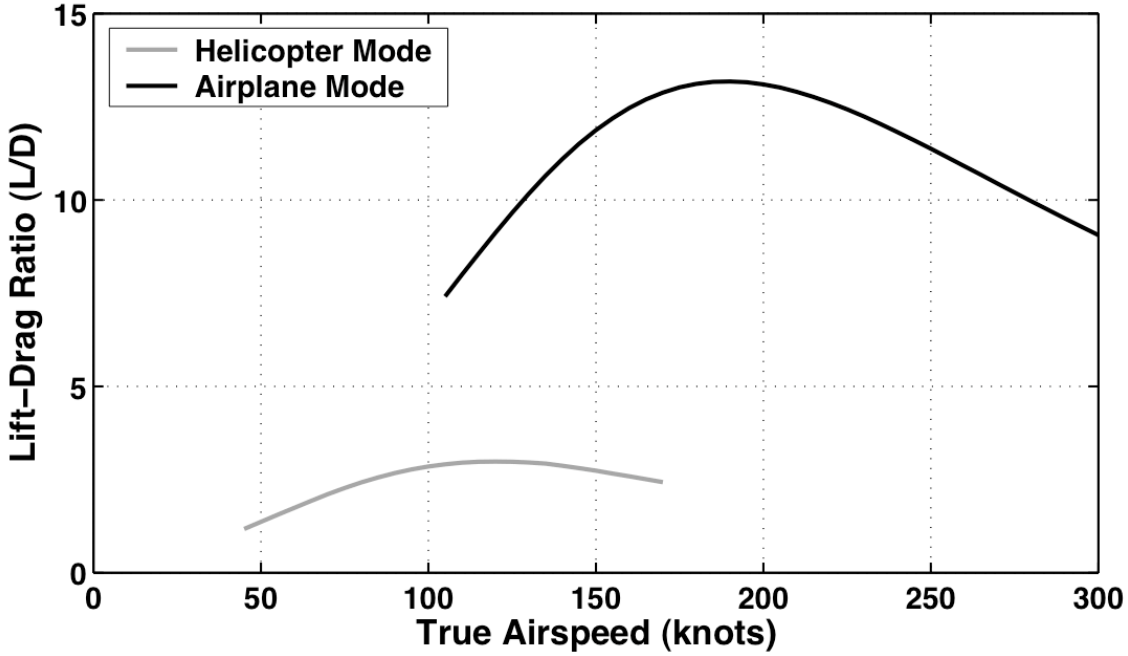

Figure 1.4: Lift-to-drag ratio of the MTR in helicopter and airplane flight modes.

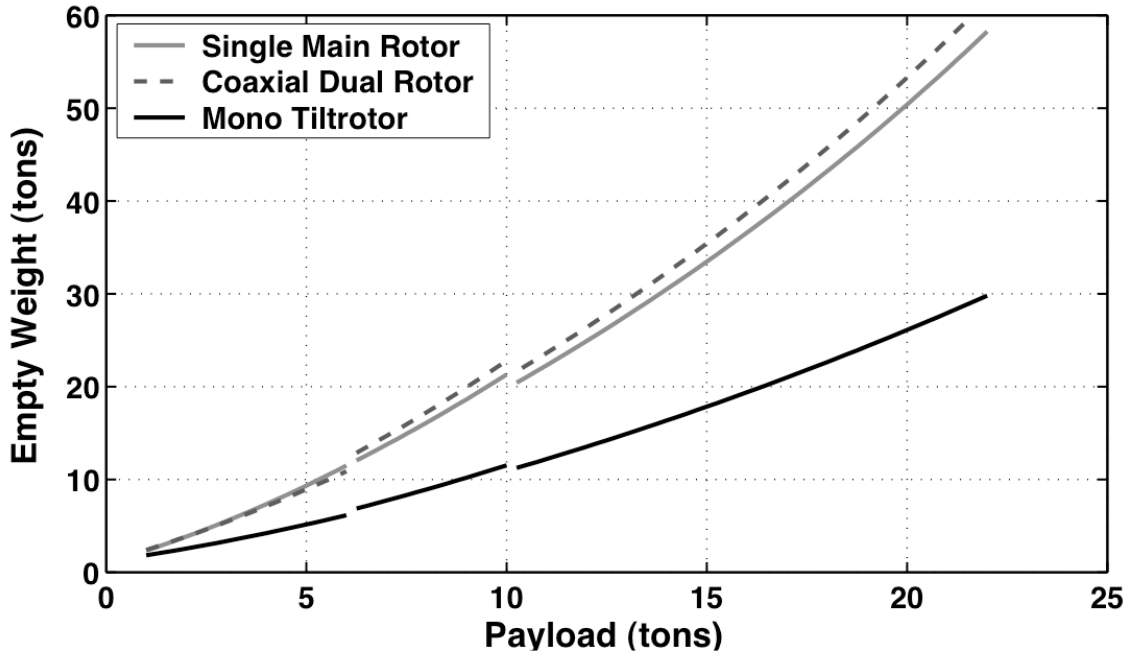

Figure 1.5: Predicted empty weight for the MTR to meet a 1,000 nm range requirement versus payload compared with hypothetical conventional (single) and coaxial rotor helicopters.

In part, the MTR also has a smaller empty weight because of its reduction in rotor size in comparison to conventional single and coaxial helicopters. Figure 1.6 shows the required rotor diameters of the MTR and hypothetical single and coaxial rotors required to carry a given payload a 1,000 nm range. Overall it is shown that the MTR's rotor can be up 50% smaller in diameter than a conventional helicopter design for the same payload and range carrying requirements.

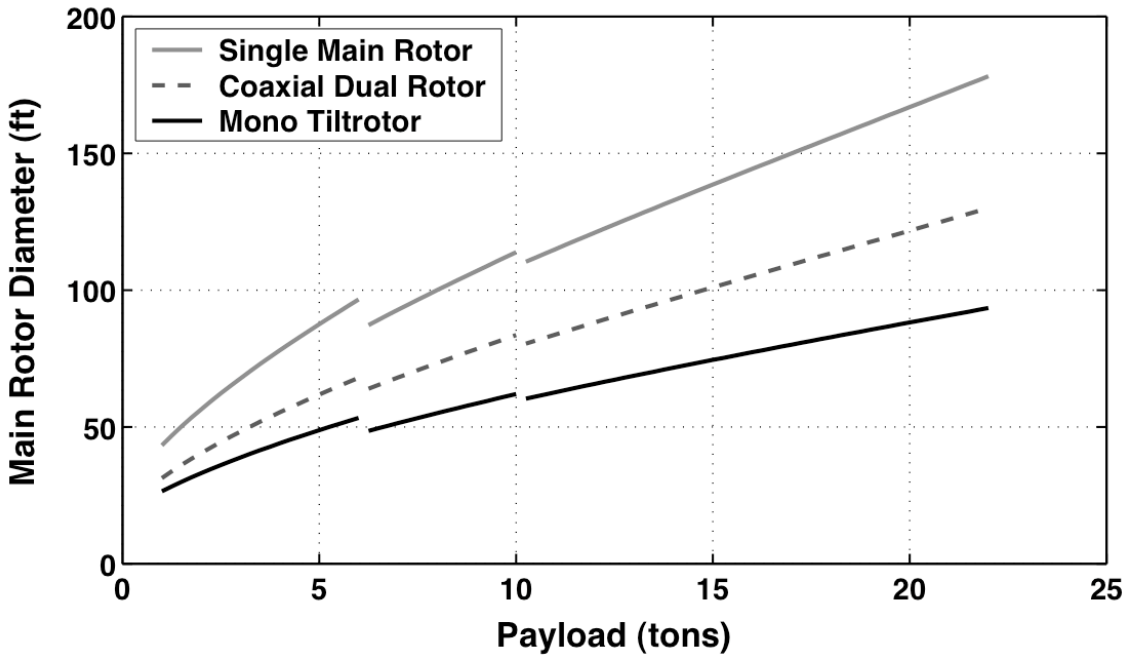

Figure 1.6: Predicted rotor size (diameter) for the MTR to meet a 1,000 nm range requirement versus hypothetical conventional (single) and coaxial rotor helicopters.

Figure 1.7 compares the payload versus range capabilities of the MTR and legacy helicopter designs. It is shown that current rotorcraft fall short of the payload versus range capabilities of the MTR. The MTR is shown to be capable of transporting 20 tons of payload over 1,000 nm, 27 tons of payload over 500 nm or 10 tons over 1,700 nm. Overall, it is shown that if technically realized the MTR will have unprecedented payload versus range capabilities over current rotorcraft.

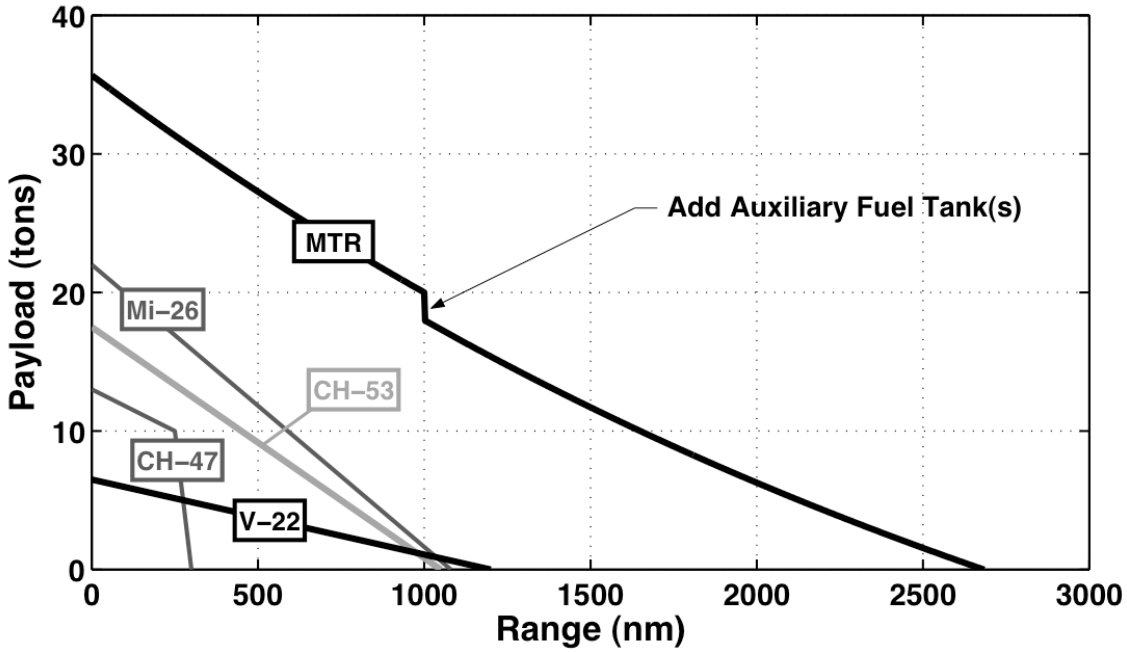

Figure 1.7: Predicted payload/range graph for the MTR concept when compared with legacy helicopter designs and to the V-22.

This makes the MTR an extremely valuable concept to consider for future rotorcraft technologies.

While the MTR concept has great potential, to be technically realized the aerodynamic deployment of the wings and transportation of a suspended payload at high flight speeds needs to be studied and demonstrated. The current work focused on these tasks. An overview of the present work covered in this thesis is as follows, first a mathematical model was developed to calculate kinematic and dynamic behavior of the wings. A comprehensive equilibrium analysis was conducted using the mathematical model to determine most likely wing hinge angles that would allow for aerodynamic wing deployment. A wind tunnel study was then accomplished to study aerodynamic wing deployment and measure lift, drag and moment forces on the MTR in various static configurations. The mathematical model was further

refined using data obtained in the wind tunnel study. The mathematical model showed good correlation between measured and predicted static forces, as well as for the dynamic behavior of the wings during deployment. This mathematical model may eventually be incorporated into a full dynamic model of the MTR.

An analysis on the payload support structure using finite element modeling (FEM) was also undertaken. The FEM analysis was required to analyze the suspended payload support structure under load to determine deformations and stresses. This FEM model may also be incorporated into a full dynamic model to analyze the MTR maneuvering while carrying a payload. There was concern that a torsional coupling effect may be present in the payload support structure which may lead to adverse flight characteristics. Therefore, in future work, this FEM model will be very beneficial in designing the payload support structure.

The specific objectives of the work reported in this thesis were:

1. To develop a suitable mathematical model with sufficient fidelity to faithfully describe the kinematic and dynamic behavior of the wings during deployment.

2. To successfully demonstrate through wind tunnel studies the controlled and repeatable wing deployment.

3. Using the mathematical model be capable of predicting the lift, drag and moments on the MTR in static flight configurations.

4. To create an FEM model of the payload support structure so it could be incorporated into a full dynamic model of the MTR.

Overall, controlled symmetric wing deployment was obtained and demonstrated in the wind tunnel study. The mathematical model was capable of calculating the static lift, drag and moment forces on the model and also the dynamic behavior of the wings during deployment with good correlation to measured data. The FEM model has been shown to be capable of predicting forces, moments and deformations within the payload support structure while under load.

Chapter 2
Mathematical Model

The previous chapter gave an introduction to the MTR concept and the significant design advantages of the MTR over current tiltrotor and rotorcraft designs. The current chapter describes the selection of a wing hinge design that would meet the geometric design requirements for the folding wings and tail. A majority of the chapter is dedicated to a description of the development of a mathematical model to be used to predict lift, drag and moments, as well as the dynamic behavior of the wings and tail during deployment.

2.1 Wing Hinge Design

The first step in the design process was to determine a kinematically suitable wing hinge geometry that would allow for the wings to rest vertically while in hover, yet allow the wings to be fully deployed when in forward flight. It was important that the wing hinge design be simple to save weight and minimize cost. It was noted that carrier-based WW2 aircraft used wing hinges to allow the wings to fold to conserve space. One plane in particular, the F-4F "Wild Cat" had a folding wing hinge that was similar to the design criteria. Figure 2.1 shows a photo of the F-4F with its wing folded and resting parallel to the fuselage of the aircraft. To investigate further this wing hinge design concept, a trip was taken to the National Air and Space Museum Paul E. Garber Restoration Facility where an F-4F is preserved. It was discovered that the F-4F uses a pin and collar type wing hinge that is canted outward

Figure 2.1: Photo of the F4-F Wildcat with wings in the folded position. (Photo courtesy of the Naval Historical Center.)

towards the wings and foward towards the nose of the aircraft. This pin and collar type joint could be incorporated for the present purposes. Hence, this wing hinge configuration was used as a starting point in the development of a mathematical model to investigate possible wing hinge angle combinations to achieve proper wing deployment with the MTR.

2.2 Theoretical Development - Introduction

A primary objective of the present work was to develop a mathematical model to calculate the response of the tail and wing positions of the MTR to changing

aerodynamic forces. In a later section of this thesis, the validation of this model is conducted against measurements that were made on a test article in the Glenn L. Martin wind tunnel.

Even a cursory examination of Fig. 1.1 shows that the kinematics of the folding wings are relatively complicated; in fact, the analysis of the problem necessarily involves several coordinate transformations to define the position vector of a point on the wing with respect to a datum or reference coordinate system. The prediction of the aerodynamic angles of attack along the wings and tail will then allow for an estimate of the aerodynamic forces and moments on the wings during their folding sequence.

Two-dimensional wing strip theory was used to predict the wing and tail aerodynamics. Because the wing folding sequence involves large excursions in angle of attack, the aerodynamics of the wing both below stall and in the post-stall condition were represented. Airfoil lift, drag and pitching moment characteristics for a full 360° angle of attack range were used, and these data were introduced into the modeling by means of a table look-up routine. The coefficient of lift, drag and pitching moment versus angle of attack used is shown in Fig. 2.2. Intermediate values in the table were obtained by linear interpolation. The net forces (lift and drag) and moments on the wings were then obtained by spanwise integration. The induced effects were accounted for in the model by means of an aspect ratio correction.

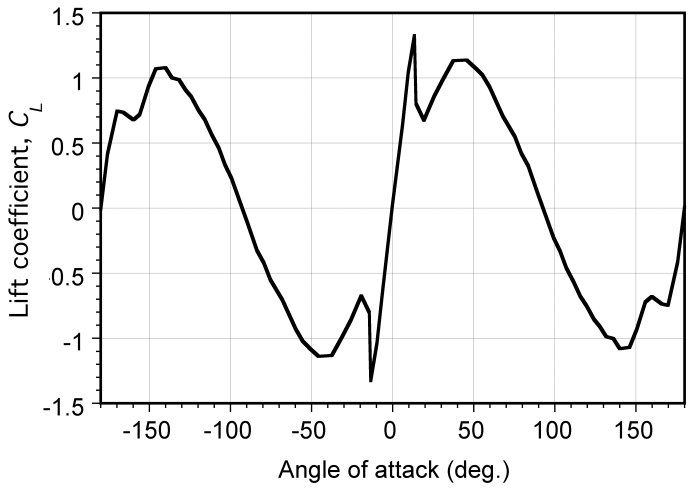

(a)

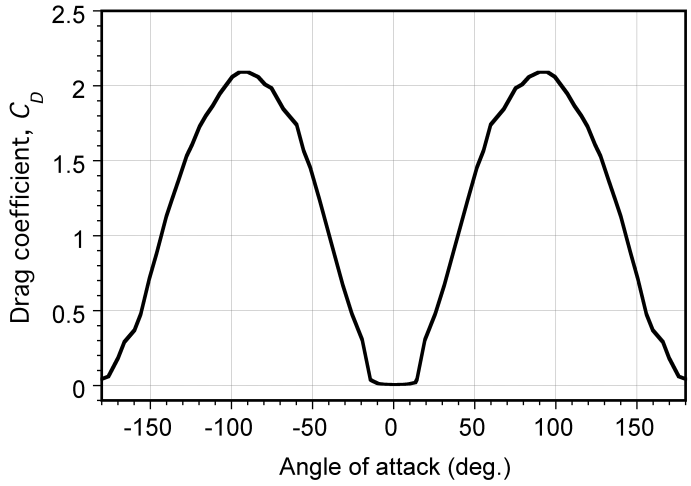

(b)

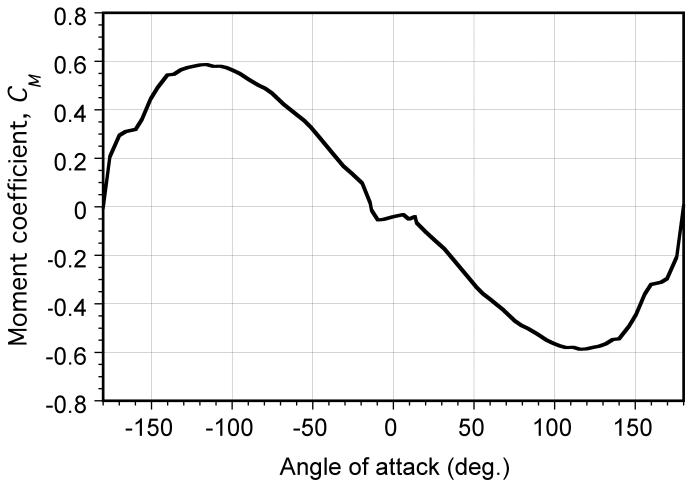

(c)

Figure 2.2: Coefficient of lift, drag and pitching moment versus angle of attack used in the mathematical model. (a) Lift coefficient; (b) Drag coefficient; (c) Moment coefficient.

2.2.1 Coordinate Systems

A fixed set of Cartesian coordinate systems was used to define the MTR's body, tail, wing hinge angle, and wing surface relative to each other. Using several coordinate transformations, a vector defined in one coordinate system can be transferred to another coordinate system [9]. The Cartesian coordinate system for the body, tail, and wing are shown schematically in Figs. 2.3, 2.4 and 2.5, respectively. In what follows, the equations needed to determine the dynamic behavior of the MTR as a system are described.

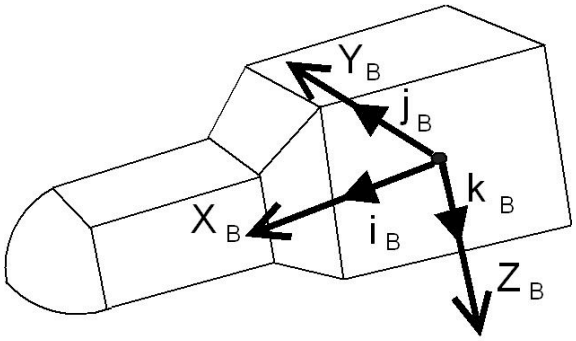

Figure 2.3: Placement and orientation of the MTR's body Cartesian coordinate system.

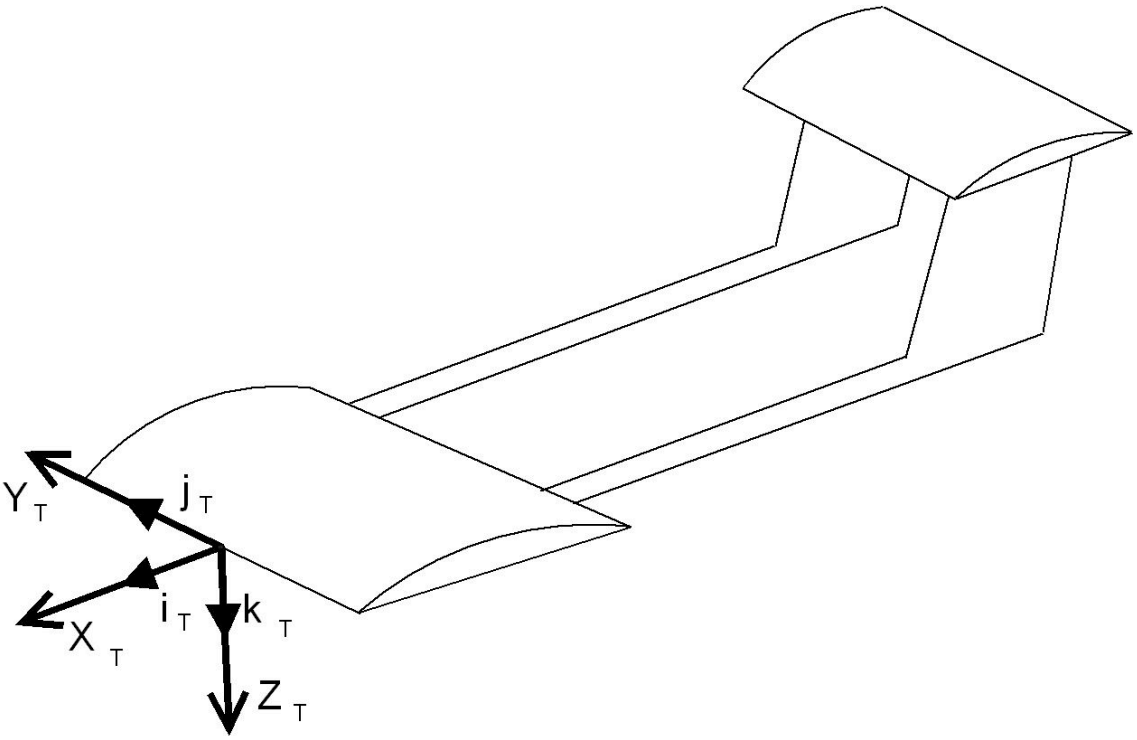

Figure 2.4: Placement and orientation of the MTR's tail Cartesian coordinate system.

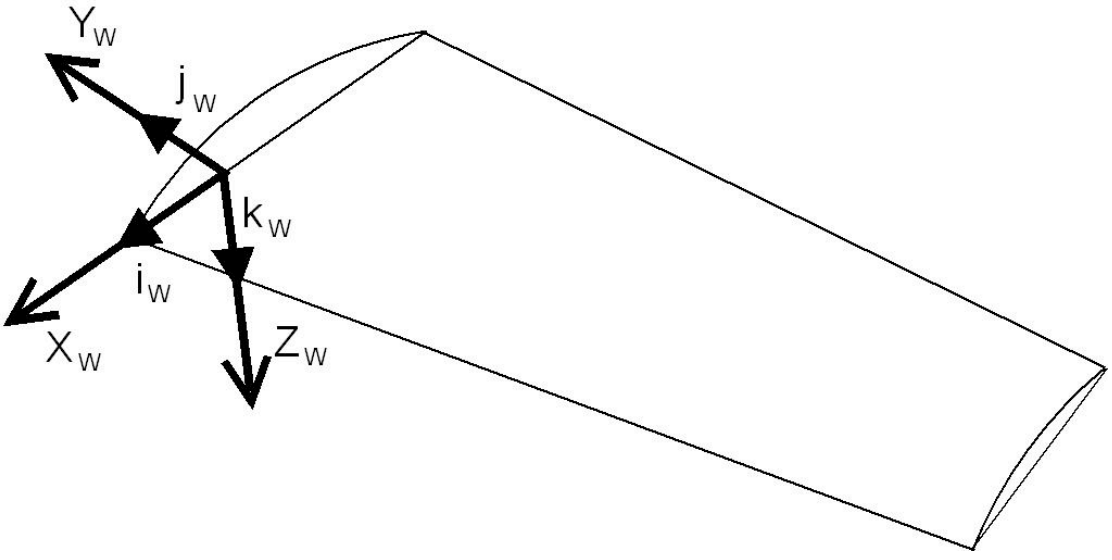

Figure 2.5: Placement and orientation of the MTR's wing Cartesian coordinate system.

2.2.2 Transformation Matrices

The coordinate transformation matrix from the tail to the wing hinge coordinates is given by

$$[S_{HT}] = [S_{H2}][S_{21}][S_{1T}] \tag{2.1}$$

where

$$[S_{1T}] = \begin{bmatrix} 1 & 0 & 0 \\ 0 & \cos\phi_{\mathrm{H}} & \sin\phi_{\mathrm{H}} \\ 0 & -\sin\phi_{\mathrm{H}} & \cos\phi_{\mathrm{H}} \end{bmatrix} \tag{2.2}$$

$$[S_{21}] = \begin{bmatrix} \cos\theta_{\mathrm{H}} & 0 & -\sin\theta_{\mathrm{H}} \\ 0 & 1 & 0 \\ \sin\theta_{\mathrm{H}} & 0 & \cos\theta_{\mathrm{H}} \end{bmatrix} \tag{2.3}$$

and

$$[S_{H2}] = \begin{bmatrix} \cos\psi_{\mathrm{H}} & \sin\psi_{\mathrm{H}} & 0 \\ -\sin\psi_{\mathrm{H}} & \cos\psi_{\mathrm{H}} & 0 \\ 0 & 0 & 1 \end{bmatrix} \tag{2.4}$$

The net coordinate transformation, shown in Fig. 2.6, is defined first as the required rotation about the x-axis by the angle ϕ, as given by Eq. 2.2, then about the y-axis by the angle θ, as given by Eq. 2.3, and then about the z-axis by the angle ψ, as given by Eq. 2.4. This transformation is necessary to rotate the orientation of the tail coordinate system into the wing hinge coordinate system. It is important to note that the angle ψ_{H} is the angle that defines the rotation (pivoting) of the wing about the wing hinge. The angles ϕ_{H} and θ_{H} are fixed angles that define the wing hinge in terms of its inclination.

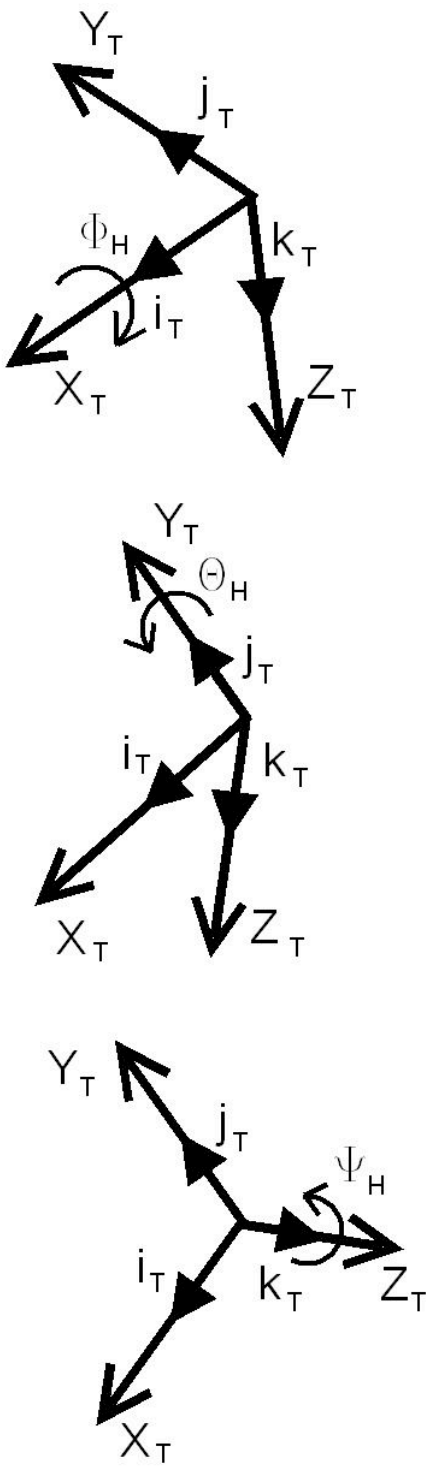

Figure 2.6: Coordinate transformation from tail to wing hinge.

The coordinate transformation matrices that are used from the wing to the wing hinge coordinate system as depicted in Fig. 2.7 are given by

$$[S_{HW}] = [S_{H2}][S_{21_W}][S_{1W}] \tag{2.5}$$

where

$$[S_{1W}] = \begin{bmatrix} 1 & 0 & 0 \\ 0 & \cos\phi_{\mathrm{W}} & \sin\phi_{\mathrm{W}} \\ 0 & -\sin\phi_{\mathrm{W}} & \cos\phi_{\mathrm{W}} \end{bmatrix} \tag{2.6}$$

$$[S_{21_W}] = \begin{bmatrix} \cos\theta_{\mathrm{W}} & 0 & -\sin\theta_{\mathrm{W}} \\ 0 & 1 & 0 \\ \sin\theta_{\mathrm{W}} & 0 & \cos\theta_{\mathrm{W}} \end{bmatrix} \tag{2.7}$$

and

$$[S_{H2}] = \begin{bmatrix} 1 & 0 & 0 \\ 0 & 1 & 0 \\ 0 & 0 & 1 \end{bmatrix} \tag{2.8}$$

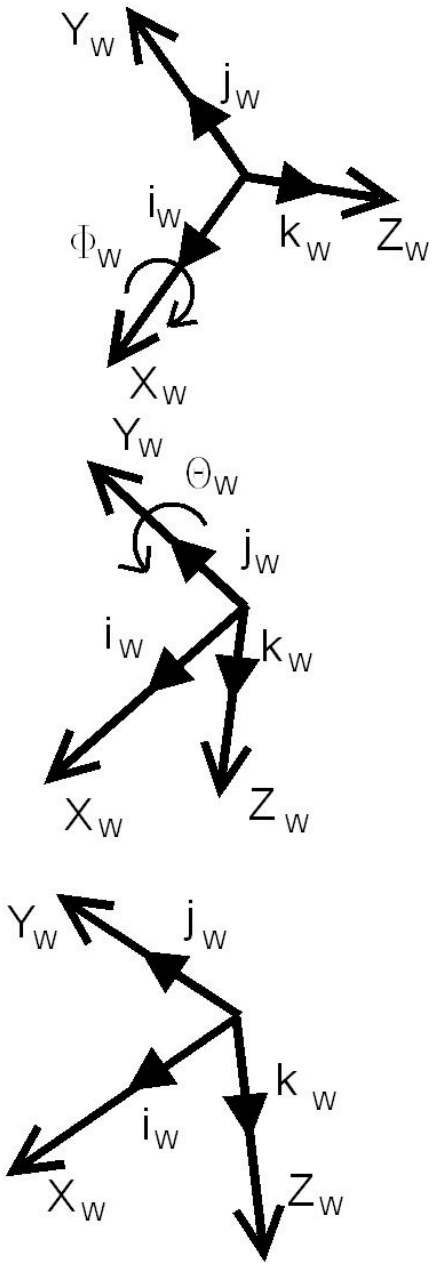

Figure 2.7: Coordinate transformation from wing to wing hinge.

The coordinate transformation matrix from the body to the tail, depicted in Fig. 2.8 coordinates is given by

$$[S_{TB}] = \begin{bmatrix} \cos\theta_{\mathrm{T}} & 0 & -\sin\theta_{\mathrm{T}} \\ 0 & 1 & 0 \\ \sin\theta_{\mathrm{T}} & 0 & \cos\theta_{\mathrm{T}} \end{bmatrix} \tag{2.9}$$

where the angle θ_{T} defines the tail rotation about the tail hinge.

The coordinate transformation matrix from the wing hinge to the wing coordinate system is given by

$$[S_{WH}] = [S_{HW}]^T \tag{2.10}$$

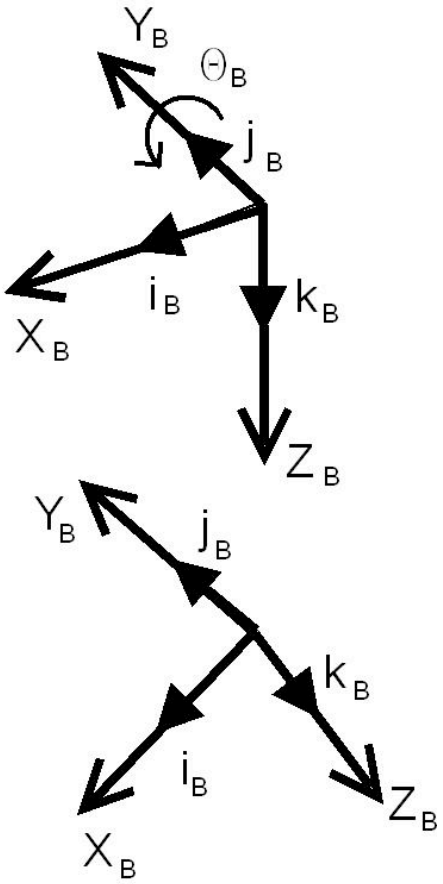

Figure 2.8: Coordinate transformation from body to tail.

This transformation is developed by taking the transpose of the coordinate transformation matrix from the wing to the wing hinge coordinates.

The coordinate transformation matrix from the tail to the wing coordinate system is given by

$$[S_{WT}] = [S_{WH}][S_{HT}] \tag{2.11}$$

This is done by multiplying the transformation matrix used for the wing hinge to the wing coordinates by the transformation matrix from the tail to the wing hinge coordinates.

The transformation matrix from the body to the wing coordinates is given by

$$[S_{WB}] = [S_{WT}][S_{TB}] \tag{2.12}$$

The transformation matrix from the wing to the tail coordinates is given by

$$[S_{TW}] = [S_{WT}]^T \tag{2.13}$$

Finally, the transformation matrix from the wing to the body coordinates is given by

$$[S_{BW}] = [S_{WB}]^T \tag{2.14}$$

2.2.3 Relative Velocity Vector

The velocity of the body defined in wing coordinates, is given by the equation

$$\mathbf{V}_W = [S_{WB}]\mathbf{V}_B \tag{2.15}$$

This equation is used to calculate the local flow velocity from the body velocity at points along the wingspan.

The vector $\mathbf{R}_{PW}$, which is defined in Eq. 2.17, is the distance from the center of gravity of the body to a point located on the wing; it is transfered to the wing coordinate system using the required matrix transformation. The vector $\mathbf{R}_1$ is the distance from the center of gravity of the body to the horizontal tail hinge attachment point, and is defined in body coordinates. The vector $\mathbf{R}_{2_W}$ is the distance from the tail hinge attachment point to the wing hinge, and is defined in tail coordinates. The vector $\mathbf{R}_{3_W}$ is measured from the wing hinge to a given point on the wing, and is defined in wing coordinates.

For the following calculations made in the mathematical model, the reference point on the wing is located at the 1/4-chord location along the span of the wing. The vector $\mathbf{R}_{PW}$ is given by

$$\mathbf{R}_{PW} = R_1 i_B + R_1 j_B + R_1 k_B + R_2 i_T + R_2 j_T + R_2 k_T + R_3 i_W + R_3 j_W + R_3 k_W \quad (2.16)$$

In terms of the wing coordinate system $\mathbf{R}_{PW}$ is given by

$$\mathbf{R}_{PW} = [S_{WB}] \begin{Bmatrix} R_{1_X} \\ R_{1_Y} \\ R_{1_Z} \end{Bmatrix} + [S_{WT}] \begin{Bmatrix} R_{2_{W_X}} \\ R_{2_{W_Y}} \\ R_{2_{W_Z}} \end{Bmatrix} + \begin{Bmatrix} R_{3_{W_X}} \\ R_{3_{W_Y}} \\ R_{3_{W_Z}} \end{Bmatrix} \quad (2.17)$$

and the components of vector $\mathbf{R}_{PW}$ are shown in the schematic in Fig. 2.9.

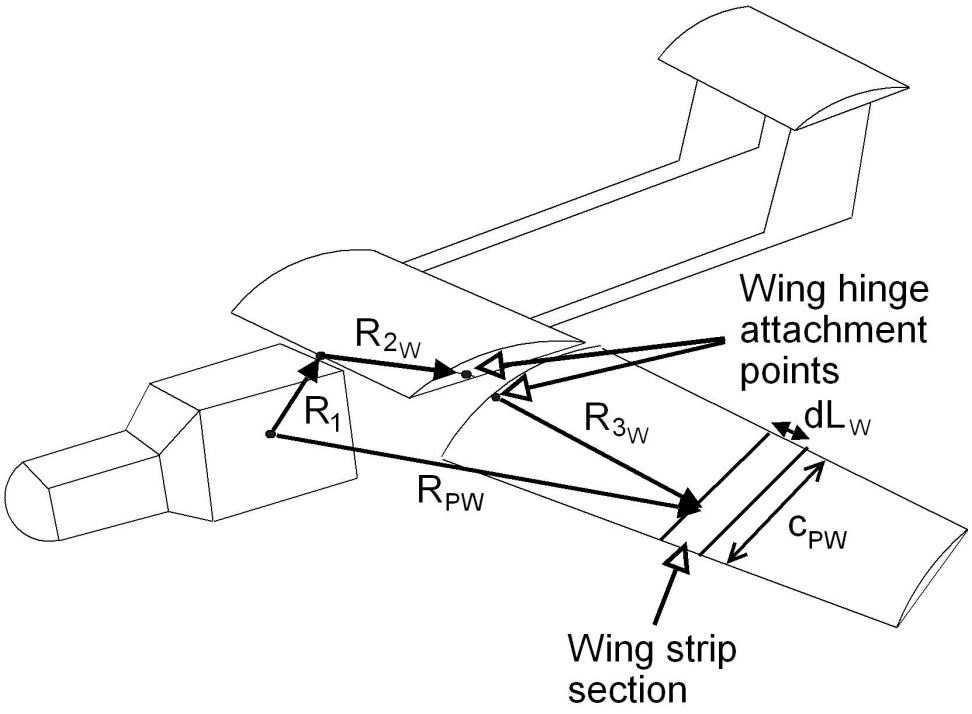

Figure 2.9: Components of vector $\mathbf{R}_{PW}$.

The angular velocity $\mathbf{\Omega}_W$, which is defined as

$$\mathbf{\Omega}_W = p i_B + q j_B + r k_B + \dot{\theta}_{\mathrm{T}} j_T + \dot{\psi}_{\mathrm{H}} k_H \tag{2.18}$$

In terms of the wing coordinate system $\mathbf{\Omega}_W$ is given by

$$\mathbf{\Omega}_W = [S_{WB}] \begin{Bmatrix} p \\ q \\ r \end{Bmatrix} + [S_{WT}] \begin{Bmatrix} 0 \\ \dot{\theta}_{\mathrm{T}} \\ 0 \end{Bmatrix} + [S_{WH}] \begin{Bmatrix} 0 \\ 0 \\ \dot{\psi}_{\mathrm{H}} \end{Bmatrix} \tag{2.19}$$

this is the angular velocity of the vector $\mathbf{R}_{PW}$ resulting from the roll, pitch, and yaw rates of the aircraft, respectively; they are defined by p, q and r about the body axes, for the work done in this thesis they are set to zero. Also taken into account is the angular velocity about the tail hinge $\dot{\theta}_T$, and the angular velocity about the wing hinge $\dot{\psi}_H$. This angular velocity has been transformed to be in terms of the wing coordinate system.

The change in $\mathbf{\Omega}_W$ as a function of time is given by

$$\dot{\mathbf{\Omega}}_W = [S_{WT}] \begin{Bmatrix} 0 \\ \ddot{\theta}_{\mathrm{T}} \\ 0 \end{Bmatrix} + [S_{WH}] \begin{Bmatrix} 0 \\ 0 \\ \ddot{\psi}_{\mathrm{H}} \end{Bmatrix} + [\dot{S}_{WT}] \begin{Bmatrix} 0 \\ \dot{\theta}_{\mathrm{T}} \\ 0 \end{Bmatrix} + [\dot{S}_{WH}] \begin{Bmatrix} 0 \\ 0 \\ \dot{\psi}_{\mathrm{H}} \end{Bmatrix} \tag{2.20}$$

Note that the pitch, yaw and roll rates have been omitted due to being zero for these equations.

The velocity $\mathbf{V}_{PW}$, which is defined in Eq. 2.21 [10], is the velocity at a given point on the wing resulting from the time rate of change of the vector $\mathbf{R}_{PW}$ and

also from the angular velocity $\mathbf{\Omega}_W$, i.e.,

$$\mathbf{V}_{PW} = \frac{d\mathbf{R}_{PW}}{dt} + \mathbf{\Omega}_W \times \mathbf{R}_{PW} \tag{2.21}$$

The total velocity at a given point on the wing, which is the sum of the components $\mathbf{V}_{PW}$ and $\mathbf{V}_W$, is given by

$$\mathbf{V}_{TOT_{PW}} = \mathbf{V}_{PW} + \mathbf{V}_W \tag{2.22}$$

The magnitude of the total velocity, which is required to calculate the aerodynamic forces over a given section of the wing, is given by

$$V_{\infty_{PW}} = \sqrt{V^2_{TOT_{PW_X}} + V^2_{TOT_{PW_Z}}} \tag{2.23}$$

The corresponding dynamic pressure at a given section on the wing is given by

$$q_{\infty_{PW}} = \frac{1}{2}\rho V^2_{\infty_{PW}} \tag{2.24}$$

2.2.4 Sweep Angle Correction

The independence principle was used to calculate the airloads in the attached flow regime, but a correction was used in stalled flow. The local wing sweep angle relative to the flow is given by

$$\Lambda = \arctan\left(\frac{V_{W_Y}}{V_{W_X}}\right) \tag{2.25}$$

The value of this parameter is used to calculate a post-stall lift coefficient correction that takes account of the elevated lift coefficients on the wing with sweep. The angle

of attack at a point on the wing that takes into effect the amount of wing twist per length of the wing, as defined by δ, is given by

$$\alpha_{_{PW}} = \arctan\left(\frac{V_{TOT_{PW_Z}}}{V_{TOT_{PW_X}}}\right) - \delta\left(\frac{Y_W}{L_e}\right) \tag{2.26}$$

The corrected lift coefficient beyond the static stall angle of attack [9] is given by

$$C_{L_{corr}} = C_L\left(\frac{1}{\cos\Lambda}\right) \tag{2.27}$$

2.2.5 Unsteady Aerodynamics

Unsteady aerodynamic effects from the changing angle of attack as a function of time was modeled using a correction from classical unsteady aerodynamic theory [11]. An effective angle of attack α_{eff}, was used to find the instantaneous lift, drag and moments, where

$$\alpha_{\text{eff}} = \alpha_t - X_t - Y_t \tag{2.28}$$

and where the deficiency functions X and Y are given by

$$X_t = X_{(t-\delta t)}e^{-b_1\Delta S} + A_1\ \Delta\alpha\ e^{-b_1(\frac{\Delta S}{2})} \tag{2.29}$$

$$Y_t = Y_{(t-\delta t)}e^{-b_2\Delta S} + A_2\ \Delta\alpha\ e^{-b_2(\frac{\Delta S}{2})} \tag{2.30}$$

with

$$\Delta S = \frac{2V\Delta t}{c} \tag{2.31}$$

and

$$\Delta\alpha = \alpha_t - \alpha_{(t-\delta t)} \tag{2.32}$$

and where the coefficients A_1=0.165, A_2=0.335, b_1=0.0455, and b_2=0.3 come from the exponential approximation to Wagner's function.

2.2.6 Wing Forces and Moments

The sectional lift, drag and pitching moment about the 1/4-chord at each elemental section of the wing were then computed. The sectional lift is given by

$$dL_{PW} = q_{\infty_{PW}} C_{L_{PW}} \sqrt{1 - \left(\frac{Y_W}{L_e}\right)^2} c_{PW}\ dL_w \tag{2.33}$$

where the term dL_W represents the spanwise width of the elemental section, and c_{PW} is the local wing chord at that particular section of the wing (in general, the wing is both twisted and tapered). For the drag, the corresponding equation is

$$dD_{PW} = q_{\infty_{PW}} C_{D_{PW}} c_{PW} dL_w \tag{2.34}$$

and for the pitching moment the equation is

$$dM_{PW} = q_{\infty_{PW}} C_{M_{PW}} c_{PW}^2 dL_w \tag{2.35}$$

The components of the sectional lift and drag were transfered into wing coordinates corresponding to the normal (z) and tangential (x) components, which are given by

$$dN_{W_Z} = -dL_{PW} \cos\alpha_{PW} - dD_{PW} \sin\alpha_{PW} \tag{2.36}$$

and

$$dT_{W_X} = dL_{PW} \sin\alpha_{PW} - dD_{PW} \cos\alpha_{PW} \tag{2.37}$$

The summation of the normal and tangential sectional components of the wing lift and drag in wing coordinates along the span of the wing is given by

$$N_{W_Z} = \sum_{i=1}^{i=K_W} dN_{W_Z} \tag{2.38}$$

and

$$T_{W_X} = \sum_{i=1}^{i=K_W} dT_{W_X} \tag{2.39}$$

In each case, the index i is the wing section number, where K_W is the total number of sections.

A vector from the wing hinge to the aerodynamic center of an elemental section located on the left wing is shown in Fig. 2.10 and is given by the equation

$$\mathbf{R}_{W_{AC}} = \left\{ \begin{array}{c} R_{3_{W_X}} \\ R_{3_{W_Y}} \\ R_{3_{W_Z}} \end{array} \right\} \tag{2.40}$$

The sectional pitching moment produced at the wing hinge, as defined in wing coordinates, resulting from the lift and drag acting at the aerodynamic center of a given elemental wing section, is given by

$$d\mathbf{M}_{LD} = \mathbf{R}_{W_{AC}} \times \left\{ \begin{array}{c} dT_{W_X} \\ 0 \\ dN_{W_Z} \end{array} \right\} \tag{2.41}$$

The total sectional moment produced from the lift, drag, and the moment

produced about the aerodynamic center point at a given wing section is given by

$$d\mathbf{M}_{TOT} = \left\{ \begin{array}{c} 0 \\ d_{M_{PW}} \\ 0 \end{array} \right\} + d\mathbf{M}_{LD} \tag{2.42}$$

The total weight of the wing, which is defined in wing coordinates, is given by

$$\mathbf{W}_{CG_W} = [S_{WB}] \left\{ \begin{array}{c} 0 \\ 0 \\ W \end{array} \right\} \tag{2.43}$$

The moment produced (as defined in wing coordinates from the weight of the wing) is given by

$$\mathbf{M}_{CG_W} = \mathbf{R}_{CG} \times \mathbf{W}_{CG_W} \tag{2.44}$$

Notice that $\mathbf{R}_{CG}$ is a vector from the wing hinge to the center of gravity point on the wing, and is defined in wing coordinates.

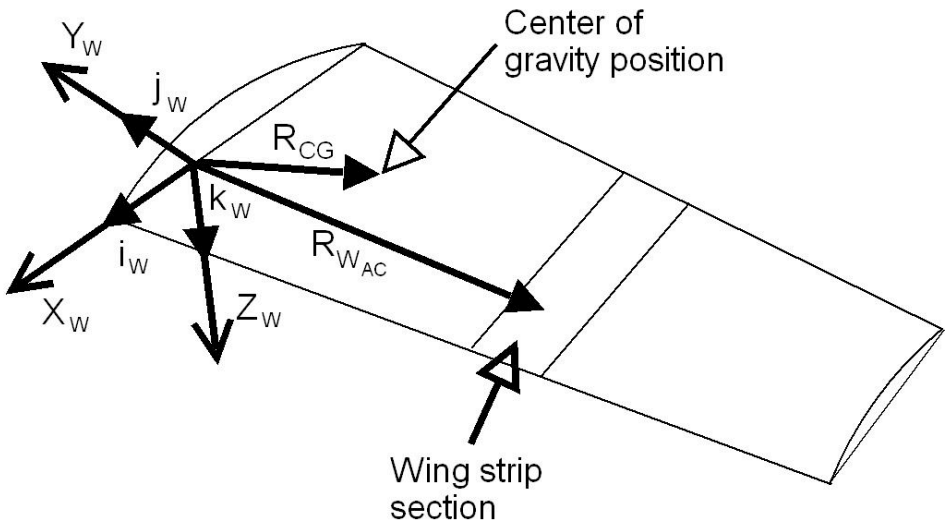

Figure 2.10: Vector $\mathbf{R}_{CG}$ from wing hinge to the center of gravity point on the wing and vector $\mathbf{R}_{W_{AC}}$ from the wing hinge to the aerodynamic center point on a wing strip section.

The total moment (in wing coordinates) from the summation of the sectional moments produced from the lift, drag and moment about the aerodynamic center acting down the span of the wing is given by

$$\mathbf{M}_{TOT_W} = \sum_{i=1}^{K_W} \mathbf{dM}_{TOT} + \mathbf{M}_{CG_W} \tag{2.45}$$

Notice that the total moment also includes the moment resulting from the wing weight, $\mathbf{M}_{CG_W}$.

The total moment acting on the wing hinge in wing hinge coordinates, transfered from the total moment that is acting on the wing in wing coordinates, is given by

$$\mathbf{M}_{TOT_H} = [S_{HW}]\mathbf{M}_{TOT_W} \tag{2.46}$$

The total forces acting on the MTR's body from the lift and drag produced from the two (left- and right-hand) wings is given by

$$\mathbf{N}_{T_B} = 2[S_{BW}] \left\{ \begin{array}{c} T_{W_X} \\ 0 \\ N_{W_Z} \end{array} \right\} \tag{2.47}$$

Notice that these forces are expressed in body coordinates.

2.2.7 Tail Forces and Moments

The vector, $\mathbf{R}_{PT}$, is defined from the body center of gravity to a point on the tail and is given by

$$\mathbf{R}_{PT} = R_1 i_B + R_1 j_B + R_1 k_B + R_{T2} i_T + R_{T2} j_T + R_{T2} k_T \tag{2.48}$$

Expressed in terms of the tail coordinate system $\mathbf{R}_{PT}$ is given by

$$\mathbf{R}_{PT} = [S_{TB}] \begin{Bmatrix} R_{1_X} \\ R_{1_Y} \\ R_{1_Z} \end{Bmatrix} + \begin{Bmatrix} R_{T2_X} \\ R_{T2_Y} \\ R_{T2_Z} \end{Bmatrix} \tag{2.49}$$

The vector $\mathbf{R}_1$ is from the body center of gravity to the tail hinge point and is defined in body coordinates. Vector $\mathbf{R}_{T_2}$ is a vector from the tail hinge to a point located on the tail, and is defined in tail coordinates. The scalar components of vector $\mathbf{R}_{PT}$ are shown in Fig. 2.11.

The angular velocity $\mathbf{\Omega}_T$, as defined by

$$\mathbf{\Omega}_T = pi_B + qj_B + rk_B + \dot{\theta}_{\mathrm{T}} j_T \tag{2.50}$$

Expressed in term of the tail coordinate system $\mathbf{\Omega}_T$ is given by

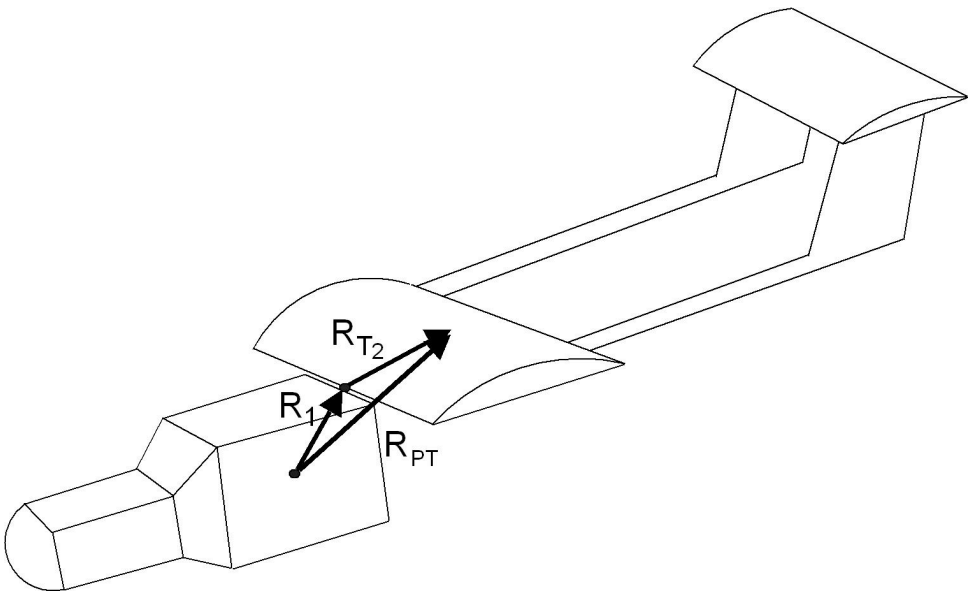

Figure 2.11: Vector components of vector $\mathbf{R}_{PT}$.

$$\mathbf{\Omega}_T = [S_{TB}] \left\{ \begin{array}{c} p \\ q \\ r \end{array} \right\} + \left\{ \begin{array}{c} 0 \\ \dot{\theta}_{\mathrm{T}} \\ 0 \end{array} \right\} \tag{2.51}$$

this is the angular velocity of the vector $\mathbf{R}_{PT}$ resulting from the roll, pitch, and yaw rates, respectively, as defined by p, q and r of the body, and also including the angular velocity about the tail hinge $\dot{\theta}_{\mathrm{T}}$. This angular velocity is transformed so as to be in terms of the tail coordinate system.

The time rate of change of $\mathbf{\Omega}_T$ is given by

$$\dot{\mathbf{\Omega}}_T = \left\{ \begin{array}{c} 0 \\ \ddot{\theta}_{\mathrm{T}} \\ 0 \end{array} \right\} \tag{2.52}$$

the effects in the term $\dot{\mathbf{\Omega}}_T$ due to the pitch, yaw and roll rates have been omitted because they equal zero for the work done in this thesis.

The velocity of a point on the horizontal tail resulting from $\mathbf{\Omega}_T$ and the time rate of change of the vector $\mathbf{R}_{PT}$ is given by

$$\mathbf{V}_{PT} = \frac{d\mathbf{R}_{PT}}{dt} + \mathbf{\Omega}_T \times \mathbf{R}_{PT} \tag{2.53}$$

The velocity of a point on the horizontal tail in tail coordinates resulting from the velocity of the body $\mathbf{V}_B$ is given by

$$\mathbf{V}_T = [S_{TB}]\mathbf{V}_B \tag{2.54}$$

The total velocity for a given point on the tail is given by

$$\mathbf{V}_{TOT_{PT}} = \mathbf{V}_T + \mathbf{V}_{PT} \tag{2.55}$$

The resultant relative flow velocity required to calculate the lift, drag and pitching moment of a given section on the horizontal tail is given by

$$V_{\infty_T} = \sqrt{V_{TOT_{PT_X}}^2 + V_{TOT_{PT_Z}}^2} \tag{2.56}$$

The angle of attack on a section of the horizontal tail is given as

$$\alpha_{PT} = \arctan\left(\frac{V_{TOT_{PT_Z}}}{V_{TOT_{PT_X}}}\right) - \beta \tag{2.57}$$

Notice that β is the angle of incidence (pitch angle) of the tail section. This value is needed to model the aerodynamics of tail Section 2 (see next), which has a variable (adjustable) pitch setting.

The dynamic pressure at a particular section of the tail is given by

$$q_{\infty_T} = \frac{1}{2}\rho V_{\infty_T}^2 \tag{2.58}$$

The total lift, drag, and pitching moment at a given section on the horizontal tail are given by the equations

$$L_T = q_{\infty_T} C_{L_T} S_T \tag{2.59}$$

$$D_T = q_{\infty_T} C_{D_T} S_T \tag{2.60}$$

and

$$M_T = q_{\infty_T} C_{M_T} S_T c_T \tag{2.61}$$

respectively. Notice that the velocity $\mathbf{V}_{PT}$ is calculated at 1/4-chord of the given tail section. Furthermore, notice that there are two tail sections: Section 1 refers to the mid-section part of the tail, and Section 2 refers to the stabilator section, which has a variable incidence. The term S_T is the surface area of the particular section.

The normal and tangential force components on the tail resulting from lift and drag in the tail coordinate system are given by

$$N_{Z_T} = (-L_T \cos \alpha_{_{PT}} - D_T \sin \alpha_{_{PT}}) \cos \beta \tag{2.62}$$

and

$$T_{X_T} = (L_T \sin \alpha_{_{PT}} - D_T \cos \alpha_{_{PT}}) \cos \beta \tag{2.63}$$

The lift and drag components on tail Section 1 in tail coordinates is given by

$$\mathbf{N}_{T_{T_1}} = \left\{ \begin{array}{c} T_{X_{T_1}} \\ 0 \\ N_{Z_{T_1}} \end{array} \right\} \tag{2.64}$$

The lift and drag components on tail Section 2 in tail coordinates is given by

$$\mathbf{N}_{T_{T_2}} = \left\{ \begin{array}{c} T_{X_{T_2}} \\ 0 \\ N_{Z_{T_2}} \end{array} \right\} \tag{2.65}$$

The weight of tail Section 1 (mid-section wing), expressed in tail coordinates, is given by

$$\mathbf{W}_{CG_{T_1}} = [S_{TB}] \left\{ \begin{array}{c} 0 \\ 0 \\ W_{T_1} \end{array} \right\} \tag{2.66}$$

The weight of tail Section 2 (tail components), expressed in tail coordinates, is given by

$$\mathbf{W}_{CG_{T_2}} = [S_{TB}] \left\{ \begin{array}{c} 0 \\ 0 \\ W_{T_2} \end{array} \right\} \tag{2.67}$$

The weight of tail Section 3 (tail boom and structure components), again expressed in tail coordinates, is given by

$$\mathbf{W}_{CG_{T_3}} = [S_{TB}] \left\{ \begin{array}{c} 0 \\ 0 \\ W_{T_3} \end{array} \right\} \tag{2.68}$$

The moment produced on the tail hinge (in tail coordinates) from the lift and drag produced from tail Sections 1 and 2 is given by

$$\mathbf{M}_{LD_{TH}} = \mathbf{R}_{1_T} \times \mathbf{N}_{T_{T_1}} + \mathbf{R}_{2_T} \times \mathbf{N}_{T_{T_2}} \tag{2.69}$$

The vector $\mathbf{R}_{1_T}$ is a vector from the tail hinge to the aerodynamic center of Section 1. The vector $\mathbf{R}_{2_T}$ is a vector from the tail hinge to the aerodynamic center of Section 2.

The moment (in tail coordinates) about the tail hinge from the weight of the tail components is given by

$$\mathbf{M}_{CG_{TH}} = \mathbf{R}_{CG_{T_1}} \times \mathbf{W}_{CG_{T_1}} + \mathbf{R}_{CG_{T_2}} \times \mathbf{W}_{CG_{T_2}} + \mathbf{R}_{CG_{T_3}} \times \mathbf{W}_{CG_{T_3}} \tag{2.70}$$

The vectors $\mathbf{R}_{CG_{T_1}}$, $\mathbf{R}_{CG_{T_2}}$, and $\mathbf{R}_{CG_{T_3}}$ are the vectors from the tail hinge to the center of gravity locations of tail Sections 1, 2 and 3, respectively.

The moment in tail coordinates about the tail hinge from the moments produced about the aerodynamic centers of tail Sections 1 and 2 is given by

$$\mathbf{M}_{AC_{TH}} = \left\{ \begin{array}{c} 0 \\ M_{T_1} \\ 0 \end{array} \right\} + \left\{ \begin{array}{c} 0 \\ M_{T_2} \\ 0 \end{array} \right\} \tag{2.71}$$

The moment produced on the tail hinge (in tail coordinates) from the wing moment that acts on the wing hinge and then onto the tail is given by

$$\mathbf{M}_{TH_M} = 2[S_{TW}]\mathbf{M}_{TOT_W} \tag{2.72}$$

Notice that this moment is multiplied by two to account for both the left- and right-hand wing panels.

The force acting on the tail at the wing hinge angle location because of the lift and drag acting on the wing is given by

$$\mathbf{F}_{W_{LD}} = [S_{TB}]\mathbf{N}_{T_B} \tag{2.73}$$

This force is then transfered into tail coordinates.

The force acting on the tail at the wing hinge angle location resulting from the weight of a wing is

$$\mathbf{F}_{CG_W} = [S_{TW}]\mathbf{W}_{CG_W} \tag{2.74}$$

Again, this force is transfered into the tail coordinates.

The sum of the moments acting on the tail hinge in tail coordinates from the lift and drag forces on the wings, and also from the wing weight, is given by

$$\mathbf{M}_{TH_W} = \mathbf{R}_{TH} \times 2\mathbf{F}_{W_{LD}} + \mathbf{R}_{TH} \times 2\mathbf{F}_{CG_W} \tag{2.75}$$

Notice that these moments are again multiplied by two to account for the contributions from both wings.

The total moment acting on the tail hinge from summation of the moments as described previously is given by

$$\mathbf{M}_{TOT_{TH}} = \mathbf{M}_{LD_{TH}} + \mathbf{M}_{CG_{TH}} + \mathbf{M}_{AC_{TH}} + \mathbf{M}_{TH_M} + \mathbf{M}_{TH_W} \tag{2.76}$$

2.2.8 Inertia Calculations

The acceleration of a point on the wing in wing coordinates is given by

$$\begin{aligned} \mathbf{A}_{PW} &= \dot{\mathbf{\Omega}}_W \times \mathbf{R}_{PW} + \mathbf{\Omega}_W \times (\mathbf{\Omega}_W \times \mathbf{R}_{PW}) \\ &\quad +2\mathbf{\Omega}_W \times \frac{d\mathbf{R}_{PW}}{dt} + \frac{d^2\mathbf{R}_{PW}}{dt^2} \end{aligned} \tag{2.77}$$

where $\mathbf{\Omega}_W$ is defined in Eq. 2.19, $\dot{\mathbf{\Omega}}_W$ is defined in Eq. 2.20 and $\mathbf{R}_{PW}$ is defined in Eq. 2.17 and is shown in Fig. 2.9.

The acceleration for a point on the tail in tail coordinates is given by

$$\begin{aligned} \mathbf{A}_{PT} &= \dot{\mathbf{\Omega}}_\mathbf{T} \times \mathbf{R}_{PT} + \mathbf{\Omega}_T \times (\mathbf{\Omega}_T \times \mathbf{R}_{PT}) \\ &\quad +2\mathbf{\Omega}_T \times \frac{d\mathbf{R}_{PT}}{dt} + \frac{d^2\mathbf{R}_{PT}}{dt^2} \end{aligned} \tag{2.78}$$

where $\mathbf{\Omega}_T$ is defined in Eq. 2.51, $\dot{\mathbf{\Omega}}_W$ is defined in Eq. 2.52 and $\mathbf{R}_{PT}$ is defined in Eq. 2.49 and is shown in Fig. 2.11.

The calculation of the inertia terms for the wing about the wing hinge angle location, as expressed in wing coordinates, is given by

$$\mathbf{I}_W = \int_0^{L_w} M_{A_W}(L)\,(\mathbf{A}_{PW} \times \mathbf{R}_{W_{AC}})\,dL_w \tag{2.79}$$

in discretized form using the trapezoidal method of integration over each wing section the inertia of the wing about the wing hinge is given by

$$\mathbf{I}_W = \sum_{i=1}^{i=K_W} k\ \Delta M_{A_W}\ \Delta Lw\,(\mathbf{A}_{PW} \times \mathbf{R}_{W_{AC}}) \tag{2.80}$$

Notice that the term ΔM_{A_W} is the section mass of the wing section, and ΔL_w is the elemental width of the wing section. Vector $\mathbf{R}_{W_{AC}}$ is a vector from the wing

hinge to the aerodynamic center of a wing section. This formula is based on the use of the trapezoidal method of integration, therefore, $k = 0.5$ if $i = 1$ or $i = K_W$, where K_W is the total number of elemental wing sections.

The inertia of the tail about the tail hinge expressed in tail coordinates is given by

$$\mathbf{I}_T = \int_0^{L_w} M_{A_T}(L) \left(\mathbf{A}_{PT} \times \mathbf{R}_T\right) dL_{e_T} \tag{2.81}$$

in discretized form using the trapezoidal method of integration over each tail section the inertia of the tail about the tail hinge is given by

$$\mathbf{I}_T = \sum_{i=1}^{i=K_T} k \; \Delta M_{A_T} \; \Delta L_{e_T} \left(\mathbf{A}_{PT} \times \mathbf{R}_T\right) \tag{2.82}$$

The term ΔM_{A_T} is the section mass of the tail section, and ΔL_{e_T} is the elemental length of the tail section. Vector $\mathbf{R}_T$ is a vector from the tail hinge to the mass location of a tail section. The term K_T is the total number of elemental tail sections. Again, $k = 0.5$ if $i = 1$ or $i = K_T$.

2.2.9 Differential Equations of Motion

The final differential equations that describe the angular displacements and acceleration, respectively, about the wing hinge and tail hinge from the inertia of these bodies and also the moments produced about the hinge locations [10], are given by

$$\left\{ \begin{array}{c} 0 \\ 0 \\ M_{TOT_{H_Z}} \end{array} \right\} = [S_{HW}] \sum_{i=1}^{i=K_W} k \; dMA_W \; dLw$$
$$\Big(\dot{\mathbf{\Omega}}_W \times \mathbf{R}_{PW} + \mathbf{\Omega}_W \times (\mathbf{\Omega}_W \times \mathbf{R}_{PW})$$
$$+2\mathbf{\Omega}_W \times \frac{d\mathbf{R}_{PW}}{dt} + \frac{d\mathbf{R}^2_{PW}}{dt^2} \Big) \times \mathbf{R}_{W_{AC}} \tag{2.83}$$

and

$$\left\{ \begin{array}{c} 0 \\ M_{TOT_{TH_Y}} \\ 0 \end{array} \right\} = \sum_{i=1}^{i=K_T} k \; dMA_T \; dLe_T \Big(\dot{\mathbf{\Omega}}_T \times \mathbf{R}_{PT}$$
$$+\mathbf{\Omega}_T \times (\mathbf{\Omega}_T \times \mathbf{R}_{PT}) + 2\mathbf{\Omega}_T \times \frac{d\mathbf{R}_{PT}}{dt} + \frac{d\mathbf{R}^2_{PT}}{dt^2} \Big) \times \mathbf{R}_T \tag{2.84}$$

These equations describe the change in angular momentum from the moments acting on the wing and tail hinges. The equations were solved using ode 45, which is a non-stiff, ordinary differential equation solver. Inside these equations are the terms for $\ddot{\theta}_T$ and $\ddot{\psi}_H$, using these terms the equations can be converted into a first order form. The output gave the angular velocity and position about both the tail hinge and wing hinge as defined by the matrix Y given below

$$Y = [\theta_T, \dot{\theta}_T, \psi_H, \dot{\psi}_H] \tag{2.85}$$

where θ_T is the angular position about the tail hinge, $\dot{\theta}_T$ is the angular velocity about the tail hinge, ψ_H is the angular position about the wing hinge and $\dot{\psi}_H$ is the

angular velocity about the wing hinge.

The initial conditions required to solve the differential equations are the rotation angle of the wing, ψ_{H} and the tail angle θ_{T}, when no aerodynamic forces are applied, which can be solved for by first setting the relative velocity of the body to zero to make the aerodynamic forces zero. The only forces acting on the wing and tail will then be from gravity, and the wings and tail will pivot freely to reach their equilibrium positions. The resulting wing and tail positions were then used as initial conditions. The initial angular velocity about the tail and wing hinges were set to zero.

Using this mathematical model the time dependent dynamic behavior of wings and tail from aerodynamic forcing could be solved. Additionally the lift, drag and moments on static configurations of the MTR could be easily calculated as well.

Chapter 3

Equilibrium Analysis

The previous chapter discussed the development of a mathematical model to predict the dynamic behavior of the wings and tail during deployment, as well as calculating the lift, drag and moment forces on static configurations of the MTR. The current chapter describes how a simplified version of the mathematical model can be used to conduct an equilibrium analysis to predict optimal wing hinge geometry for aerodynamic wing deployment. The goal of this chapter was to determine two optimal wing hinge angle settings that would most likely allow for full aerodynamic wing deployment.

3.1 Computer Aided Design Model

Using Computer Aided Design (CAD) modeling, an initial range of wing hinge angle settings were determined that would allow for the geometric constraints of the wings having to fold down and hang vertically during hover, and also to be in the correct position when deployed during flight.

The mid-section wing and the left wing was modeled and attached to each other using a pin and collar type wing hinge. Figure 3.3 shows example of the model being used to look at the geometric positions of the wing and mid-section wing during deployment. The position of the wing hinge about which rotation takes

place can be defined by two angles, the rotation of the hinge around its x-axis through an angle, ϕ_{H}, and the rotation of the hinge around its y-axis, θ_{H}, these angles are depicted in Figs. 3.1 and 3.2, respectively. Both of these angles define the wing hinge orientation, and are measured with respect to the coordinate system of the tail. Using the CAD model, the range of wing hinge angles to allow for geometric and kinematic feasibility was determined to be $25° \leq \phi_{\mathrm{H}} \leq 50°$ and $25° \leq \theta_{\mathrm{H}} \leq 50°$.

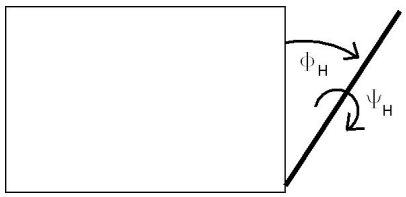

Figure 3.1: Front view of the outward orientation of the wing hinge axis by angle ϕ_{H}.

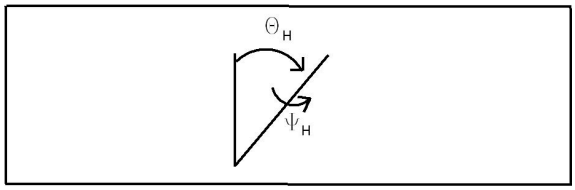

Figure 3.2: Side view of the rearward orientation of the wing hinge axis by angle θ_{H}.

3.2 Mathematical Model for Equilibrium Analysis

During the time period this work was being accomplished wing hinge angles had to be selected in order to allow them to be manufactured in time for the wind tunnel study. The full dynamic model was still under development, however the model was capable of calculating the aerodynamic forces and moments on tail and

(a)

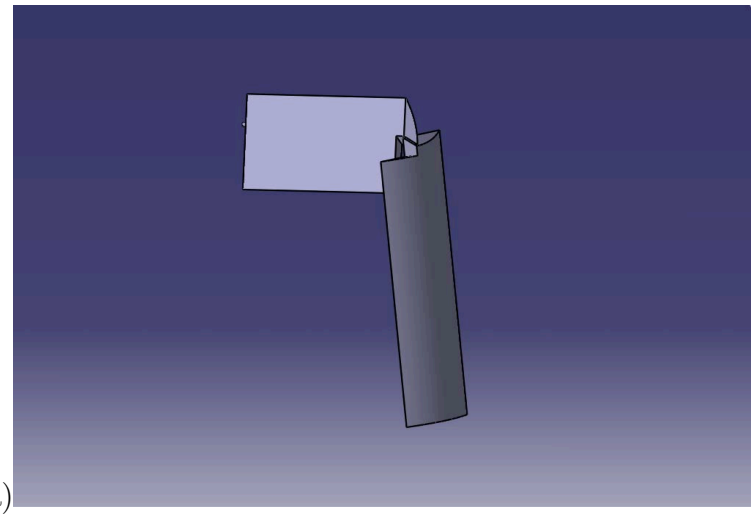

(b)

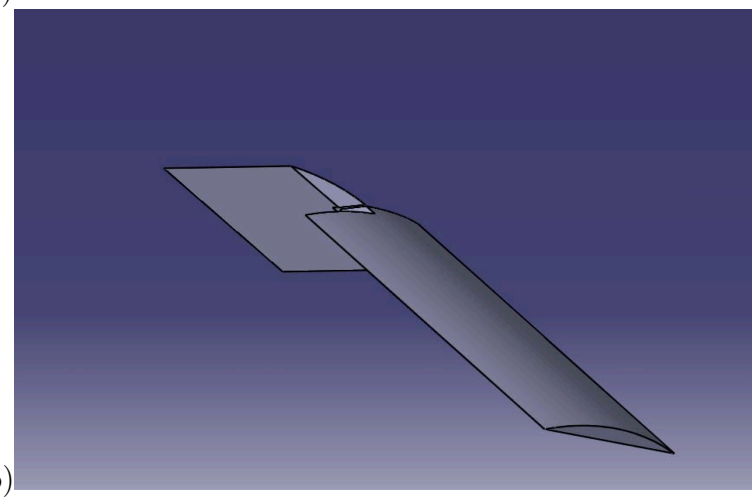

(c)

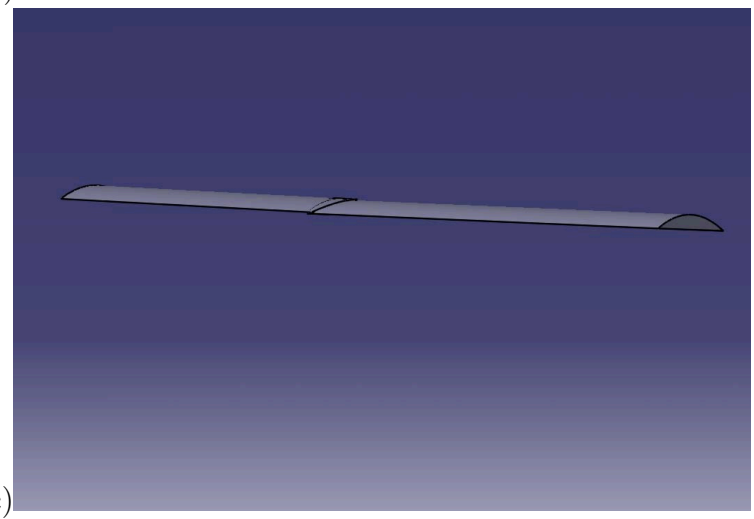

Figure 3.3: Example of CAD model used to determine geometrically feasible wing hinge angles: (a) Wing and mid-section wing hanging vertically during hover; (b) Wing and mid-section wing during the deployment process; (c) Wing and mid-section wing fully deployed.

wing, and was also capable of calculating the moment about the wing and tail hinges. To determine the wing hinge angles most likely to allow for successful wing deployment, a static equilibrium analysis was implemented using the mathematical model described in Chapter 2 to determine the wing and tail settling positions at a given airspeed. These positions were determined by calculating the moment on the tail hinge and wing hinge as the wing and tail deploy, and determining where they equalled zero. In each case, the hinge was located at the 4/10-chord point so that the lift acting at the aerodynamic center (near 1/4-chord) would cause a deployment rotational moment about the hinge. The mathematical model showed that for a given airspeed the wing and tail would deploy as long as there was a positive deploying moment about wing and tail hinges. The wings and tail would continue to deploy until they reach their settling position where the resultant moment on the wing and tail hinge would equal zero. A zero moment on the wing and tail hinge implies that the moments produced by gravity are exactly balanced by the moments from the aerodynamic forces. Therefore, the wings and tail would remained fixed at these equilibrium positions. This model was developed under the assumption that the system was both statically and dynamically stable. That is if the wings and tail were at their equilibrium positions and were perturbed, then they would would then return back to their original equilibrium positions and not diverge.

3.3 Results from the Equilibrium Analysis

Using this static equilibrium analysis, the geometrically feasible wing hinge angles in the ranges $25^\circ \leq \phi_H \leq 50^\circ$ and $25^\circ \leq \theta_H \leq 50^\circ$ were evaluated over 5° increments. The settling positions of the tail and wing where plotted for given wing hinge configuration for airspeeds between 10 and 135 ft/sec. The most likely wing hinge angles that allowed for full aerodynamic deployment were then determined by evaluating those wing hinge angles that allowed the wing to become the closest to fully deployed.

Figure 3.4 shows a plot of roughly how close the wings came to predicted deployment for the evaluated wing hinge angles. The fully deployed wing position is $\psi_H = 0^\circ$ and a fully deployed tail position is $\theta_T = 0^\circ$. The results show that the best wing hinge angle configurations to allow the wing to become the closest to fully deployed were in the range $35^\circ \leq \phi_H \leq 40^\circ$ and $25^\circ \leq \theta_H \leq 40^\circ$. From this evaluation, the hinges that were finally selected for experimental testing were $(\phi_H,\theta_H)=(-35^\circ, 30^\circ)$ and $(\phi_H, \theta_H) = (-40^\circ, 40^\circ)$.

The equilibrium positions for the wing and tail versus airspeed for these two wing hinge angles are shown in Figs. 3.5 and 3.6, respectively. The results show that as the airspeed is increased, the tail progressively comes closer to being fully deployed. In some cases the wings were shown to nearly fully deploy, however, past this point it was predicted that as the tail continues to deploy the wings will de-deploy. This de-deployment of the wings was later observed in the wind tunnel studies, and is a result of the wings not being able to provide sufficient lift because

of the decreasing angles of attack and hence decreasing lift through the kinematics of the entire system as the tail drops down.

For comparison, Fig. 3.7 shows the results for the wing hinge angle of $(\phi_{\mathrm{H}}, \theta_{\mathrm{H}}) = (-30^{\circ}, 25^{\circ})$, where it can be seen that this wing hinge angle is not the best choice. This is because the closest the wings reach to deployment is 47° before the wings de-deploy because of the reduced angles of attack caused by tail deployment.

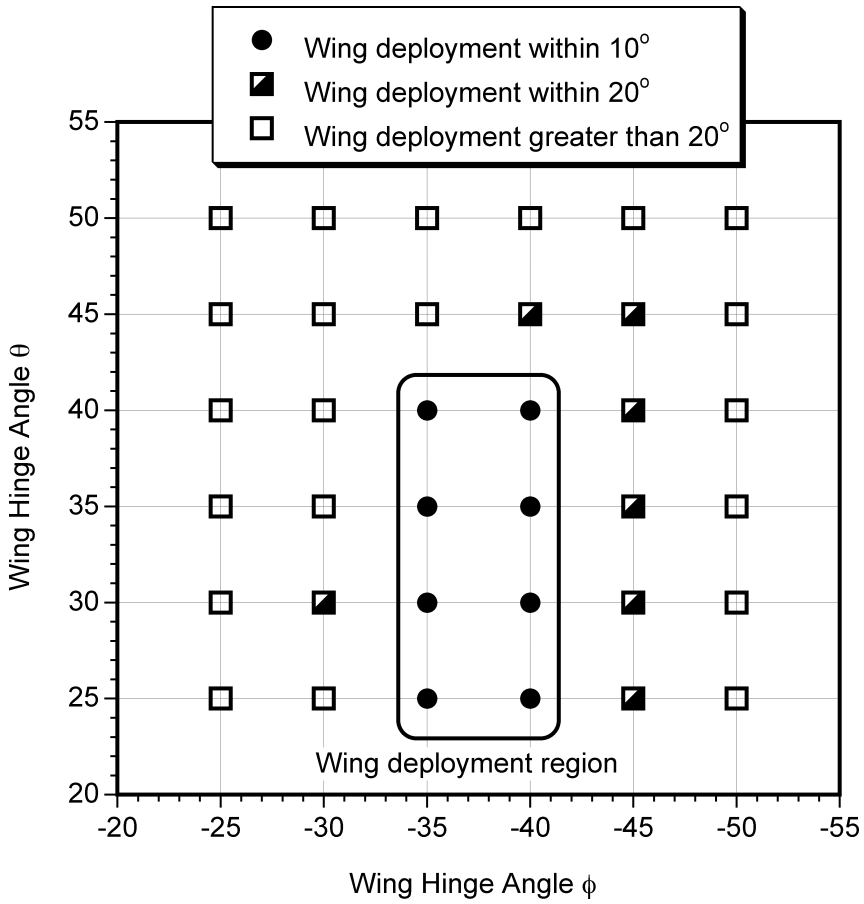

Figure 3.4: Subset of the most likely wing deployment positions over the range of geometrically feasible wing hinge angles.

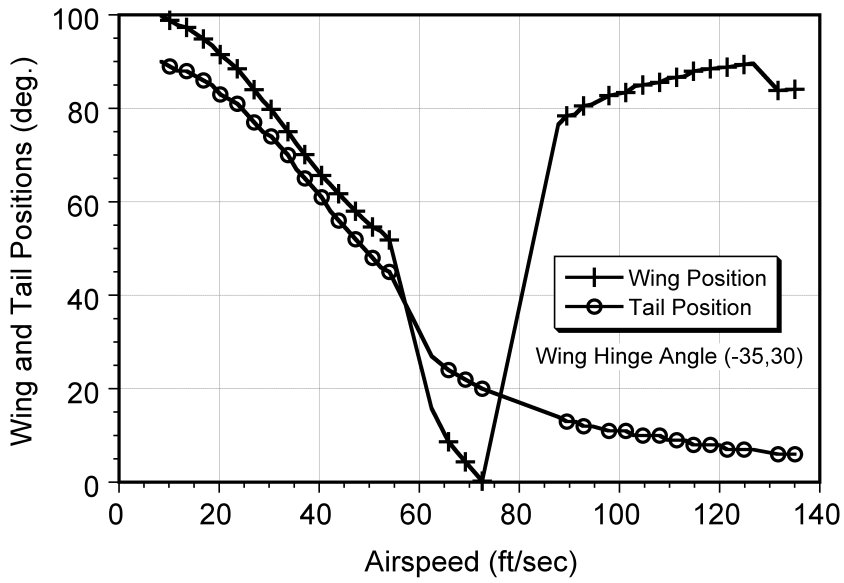

Figure 3.5: Equilibrium positions of the wing and tail versus airspeed for wing hinge angle setting $(\phi_{\mathrm{H}}, \theta_{\mathrm{H}}) = (-35°, 30°)$.

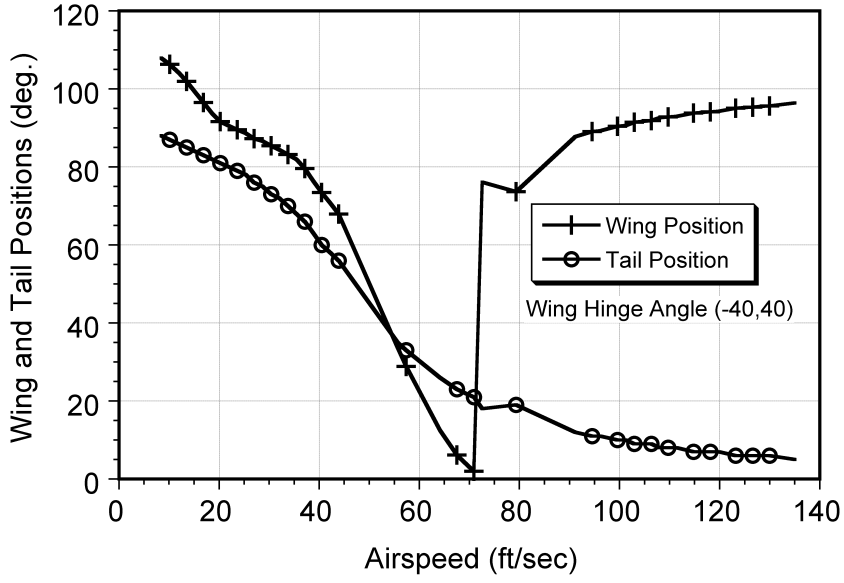

Figure 3.6: Equilibrium positions of the wing and tail versus airspeed for wing hinge angle setting $(\phi_{\mathrm{H}}, \theta_{\mathrm{H}}) = (-40°, 40°)$.

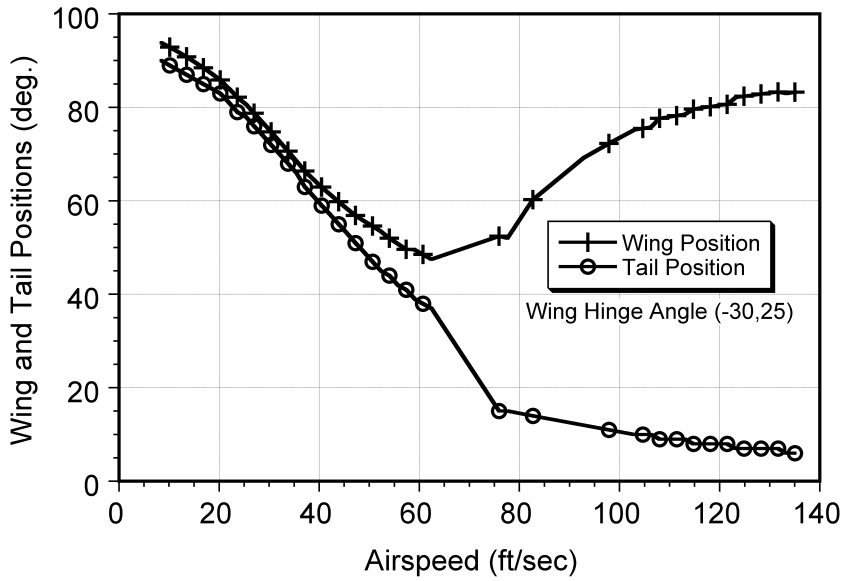

Figure 3.7: Equilibrium positions of the wing and tail versus airspeed for wing hinge angle setting $(\phi_{\mathrm{H}}, \theta_{\mathrm{H}}) = (-30^{\circ}, 25^{\circ})$.

The additional equilibrium plots covering the full range of $25^{\circ} \leq \phi_{\mathrm{H}} \leq 50^{\circ}$ and $25^{\circ} \leq \theta_{\mathrm{H}} \leq 50^{\circ}$ are shown in Appendix A. In some of the plots, especially at the outer boundaries of the geometrically feasible wing hinge angle settings, the mathematical model was not able to converge on a wing or tail equilibrium position. This was particular noticeable around the point at which the wings de-deploy because of the deployment of the tail, as discussed previously. In the next chapter, a description of the wind tunnel study on a sub-scale model using the two optimal wing hinge angles is conducted.

Chapter 4

Wind Tunnel Experiment

In the previous chapter the mathematical model was used to conduct an equilibrium analysis to select two optimal wing hinge angle settings most likely to allow for wing deployment. This chapter discusses the tests that were conducted in the wind tunnel study using the two optimal wing hinge angle settings on a sub-scale model. Also discussed is the drag measurements that were made on the suspended payload units.

The folding wings and the tail of the sub-scale model of the MTR (which has been called the Parametric Research Model or PRM) were tested in the Glenn L. Martin wind tunnel (GLMWT). A photograph of the PRM with the suspended payload unit attached is shown in Fig. 4.1. A primary goal of the testing was to demonstrate the aerodynamic self-deployment of the wings, without any oscillatory or divergent motion.

Displacement transducers positioned in both wing hinges, tail and tail-plane were used to out put a voltage related to their displacements. A customized LabView^{TM} program was developed, which allowed for both the continuous monitoring and recording of all parameters. These voltages are first conditions through an amplifier to remove any noise, sampled using a 12-bit analog-to-digital converter, and then recorded using the LabView^{TM} software.

Figure 4.1: Photograph of the complete wind tunnel model in the Glenn L. Martin wind tunnel.

To calibrate the wing hinge displacement transducers, their voltages were recorded for a series of fixed wing positions. To set the wings at these positions, they were positioned so that there is a certain distance between two defined points on opposite sides of the wing hinge. The distance between the two defined points to correspond with a given wing position was calculated from a CAD model of the PRM. Next, the wings were positioned at these defined positions and the voltages recorded. The tail and tail-plane displacements transducers were calibrated in a similar manner, however their angular positions were measured using a digital level, which measured their angle of inclination. By recording the transducer's voltage output for a series of known wing, tail and tail-plane positions, calibration graphs were determined. From the calibration graphs, suitable curve fits where made to relate the voltage and angular position of a particular parameter. The mathematical formulas describing the curve fits were then entered into the developed LabView^{TM} program. This allowed for an output of angular position.

For the wind tunnel study the PRM was suspended beneath a beam at the ceiling of the wind tunnel. The beam was supported by two pillars on each side of the wind tunnel and these pillars are attached to the balance. The balance measured the three forces and three moments corresponding to a cartesian coordinate system. Balance loads were made with the model in several configurations and for several different operating conditions. Gravity tares were taken for all configurations. A summary of the balance run log is given in Fig. 4.3. Note that Runs 4–10 have been omitted because these became dynamic deployment tests and balance data were not used.

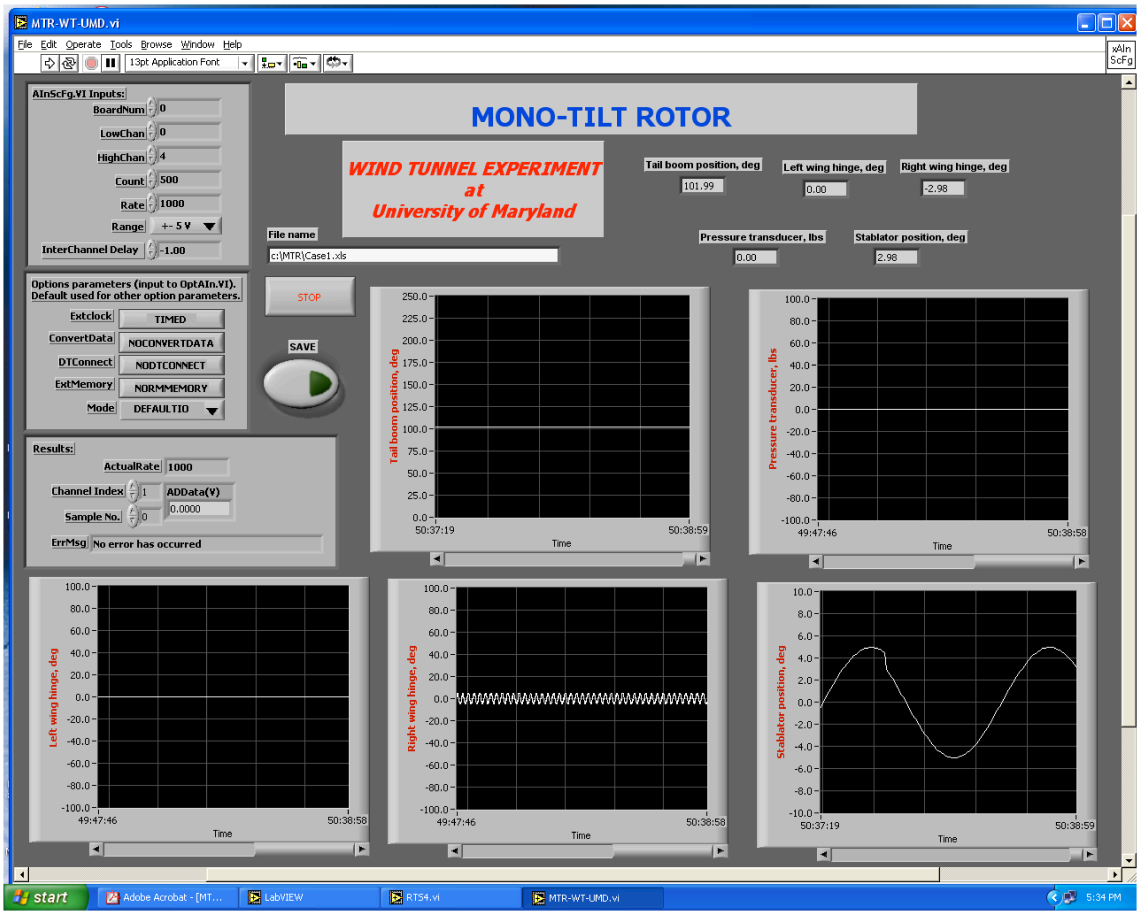

Figure 4.2: LabView program used during testing.

Balance Data Log

Run No.	Wing angle (deg.)	Stab. angle (deg.)	L aileron (deg.)	R aileron (deg.)	Wind speed (ft/s)	Test details and comments
1	n/a	0	n/a	n/a	35 – 60	Tailboom only. Cl data suspect
2	65	0	0	0	35 – 60	Locked wing panels, 10-30 deg range tail position
3	65	0	0	0	35 – 60	Load cell failed & removed, locked wing panels
11	60	0	0	0	50	Wings locked, 50 ft/s
12	60	0	0	0	60	Wings locked, 60 ft/s
13	45	0	0	0	50	Wings locked, 50 ft/s
14	45	0	0	0	60	Wings locked, 60 ft/s
15	45	0	20	20	50	Wings locked, 50 ft/s
16	45	0	20	20	60	Wings locked, 60 ft/s
17	45	0	15	15	50	Wings locked, 50 ft/s
18	45	0	15	15	60	Wings locked, 60 ft/s
19	25	0	0	0	50	Wings locked, 50 ft/s
20	25	0	0	0	60	Wings locked, 60 ft/s
21	10	0	0	0	50	Wings locked, 50 ft/s
22	10	0	0	0	60	Wings locked, 60 ft/s
23	45	0	0	0	50	Wings locked, fences on, 50 ft/s
24	45	0	0	0	60	Wings locked, fences on, 60 ft/s
25	45	0	-5	-5	50	Wings locked, fences on, 50 ft/s
26	45	0	-5	-5	60	Wings locked, fences on, 60 ft/s
27	45	0	0	0	50	Wings locked, fences on, small payload unit, 50 ft/s
28	45	0	0	0	60	Wings locked, fences on, small payload unit, 60 ft/s
29	25	0	0	0	50	Wings locked, fences on, small payload unit, 50 ft/s
30	25	0	0	0	60	Wings locked, fences on, small payload unit, 60 ft/s
31	10	0	0	0	50	Wings locked, fences on, small payload unit, 50 ft/s
32	10	0	0	0	60	Wings locked, fences on, small payload unit, 60 ft/s
33	10	0	0	0	50	Wings locked, fences on, large payload unit, 50 ft/s
34	10	0	0	0	60	Wings locked, fences on, large payload unit, 60 ft/s
35	25	0	0	0	50	Wings locked, fences on, large payload unit, 50 ft/s
36	25	0	0	0	60	Wings locked, fences on, large payload unit, 60 ft/s
37	45	0	0	0	50	Wings locked, fences on, large payload unit, 50 ft/s
38	45	0	0	0	60	Wings locked, fences on, large payload unit, 60 ft/s
39	0	0	0	0	50	Wings fully deployed, fences on, large payload unit, 50 ft/s
40	0	0	0	0	60	Wings fully deployed, fences on, large payload unit, 60 ft/s
41	10	0	0	0	50.5	Wings locked, fences on, 50.5 ft/s
42	25	0	0	0	50.5	Wings locked, fences on, 50.5 ft/s
43	45	0	0	0	50.5	Wings locked, fences on, 50.5 ft/s
44	45	5	0	0	50.5	Wings locked, fences on, 50.5 ft/s
45	45	-15	0	0	50.5	Wings locked, fences on, 50.5 ft/s
46	n/a	0	0	0	50.5	Wings and hinges removed, center wing only, 50.5 ft/s
47	45	0	0	0	50.5	2nd hinge, wings locked, fences on, 50.5 ft/s
48	25	0	0	0	50.5	2nd hinge, wings locked, fences on, 50.5 ft/s
49	10	0	0	0	50.5	2nd hinge, wings locked, fences on, 50.5 ft/s
50	0	0	0	0	50.5	2nd hinge, wings fully deployed, fences on, 50.5 ft/s
51	45	5	10	-10	50.5	2nd hinge, wings locked, fences on, 50.5 ft/s
52	45	-15	10	-10	50.5	2nd hinge, wings locked, fences on, 50.5 ft/s
53	25	-15	-10	10	50.5	2nd hinge, wings locked, fences on, 50.5 ft/s
54	25	5	-10	10	50.5	2nd hinge, wings locked, fences on, 50.5 ft/s
55	45	0	-10	10	50.5	2nd hinge, wings locked, fences on, 50.5 ft/s
56	45	0	10	-10	50.5	2nd hinge, wings locked, fences on, 50.5 ft/s
57	10	0	10	-10	50.5	2nd hinge, wings locked, fences on, 50.5 ft/s
58	10	0	-10	10	50.5	2nd hinge, wings locked, fences on, 50.5 ft/s
59	10	0	0	0	50.5	Model yawed 3 degrees to starboard, 50.5 ft/s
60	10	0	-10	10	50.5	Model yawed 3 degrees to starboard, 50.5 ft/s
61	25	0	-10	10	50.5	Model yawed 3 degrees to starboard, 50.5 ft/s
62	25	0	0	0	50.5	Model yawed 3 degrees to starboard, 50.5 ft/s
63	45	0	0	0	50.5	Model yawed 3 degrees to starboard, 50.5 ft/s
64	45	0	-10	10	50.5	Model yawed 3 degrees to starboard, 50.5 ft/s
65	0	0	0	0	50.5	Solid wing ONLY
66	0	0	0	0	50.5	Solid wing, large payload, 50.5 ft/s
67	n/a	0	n/a	n/a	50.5	Tailboom only. Repeat of Run 1
68	n/a	n/a	n/a	n/a	q sweep	Model support + struts + large payload unit
69	n/a	n/a	n/a	n/a	q sweep	Model support ONLY
70	n/a	n/a	n/a	n/a	q sweep	Model support + struts + small payload unit
71	n/a	n/a	n/a	n/a	q sweep	Model support + 2 vertical struts only

Figure 4.3: Run log for balance data.

4.1 Static Measurements

The first set of tests measured the lift, drag and moments acting on the just the tail of the PRM for a range of tail positions between 0° and 90° in 2° increments. A photograph of just the tail assembly is shown in Fig. 4.4. Next, this same test was repeated with the addition of the mid-section wing. The wings were then added and the test repeated for both wing hinge angle configurations and with the wings locked at 0°, 10°, 25° and 45°. This allowed the aerodynamic forces and moments to be measured as a function of tailboom position; these results were essential for the validation of the mathematical model describing the deployment process.

Measurements were made with both sets of wing hinges. Representative photographs of the PRM with the wings locked at the 25° position and the 45° position are shown in Figs. 4.5 and 4.6, respectively.

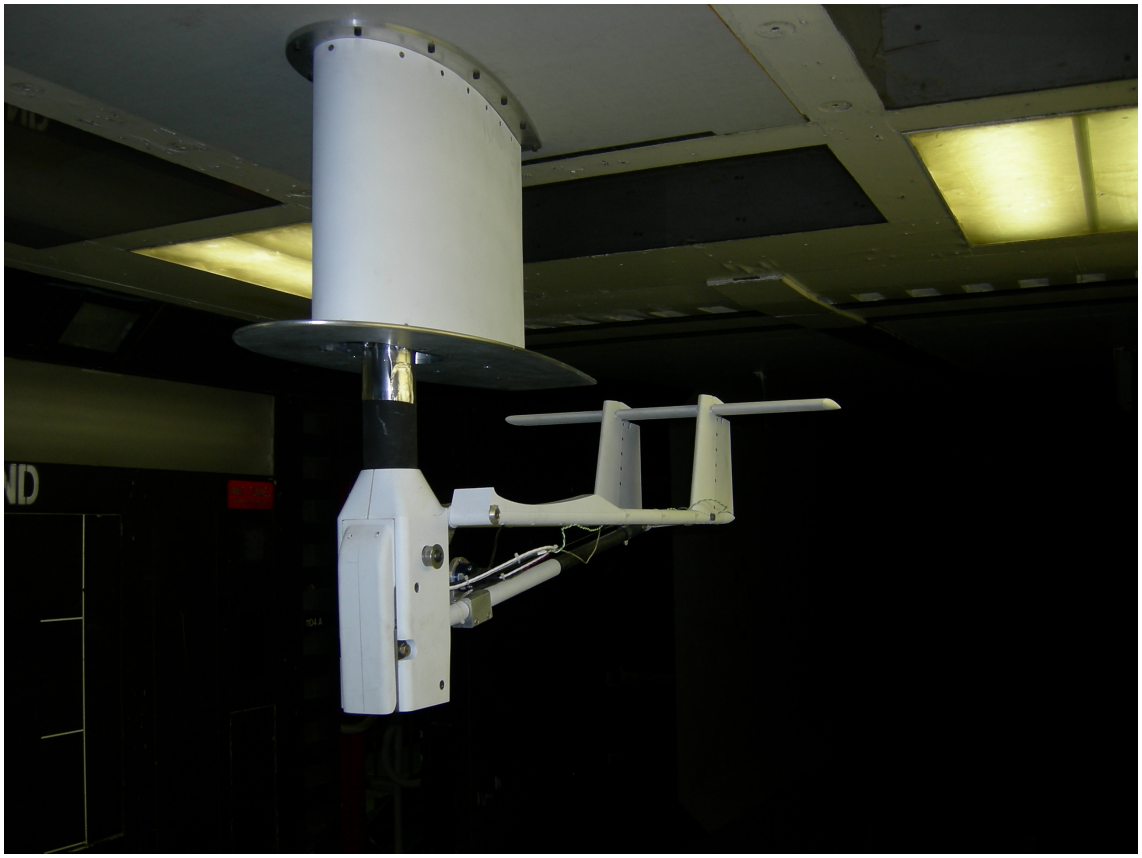

Figure 4.4: Photograph of the tail assembly of the PRM, with tail locked up in the fully deployed position.

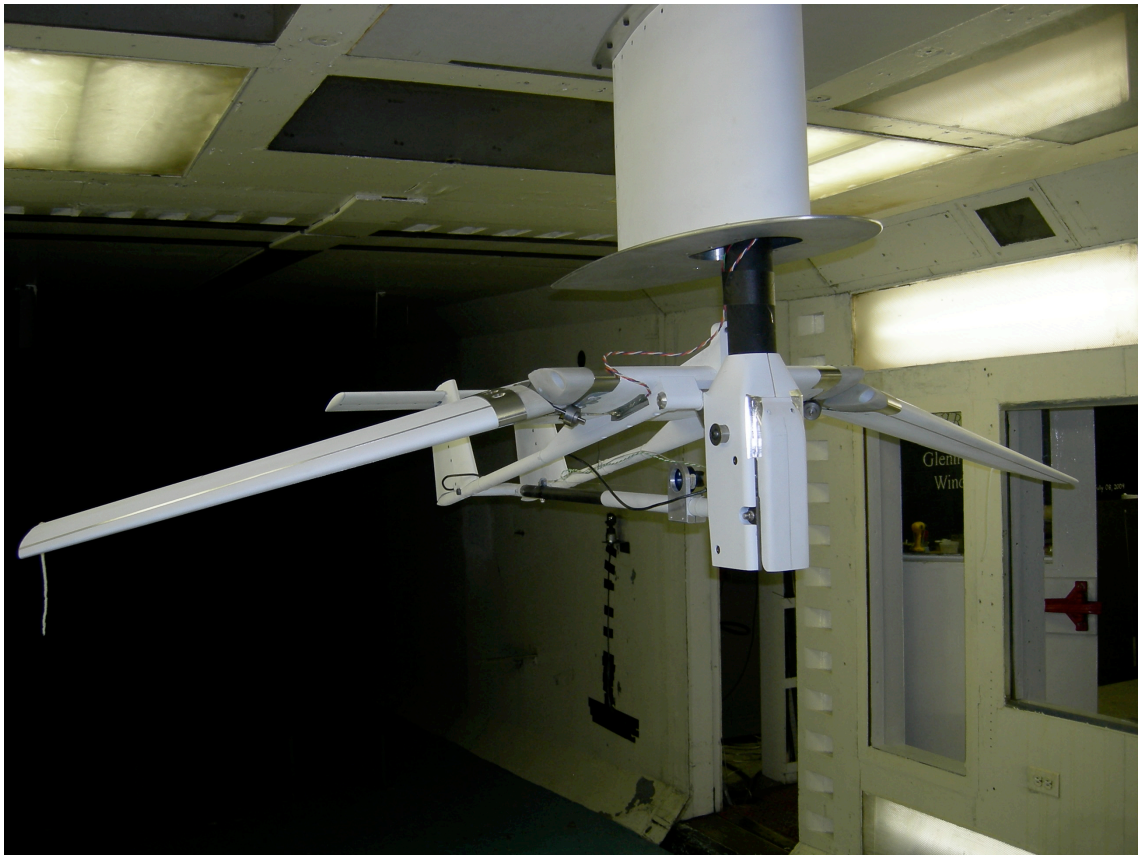

Figure 4.5: Wings installed on the PRM and locked at the 25° position.

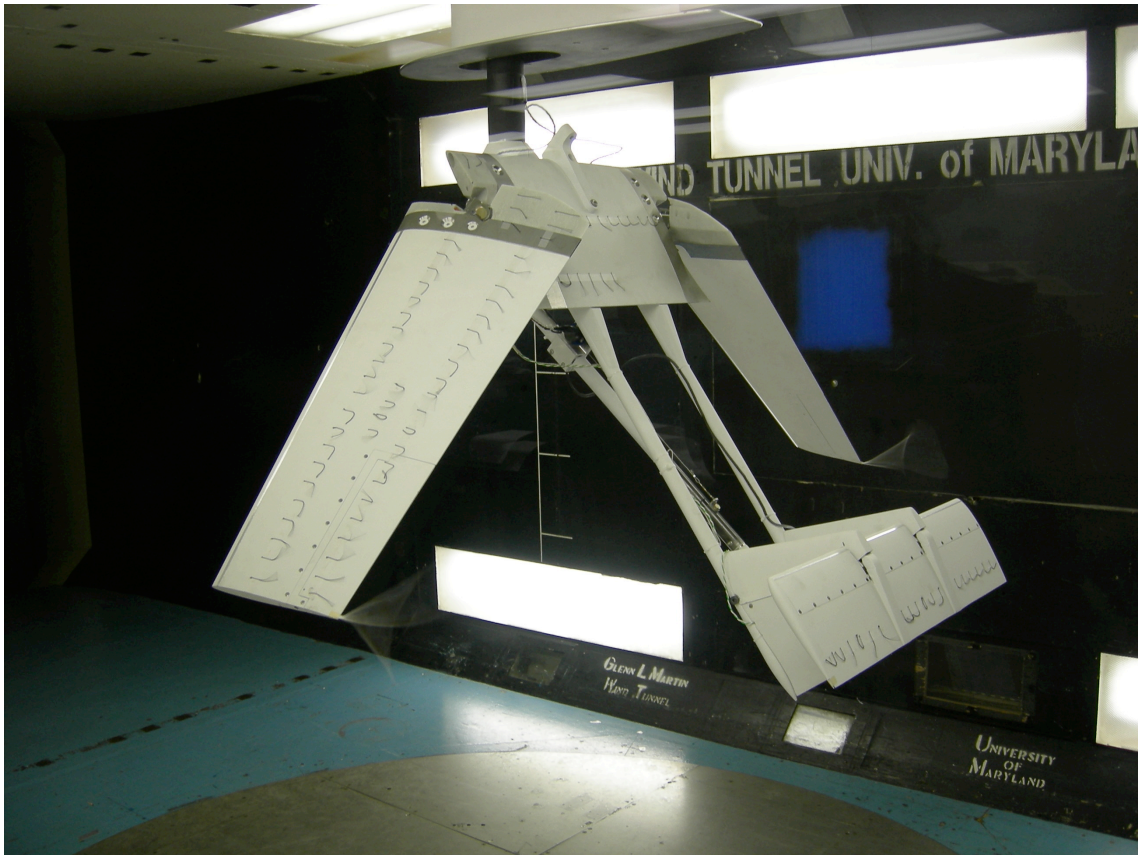

Figure 4.6: Wings installed on the PRM and locked at the 45° position.

4.2 Dynamic Measurements

A significant number of experiments were conducted to examine the dynamic, free deployment of the wings. This included the effects of wind speed, tail position, and aileron settings. Several combinations of conditions were found to produce successful wing deployment.

In the first instance, the friction locks on the wings were released, but retightened to values that allowed for some damping. The damping was checked by performing a "drop test" on both wings, where they were held almost at their fully-deployed position with the wind off and then simultaneously released. The wind speed was then increased to 55 ft/sec and tail raised to the deployed position of 0°. The tail was then lowered down at a constant rate until the wings deployed up into position, this usually occured at a tail position of approximately 30°. The dynamic responses of both wings were measured, and the damping on the hinges was then adjusted to achieve both the required value of damping, as well as a symmetric response with both wing panels responding essentially identically. The use of some positive (downward) aileron deflections was found to aid in the wing deployment, mainly by producing deployment at a lower tailboom angle and/or at a lower wind speed. Some minor differential deployment of the ailerons also helped to ensure symmetric wing deployment.

Representative results of the deployment are shown in Fig. 4.7, which are a series of still images taken from the digital video tape. The wings were found to deploy relatively slowly at first (either with increasing tailboom angle or with

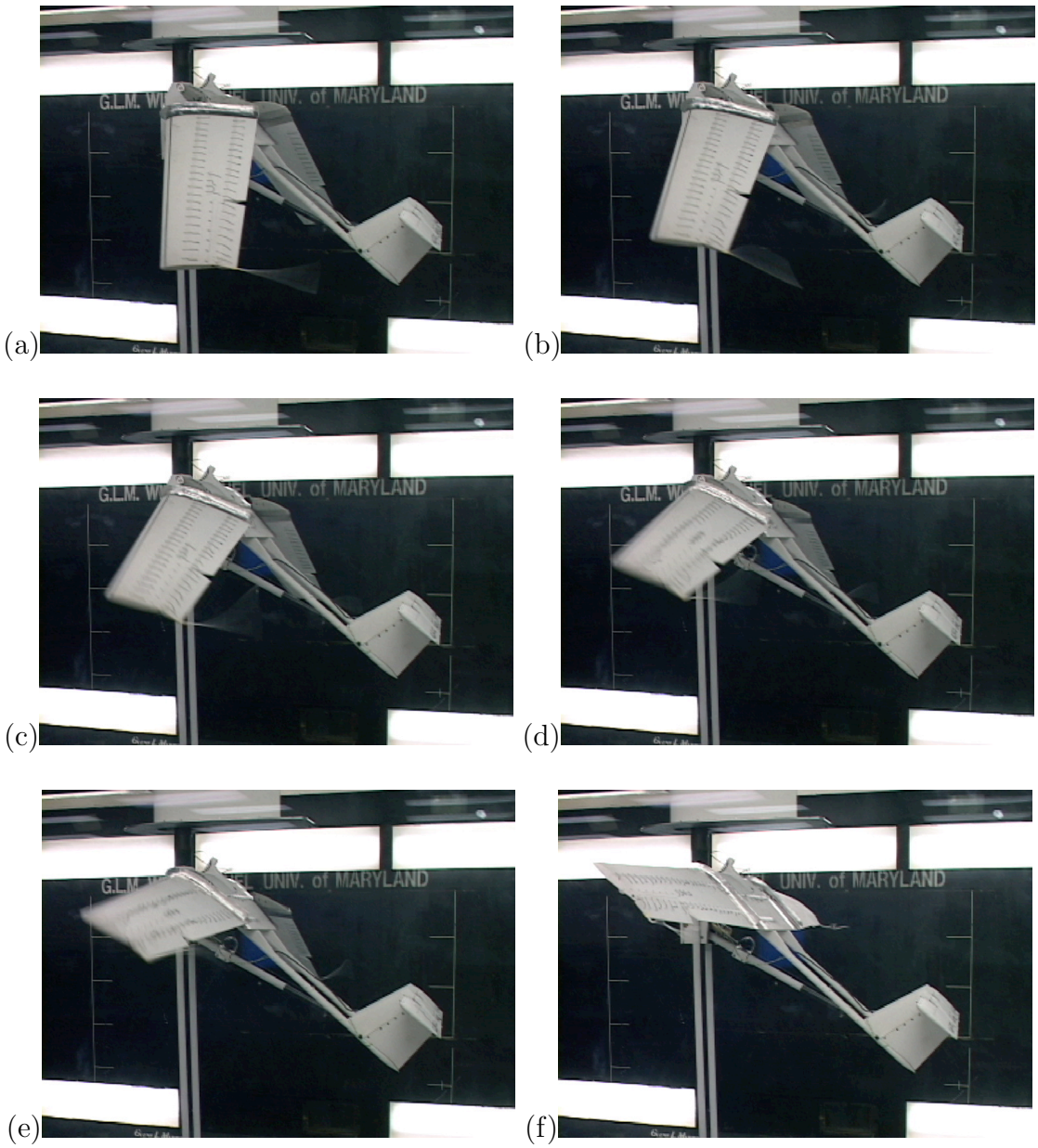

Figure 4.7: Sequence of still images taken from the digital video showing the wing deployment: (a) Wings at approximately 70°; (b) Wings at approximately 60°; (c) Wings at approximately 40°; (d) Wings at approximately 30°; (e) Wings at approximately 20°; (f) Wings fully deployed.

increasing airspeed), but thereafter they deployed relatively quickly (over a period of about 3 seconds) and locked into their final position.

Mini-tufts were also applied to the wings, which showed the development of stall patterns as the wings passed through critical angle of attack and sweep angle regions. It was immediately apparent that flow separation from the inboard wing panel and at the wing hinges and joints was causing the inboard regions of the outer wing panels to stall prematurely, losing lift and increasing drag. This was rectified by the addition of fences on the outer wing panels that were located just outboard of the wing hinges; these fences created a stable vortex flow and were extremely effective in delaying premature flow separation on the outer wing panels. The fences were also found to give to a much more controlled and repeatable wing deployment, and were thus retained for the remainder of the tests.

4.3 Payload Units

Figures 4.8 (a) and (b) show photographs of the MTR in the wind tunnel with the small and large payload units attached. A series of flow visualization experiments were conducted to examine flow patterns on the payload units. A mixture of titanium dioxide power and mineral oil was smeared evenly over each unit. The wind was turned on for 5 minutes to allow the flow patterns to develop, and then photographs were taken with the wind off. A photograph of the small payload unit with developed flow patterns is shown in Fig. 4.9.

It is apparent from the photographs that there is laminar flow over the fore-

(a)

(b)

Figure 4.8: MTR in windtunnel with: (a) small payload unit attached; (b) large payload unit attached.

body up until it meets the corner where it attaches with the rectangular payload box – see Fig. 4.10. At this point, a laminar separation bubble can be noted. The

flow downstream of the laminar separation bubble reattaches as a turbulent boundary layer. The flow is then shown to stay attached a short distance downstream before separating. Approximately 60 % of flow over the payload unit was separated. Secondary flow structures can be noted at the tail and tail cone – see Fig. 4.11.

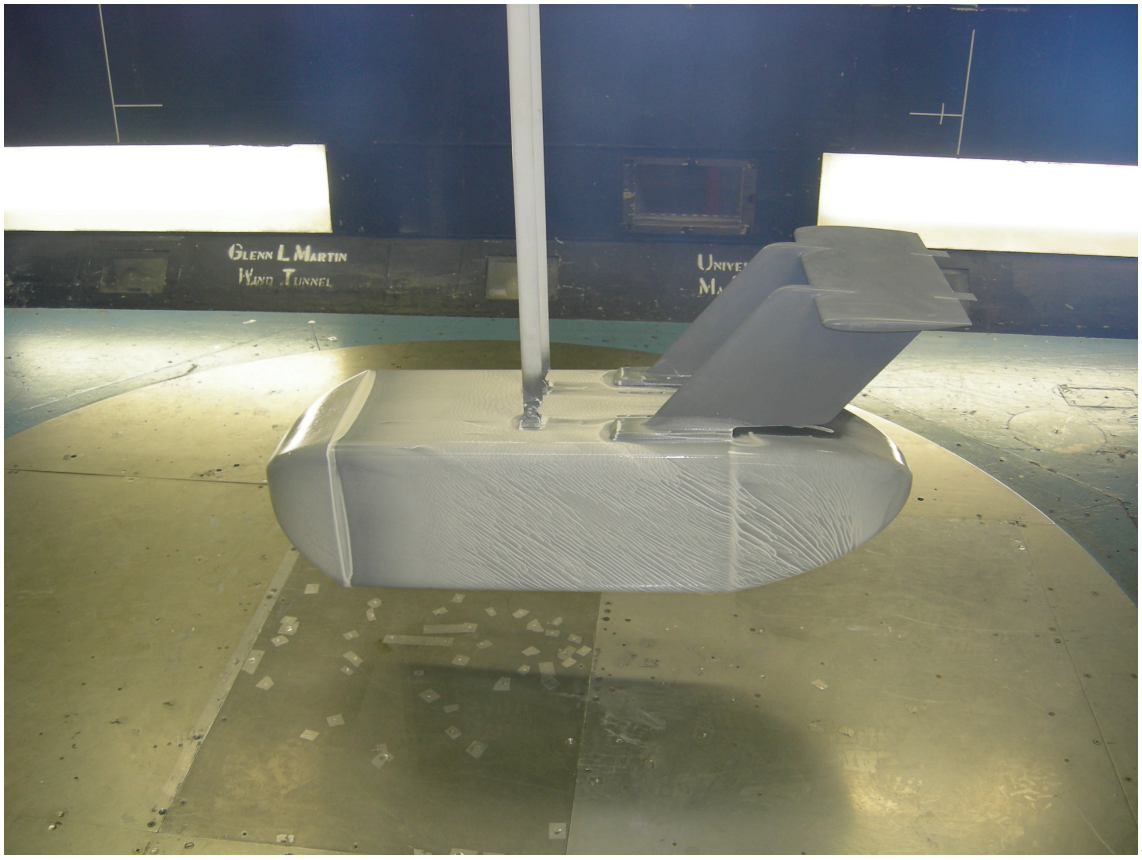

Figure 4.9: Example of oil flow visualization on the small payload unit.

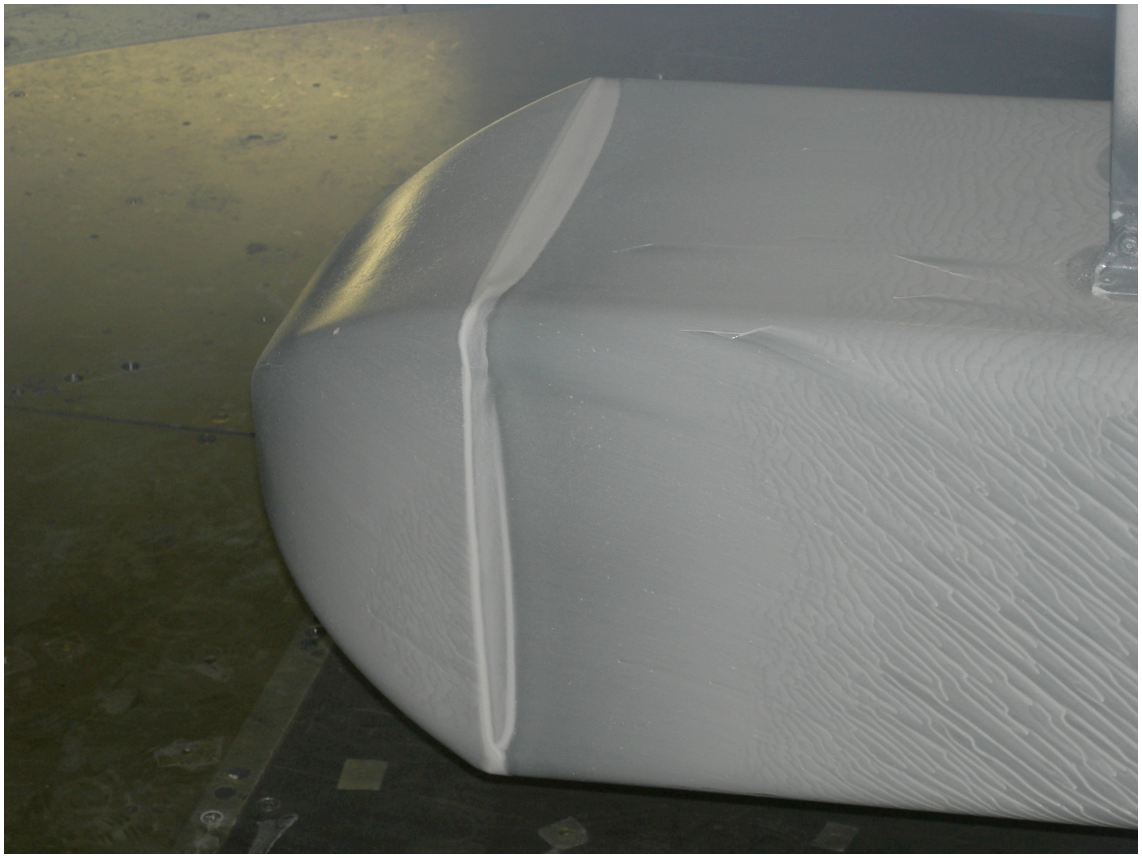

Figure 4.10: Detail of oil flow visualization at the nose of the small payload unit.

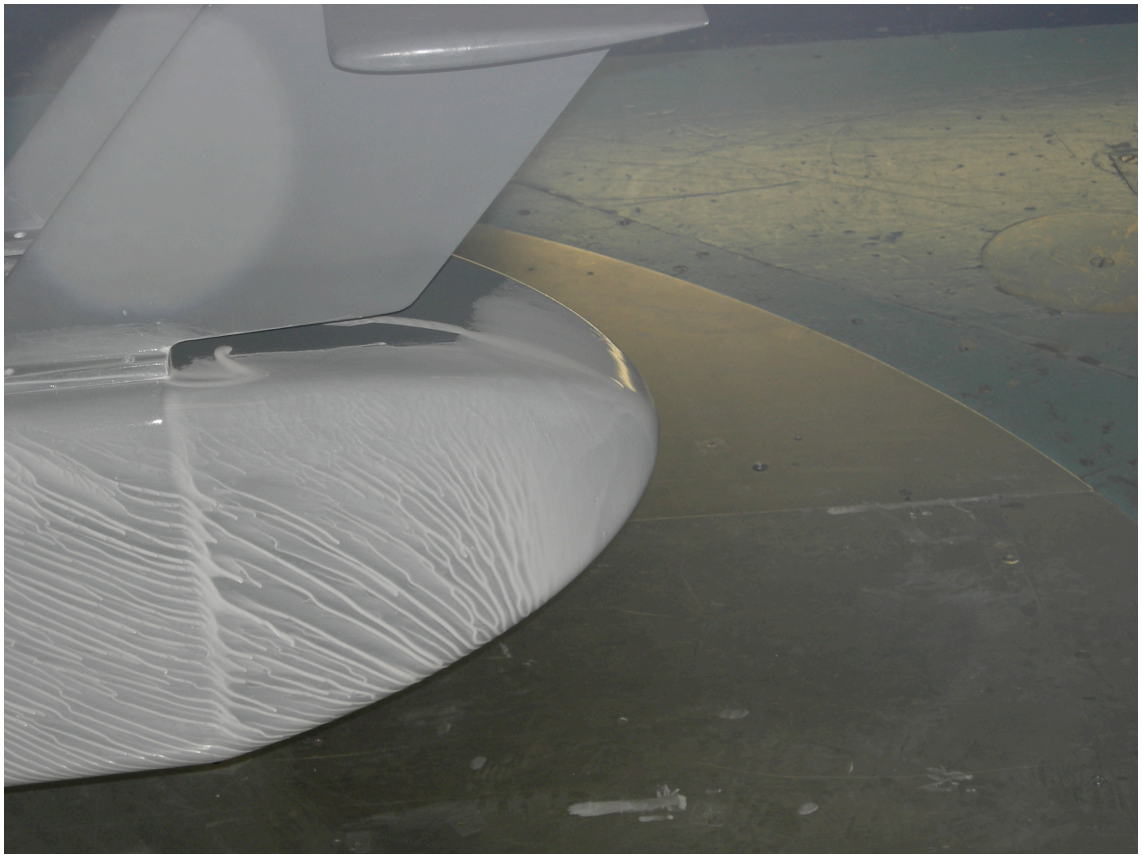

Figure 4.11: Detail of oil flow visualization at the tail of the small payload unit showing separated flow.

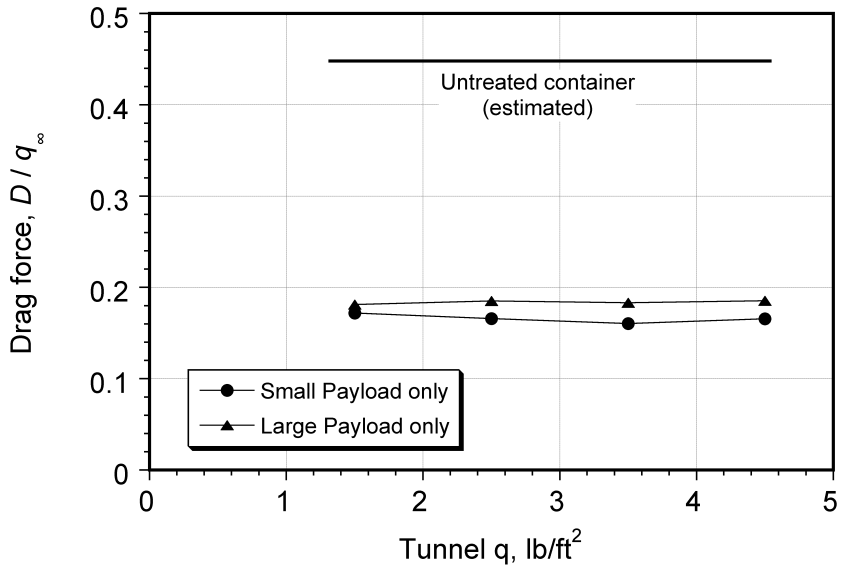

Figure 4.12: Breakdown of measured drag force for support, struts, small payload and large payload.

The measured drag force for the small and large payload units in comparison to an untreated rectangular container is shown in Fig. 4.12. From the measured data it appears that the large payload section produces slightly more drag then the small payload unit. The large payload produced slightly more drag because it was longer and hence produced more skin friction drag. A majority of the drag for both the small and large payload units can be attributed to pressure drag. It is shown that overall by incorporating rounded leading and trailing edges into the payload unit the total drag in comparison to an untreated container (flat leading and trailing edges) is less than half [12].

Chapter 5

Discussion of Results

The previous chapter discusses the tests that were conducted in the wind tunnel study. In this chapter the results from measurements with static configurations of the sub-scale model are compared to the predicted results obtained with the mathematical model. The goal was to show that the mathematical model is capable of predicting lift, drag and moment forces with good correlation to the measured data.

5.1 Tail and Mid-Section Wing

The predicted and measured lift, drag, and pitching moment for just the tail, and for the tail and mid-section wing are shown in Figs. 5.1 and 5.2, respectively. The correlation to the measured data was improved after a series of corrections to the lift curve slope data in the mathematical model were used to account for the finite aspect ratio, lower Reynolds number, and three-dimensional interference effects.

Figure 5.1 shows the lift, drag, and moment plots for the measured and calculated data with the tail only. There is good correlation of the model with measurements of the lift and drag over the range of 0° to 90° tail boom position. A small difference between measured and calculated data was noted around the 20°

tail boom position, which corresponds to the onset of stall on the tail. The pitching moment data also correlates well, there being only a slight difference between measured and calculated data at high angles of attack.

Figure 5.2 shows the lift, drag and moment for the mid-section wing and tail. The predicted and measured data correlates very well up until the tail stalls and the flow separates on the mid-section part of the wing. In the post-stall regime, the predicted and measured drag force and pitching moments differed, especially at the highest angles of attack. These differences are primarily associated with the mid-section part of the wing, which based on flow visualization involved three-dimensional flow separation and stalled regions.

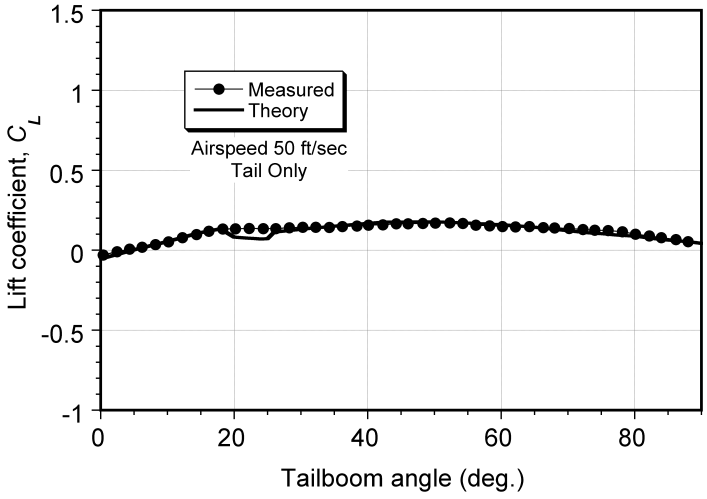

(a)

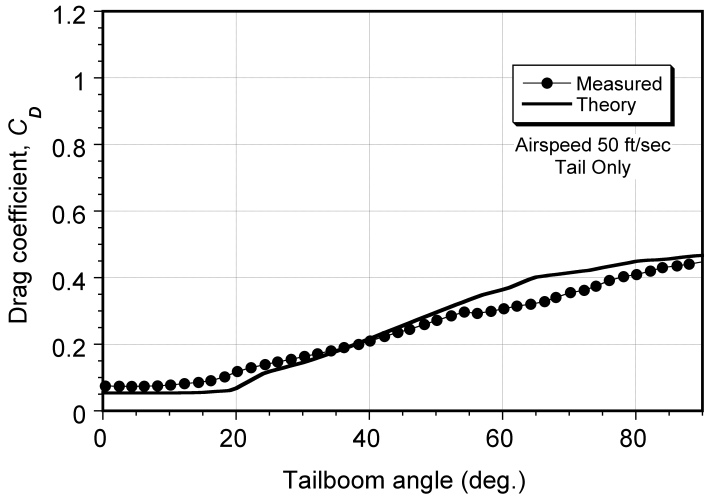

(b)

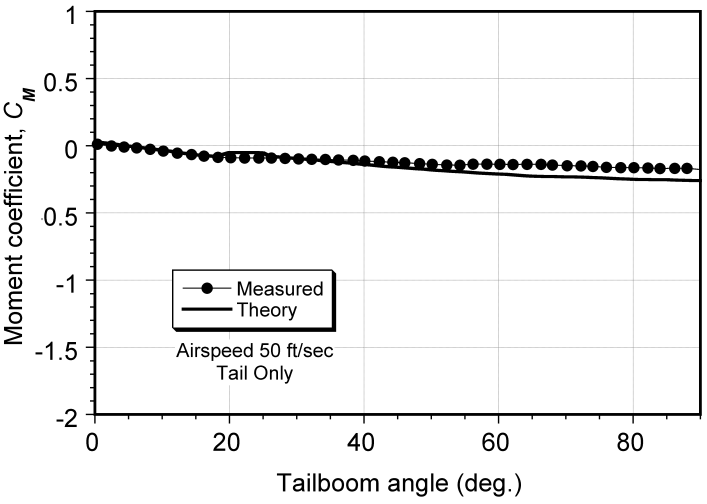

(c)

Figure 5.1: Lift, drag and pitching moment produced from the tail only versus tail boom position.

5.2 Full Configuration with Outer Wing Panels

As described in the previous section, several sets of balance measurements were made with the wings locked at fixed positions. This allowed the quasi-steady aerodynamic forces and pitching moments to be measured as a function of tailboom position.

With the wings fully deployed, the force and pitching moment characteristics were found to be typical of any finite wing. The deployment of the wings from their locked position changes the relationship between the wing angle of attack and the tailboom position, and so a series of different force and moment curves were obtained for different fixed wing positions. There was also a substantial increase in drag as the wing deploys; this is partly a result of the complex three-dimensional flow separation that occurs at the wing joint.

Figure 5.3 shows the lift, drag, and moment coefficient results with the wings locked at 0° with a wing hinge angle setting of $(\phi_{\mathrm{H}}, \theta_{\mathrm{H}}) = (-40^\circ, 40^\circ)$. There is overall a good correlation between the predictions and the measurements, but again, in the post-stall region some differences were noted.

Figure 5.4 shows the lift, drag and moment coefficient plots with the wings locked at 10° with a wing hinge angle setting of $(\phi_{\mathrm{H}}, \theta_{\mathrm{H}}) = (-40^\circ, 40^\circ)$. The lift curve slope predictions here showed an excellent correlation with the measurements up until stall. The drag and moment results also showed good correlation up until stall, which was encouraging despite the complexities of the flow state and the relative simplicity of the mathematical model (aerodynamic strip theory).

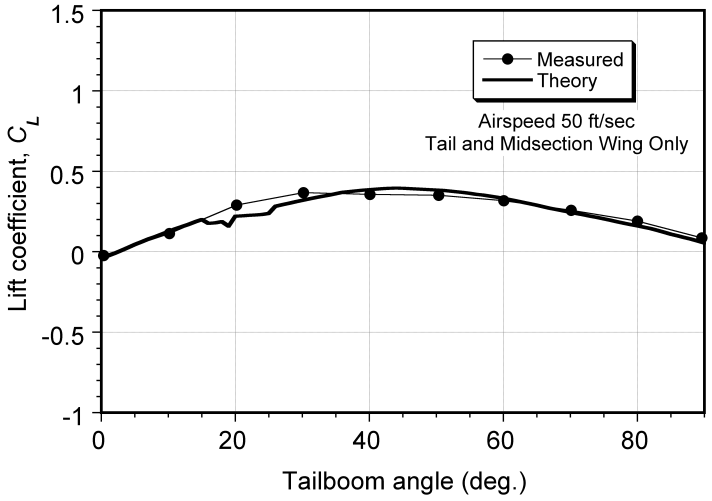

(a)

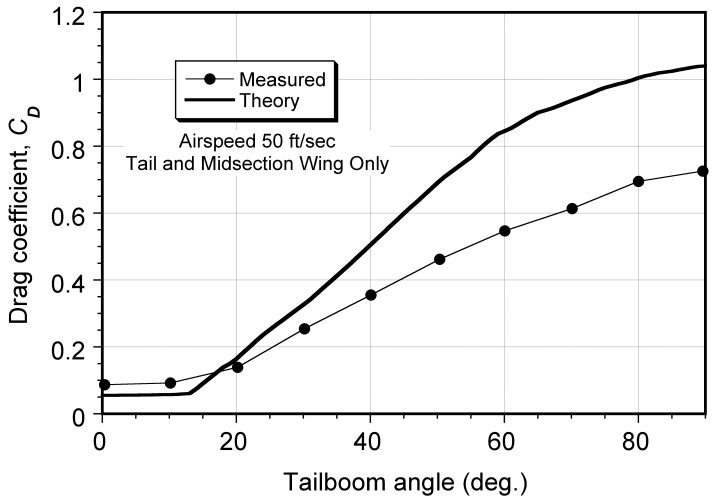

(b)

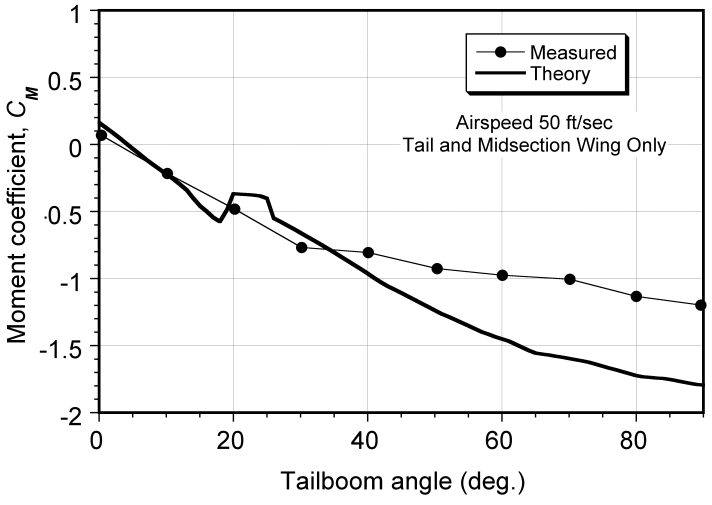

(c)

Figure 5.2: Lift, drag and pitching moment produced from the tail and mid-section wing only versus tail boom position.

Figure 5.5 shows the lift, drag and moment plots with the wings locked at 25° with a wing hinge angle setting of $(\phi_H, \theta_H) = (-40°, 40°)$. In this case there were slight differences noted between the measured and calculated results. The differences can be associated with the increasing hinge gap.

Figure 5.6 shows the lift, drag and moment plots with the wings locked at 45° with a wing hinge angle setting of $(\phi_H, \theta_H) = (-40°, 40°)$. The difference seen between the measured and calculated lift, drag, and moment data continue to increase with increased wing hinge angle setting. These differences can be attributed to the interference effects that are created resulting from flow separation at the wing joint and also because of the high wing sweep angle, which generates significant spanwise flow and three-dimensional post-stall airloads. Also note that the wing lift break (stall) occurs at around the 35° tail boom position.

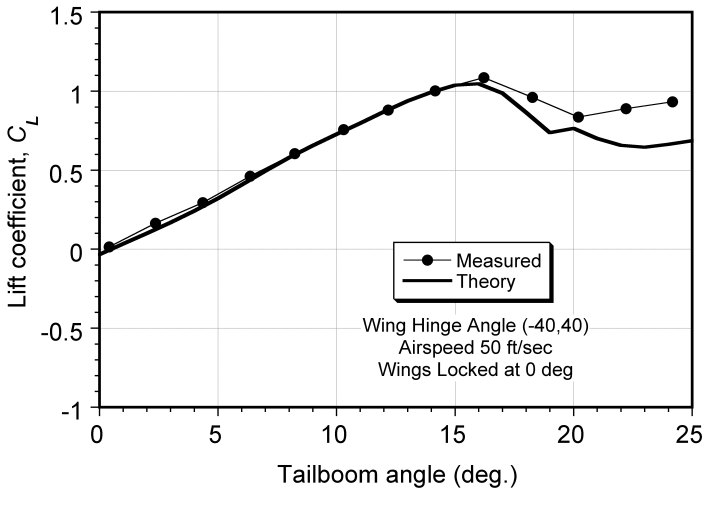

(a)

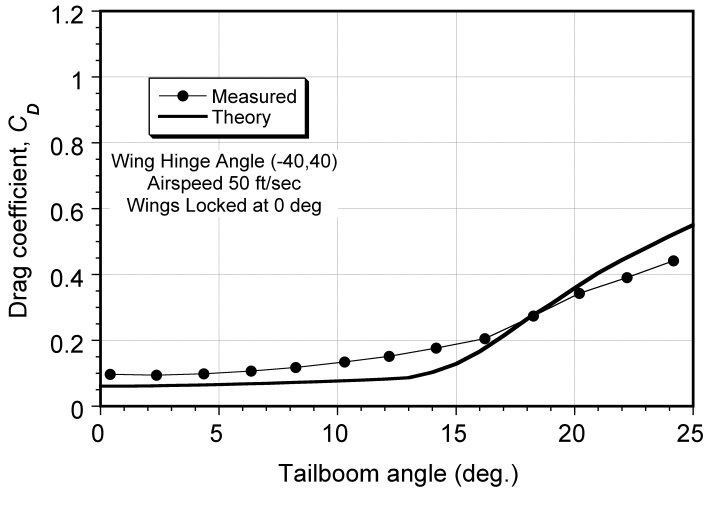

(b)

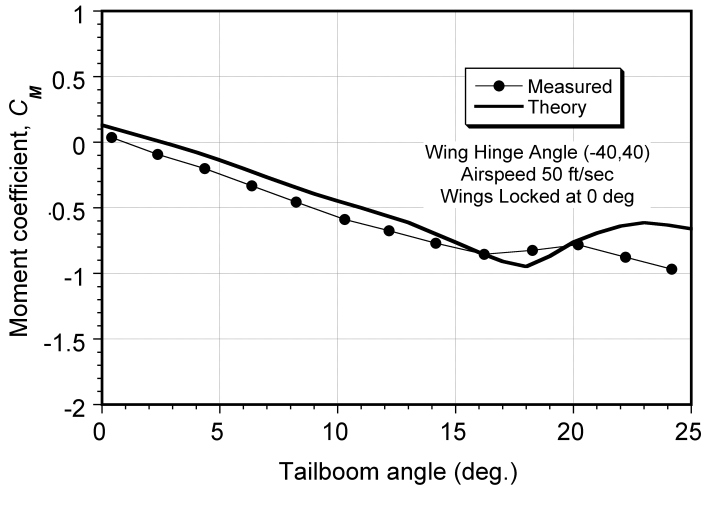

(c)

Figure 5.3: Lift, drag and pitching moment versus tail boom position. Wings locked at 0°, wing hinge angle of $(\phi_{\mathrm{H}}, \theta_{\mathrm{H}}) = (-40°, 40°)$.

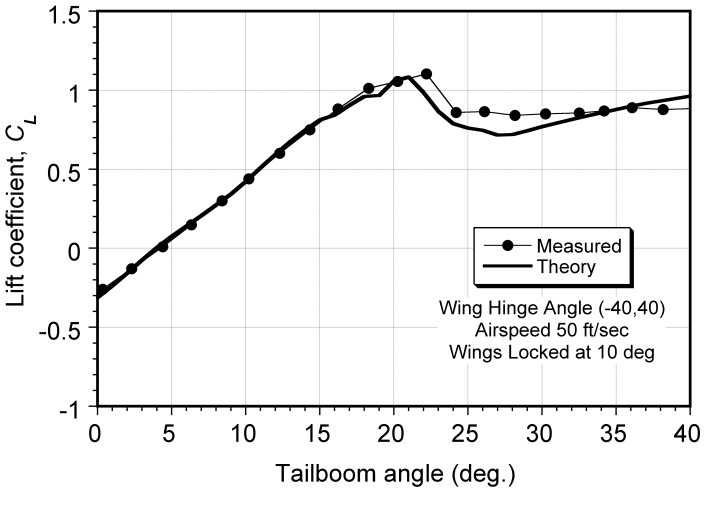

(a)

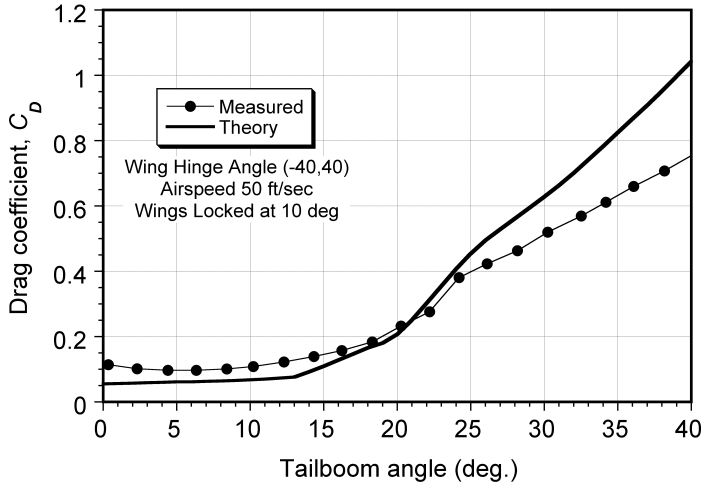

(b)

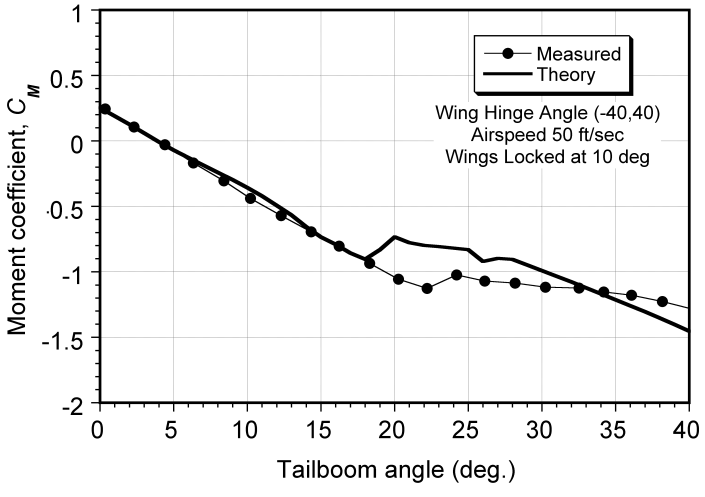

(c)

Figure 5.4: Lift, drag and pitching moment versus tail boom position. Wings locked at 10°, wing hinge angle of $(\phi_{\mathrm{H}}, \theta_{\mathrm{H}}) = (-40°, 40°)$.

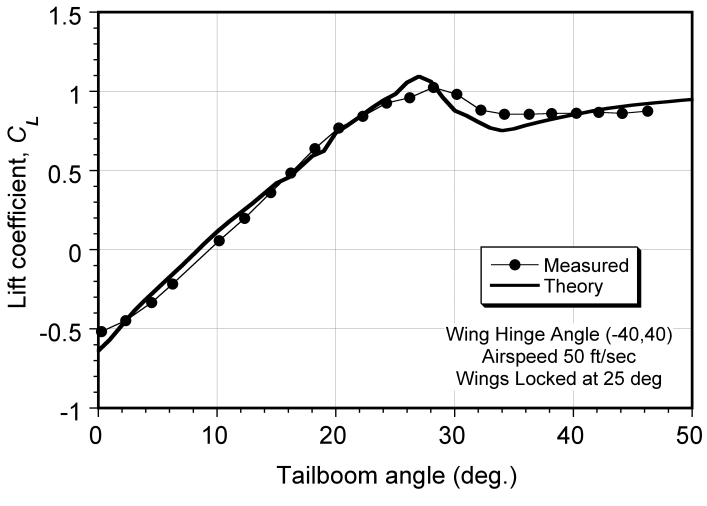

(a)

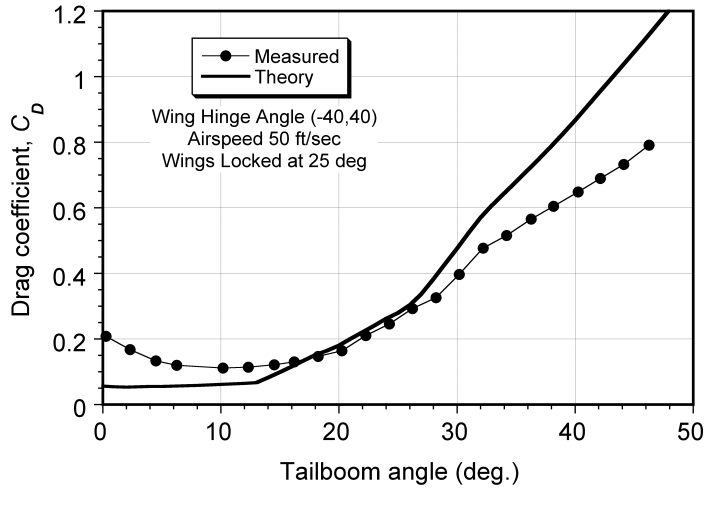

(b)

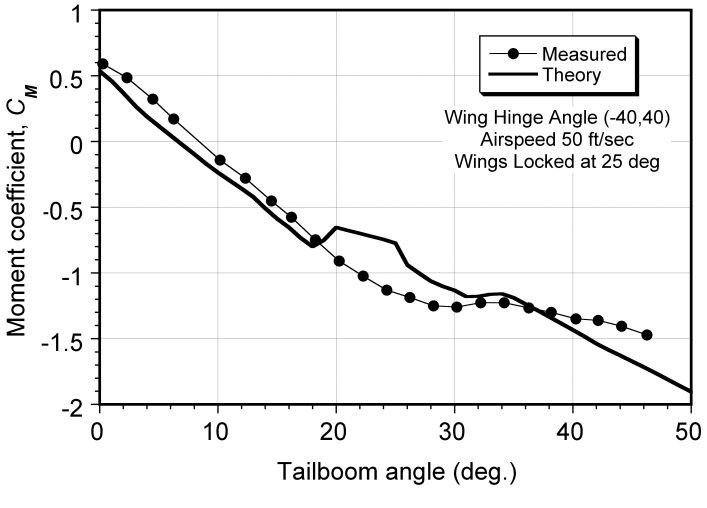

(c)

Figure 5.5: Lift, drag and pitching moment versus tail boom position. Wings locked at 25°, wing hinge angle of $(\phi_{\mathrm{H}}, \theta_{\mathrm{H}}) = (-40°, 40°)$.

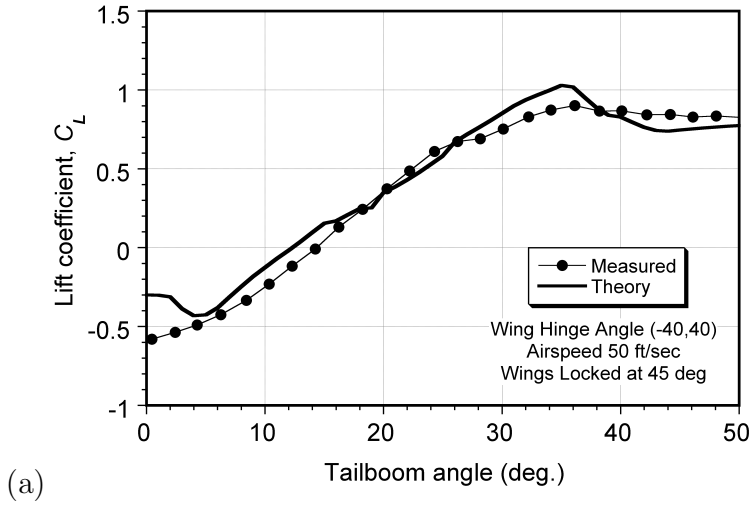

(a)

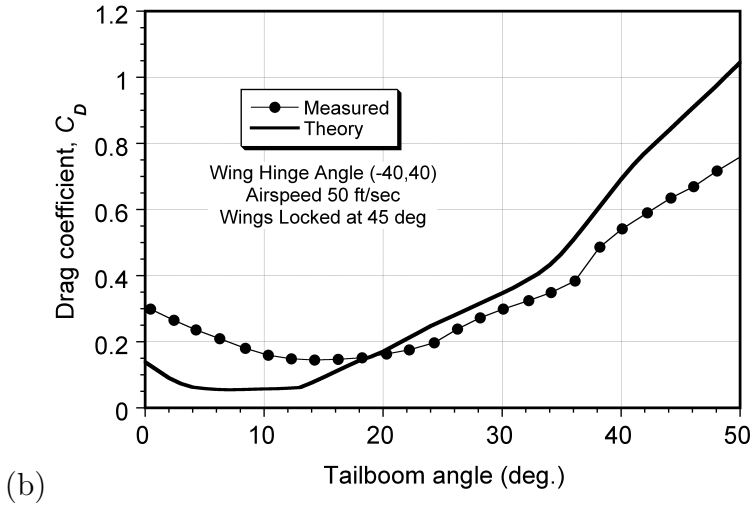

(b)

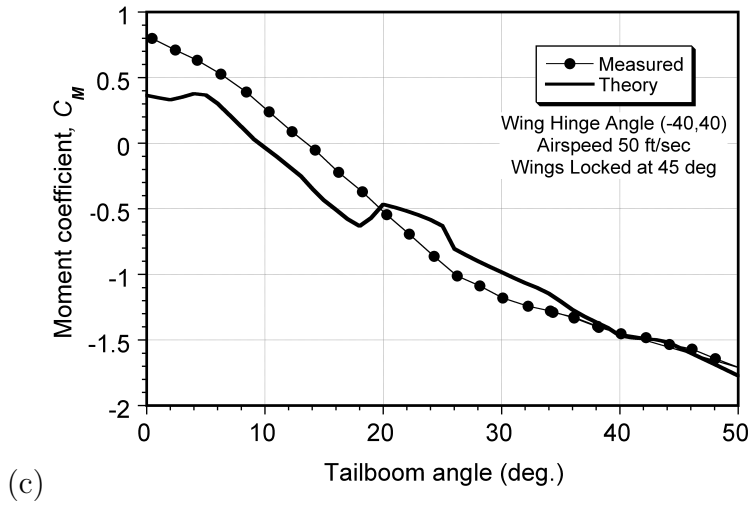

(c)

Figure 5.6: Lift, drag and pitching moment versus tail boom position. Wings locked at 45°, wing hinge angle of $(\phi_{\mathrm{H}}, \theta_{\mathrm{H}}) = (-40°, 40°)$.

Figure B.1 shows the lift, drag and moment plots for the model with the wings, midsection-wing and tail. The wings are locked at 0° and the wing hinge angle setting is $(\phi, \theta) = (-35°, 30°)$. There is overall good data correlation, post stall some difference is noted between the measured and calculated lift data.

Notice that, overall, the predicted results and the measured data agree very well, especially when the wings are set between 0° and 25°. When the wings are set at 45°, there are large three-dimensional aerodynamic effects on the configuration, and the correlations between the predictions and the measurements are not quite as good, especially at large tail boom angle settings. This is because of the high angles of attack the wings, mid-section, and tail are all experiencing along with the wing sweep angle and flow interference that is created at the wing joint. The results for the second set of wing hinge angles, $(\phi, \theta) = (-35°, 30°)$ are included in Appendix B. Overall the results for the $(\phi, \theta) = (-35°, 30°)$ wing hinge angle closely matched those of the $(\phi, \theta) = (-40°, 40°)$ wing hinge angle.

Chapter 6

Dynamic Deployment

6.1 Wing Hinge Friction Model

In the previous chapter the lift, drag and moment forces for static configurations where measured and compared to the predicted data. In this section, the predictions of the dynamic response of the free wings is considered. The development of a friction and damping model of the wing hinge proved critical to the successful prediction of the dynamic response. The wing hinge on the PRM is constructed with a pin and collar type joint that is lapped into position, but this still creates some friction.

Figure 6.1 shows the measured wing position for a wing drop test of the right wing. The model was created to try to accurately match the measured data from the wing drop tests, however it has proved difficult to do so with any kind of simple model.

The hinge friction was calculated by solving for the normal force acting on the wing hinge, and multiplying it by a coefficient of friction. The forces acting on the wing hinge can be calculated using the equation

$$F_H = [S_{HW}] \left\{ \begin{array}{c} T_{W_X} \\ 0 \\ N_{W_Z} \end{array} \right\} + [S_{HW}] W_{CG_W} \tag{6.1}$$

The normal force, F_N, is the z-component of F_H. The coefficient of friction, C_{FRIC}, depends upon the angular velocity about the wing hinge axis. If the angular velocity is zero, a static friction coefficient is used. If the angular velocity about the wing hinge axis is non-zero, a kinetic friction coefficient is used. In general, the kinetic friction coefficient is less than the static friction coefficient. The moment produced about the wing hinge by friction is

$$M_{\text{FRIC}} = F_N \; C_{\text{FRIC}} \; \text{sgn}(\dot{\psi}_{\text{H}}) \tag{6.2}$$

Many variables that are involved in calculating the wing hinge friction are too complex to model using this simple method [13]. The uncertainties in modeling include the proper representation of the shearing and normal forces, and bending moments as a function of the wing and tail positions. These forces and moments create areas of locally high shear and normal force within the wing hinge, and hence more friction is produced. While the friction was minimized using a graphite-based lubricant, it was not totally eliminated. Furthermore, the area in contact within

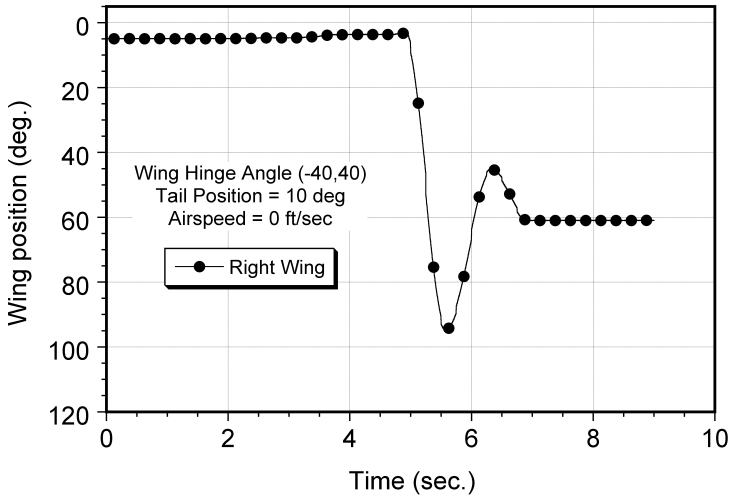

Figure 6.1: Measured wing position for a "drop test" of the right wing.

the wing hinge changes as a function of wing position about the hinge. Because of the geometry built into the wing hinge, the variation in these quantities is rather complicated. All of these uncertainties lead to friction effects that were observed during wind tunnel testing.

To examine the wing hinge damping, a series of calculations were conducted to simulate "drop tests." The wings were held in their almost fully-deployed condition with the wind off, and then dropped freely under the action of gravity alone, the tail was positioned and remained at 10°.

Figure 6.2 shows the effect of increasing the kinetic friction coefficient when the static friction coefficient is zero. It was found that as the kinetic friction coefficient is increased the time it takes for the wing to damp out to its final position is decreased as expected. Furthermore, the maximum amplitude of displacement of the wing position also decreases with increased kinetic friction coefficient.

Figure 6.3 shows the effect of increasing the static friction coefficient and

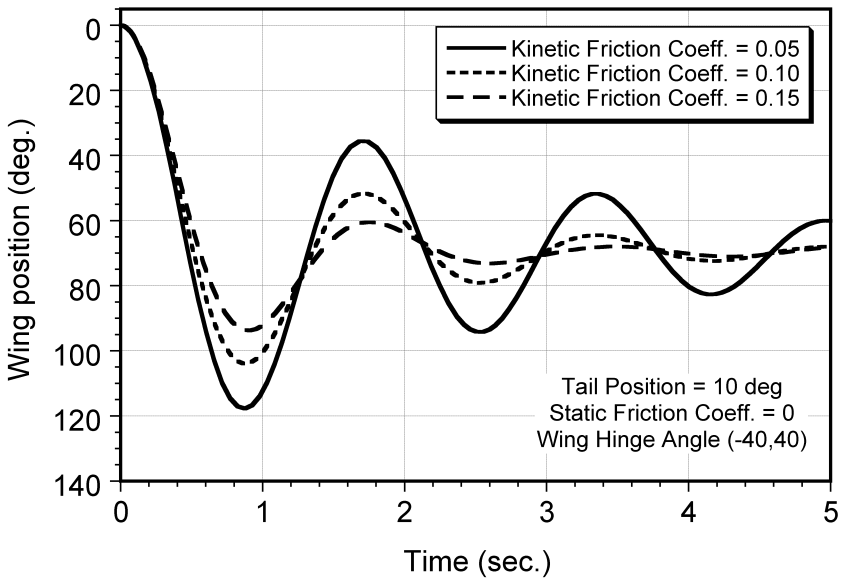

Figure 6.2: Wing drop test calculation with different kinetic friction coefficients.

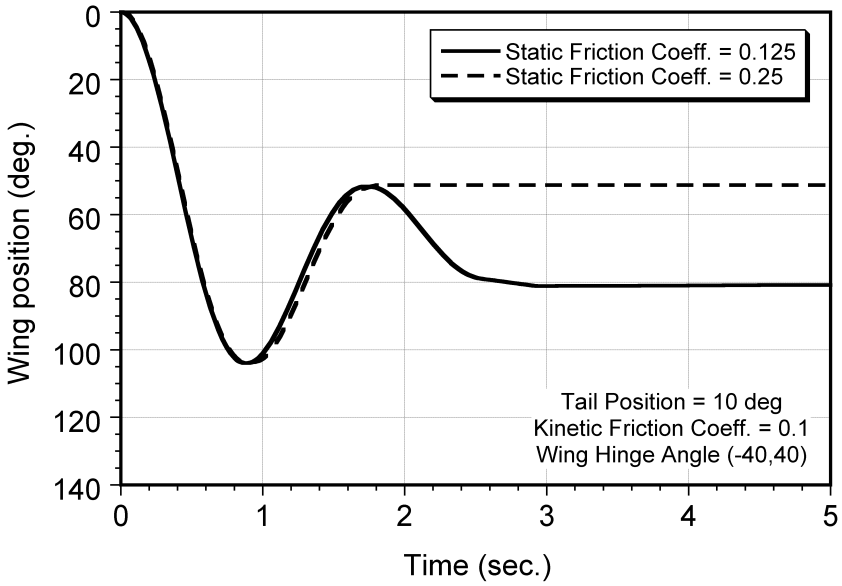

Figure 6.3: Wing drop damping calculation with different static friction coefficients.

holding the kinetic friction coefficient constant at a value of 0.10. When the static friction coefficient is 0.125 and 0.25, the final resting position of the wing is 81° and 51°, respectively. These calculations demonstrate how the final resting position of the wings under gravity alone are influenced by any static friction present in the wing hinge.

6.2 Dynamic Deployment Calculations

Figure 6.4 shows the deployment of the right wing in the wind tunnel versus the predictions made with the mathematical model. For the dynamic deployment experiments, the tail was not allowed to pivot freely, and its position was controlled using the servo actuator. To compare the dynamic results, the tail position at a particular time was set to match that measured with the wind tunnel model during the tests. The airspeed was set to the wind tunnel airspeed of 55 ft/sec. The initial

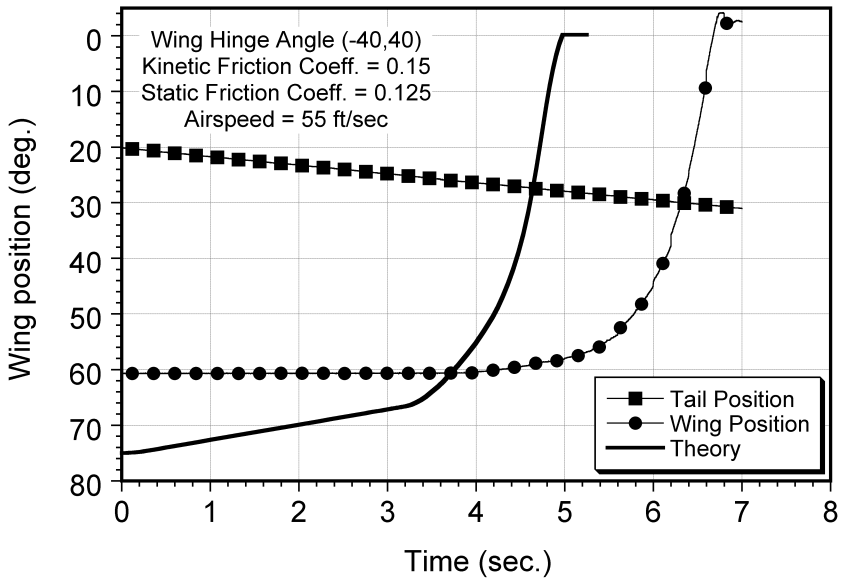

Figure 6.4: Predicted deployment of the wind tunnel model versus measurements. Kinetic friction coefficient = 0.35.

tail position was 20°, and it increased (moves downward) at a rate of 1.66°/sec. The static and kinetic damping coefficients used were 0.125 and 0.15, respectively.

It is apparent from the measured data that the wing stays at a relatively constant position of about 60° until a time of 4 seconds, when the wing begins to deploy. The wing stays at this constant position because of the static friction in the wing hinge. The predicted results shows that without static friction the wing would gradually deploy starting from time equal to zero. The initial starting position of the wing is determined by where the wing would settle if it was dropped from the deployed position with a tail position of 20° and without any wind velocity.

The predicted results show the initial starting position of the wing is 75°, however, the initial starting position of the measured wing position is 61°. The difference between the initial predicted and measured starting positions of the wing may be a result of static friction. Static friction can prevent the wing from freely

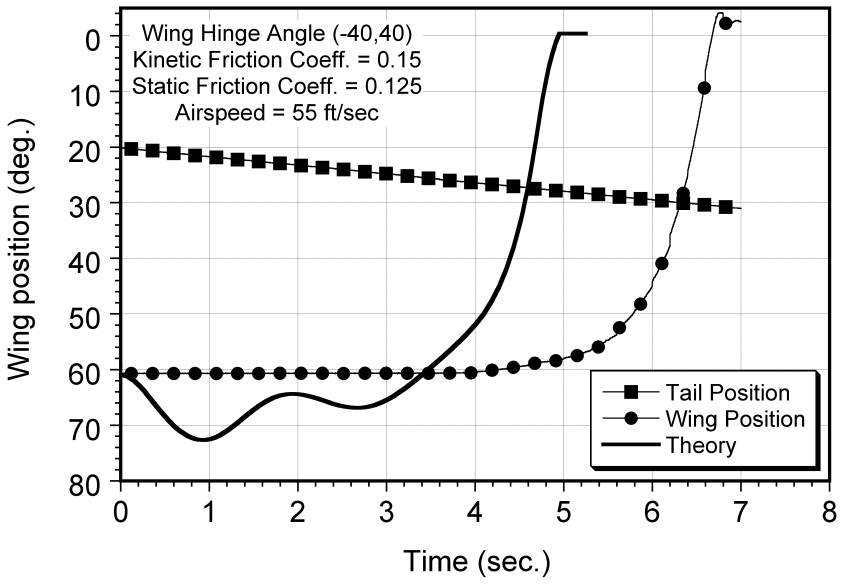

Figure 6.5: Predicted deployment of the wind tunnel model versus measurements. Kinetic friction coefficient = 0.35.

rotating down and settling at its intended resting position. As the tail is being lowered, the AoA on the wing increases to produce enough lift on the wing to overcome gravity and cause aerodynamic deployment. In this respect, both the measured and predicted results clearly show that the deployments are very similar. The measured complete deployment of the wing is 1.6 seconds longer then the predicted result, and this difference is probably associated with the effects of hinge friction.

Figure 6.5 shows the predicted and measured wing deployment for the right wing if the starting position of the wing in the mathematical model is matched to the initial position in the measured data (61°). It is apparent that the wing appears to drop at first to its intended initial starting position, and then follows a very similar deployment to that shown previously.

6.3 Oscillatory Behavior

Occasionally, the wings did not lock into place or they bounced back off the magnetic catches. If the tail continued to lower down past the deployment position while this occurred, an oscillatory type wing motion behavior was observed. Under these conditions, the wings would drop back under the action of gravity because of sufficient aerodynamic force to keep them raised, but then would experience an increased aerodynamic force as they dropped down. The wing panels then experienced a form of limit cycle oscillation, periodically lifting themselves up and dropping back down.

Figure 6.6 shows a measured example of this oscillatory limit cycle behavior that can be encountered if the wings do not lock into position during deployment and the tail continues to be lowered. When this oscillatory behavior was encountered in the wind tunnel, it was quickly eliminated by raising the tail, as shown here.

It was also possible to predict this behavior with the mathematical model, an example of which is shown in Fig. 6.7. This oscillatory behavior is shown to occur around 30° tail position for the both the predicted and measured results. The results show that the mathematical model is capable of predicting this limit cycle behavior, and hence identifying the combination of conditions where this behavior may occur in practice. To avoid this oscillatory behavior it was found imperative to start the wing deployment process by lowering the tail with a tail starting position of no greater than 20°.

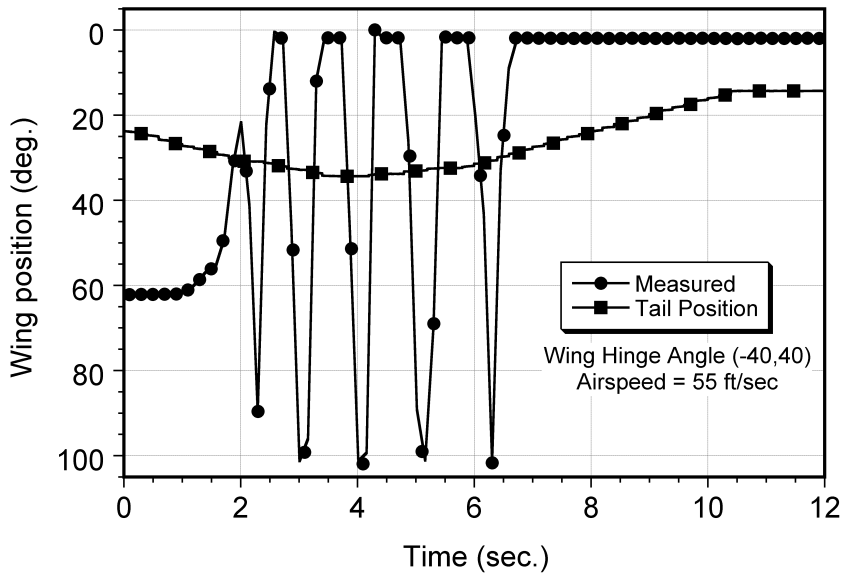

Figure 6.6: Example of oscillatory limit cycle behavior during wing deployment in wind tunnel, which is eliminated by raising the tail.

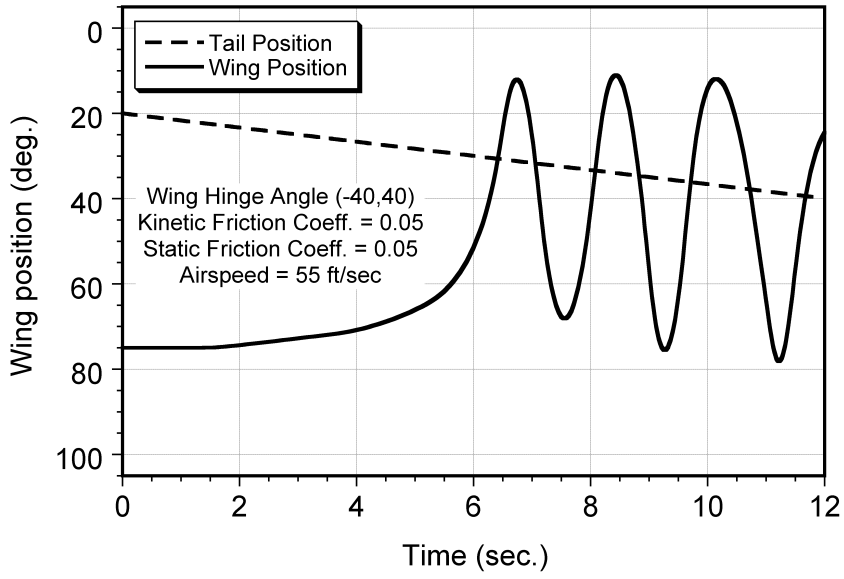

Figure 6.7: Example of the predicted limit cycle oscillatory behavior during wing deployment.

Chapter 7

Finite Element Method Analysis of Payload Support Structure

Previous chapters covered the development of a mathematical model to predict optimal wing hinge angle settings for wing deployment, the dynamic behavior of the wings and tail and also to calculate the lift, drag and moment forces on the MTR. Results from a wind tunnel study were then documented. This chapter discusses the development of a finite element method model (FEM) of the suspended payload support structure. The goal was to develop a model that is capable of predicting the deformation, stresses and moments within the payload support structure while under load. This model is to be incorporated into a full dynamic model to study stability related issues of the MTR while carrying a suspended payload at high flight speeds.

One particular mission of helicopters is to use them for carrying external suspended payloads. Helicopters are excellent for this task in that they are able to move heavy payloads to remote areas inaccessible to ground equipment. However, external payloads can modify the dynamic flight characteristics of the helicopter. The suspended payload is essentially a big pendulum, which is able to change the natural frequencies and mode shapes of the rigid body motion of the helicopter [15]. Suspended payloads are usually not aerodynamically shaped bodies, hence they are subject to large amplitude motions or even dynamic instabilities from unsteady

aerodynamic forces. The aerodynamic forcing on the suspended payload unit can make it unstable at certain flight conditions which can make the entire helicopter unstable and compromise the safety of flight.

Poli and Cromack [16] studied the stability of the helicopter in forward flight carrying rectangular and cylindrical payload units. They found that using long cables, high speeds and low payload weights can increase the stability of the load. Cliff and Bailey [17] also studied the stability of suspended payloads, they found out lower payloads weights did improve stability however longer cables would decrease stability. The contradiction in cable length between these two studies may be due to the differences in the aerodynamics of the load used. The aerodynamics of the payload unit is very important in relation to stability. Overall, it can be noted that by lowering the drag on the payload unit stability is increased. Nagabhushan [18] looked at low speed stability of a single point suspended payload configuration. He concluded that cable length, attachment point of the cable, and load weight all affected stability as well. By adjusting these parameters some modes could to be stable and others unstable. The most state of art work has been done by Cicolani [19], in the use of computer simulation to understand the sling load dynamics and flight handling qualities of the UH-60 helicopter.

From a just a quick overview of previous research it can be shown that a great deal of research must go into being able to transport a 20 ton payload unit suspended beneath the MTR at flight speeds over 200 knots. In fact, this will be a remarkable feat for the MTR if accomplished in comparison to the current suspended payload capabilities of helicopters, which are no where near capable of carrying this much

weight at such speeds. From the previous research the amount of weight carried, dimensions of the payload support structure, and attachment points to the payload all need to be studied. The first step in ensuring that the MTR suspended payload unit is stable and safe for flight is the development of a finite element model (FEM) of the payload support structure.

A FEM model of the MTR's structural payload support system was developed to calculate the forces, bending moments and deformations within the payload support structure. This FEM model is designed to be incorporated into a full dynamic model of the MTR to analyze the dynamic behavior of the MTR during flight maneuvers with the payload unit attached. Torsional modes may be present within the structure creating unwanted oscillations that may lead to adverse flight characteristics.

A preliminary FEM model was used to analyze the forces, bending moments and deformations on the payload support structure carrying a load that will stress the vertical supports in tension. The model was composed of finite elements capable to model both the in-plane and out of plane bending, as well the axial and torsional displacements. The model was developed using a standard FEM approach such as found in [20]. Initial results show that significant bending moments are present not only in the top beam, but throughout the entire support structure.

7.1 FEM Model

The following simplifying assumptions have been made for the initial finite element model of the strut assembly:

1. The aircraft is hovering with zero roll angle.

2. The telescopic joints are not modeled.

3. Each portion of the struts is modeled as a Bernoulli–Euler beam, and cross-sectional warping is neglected.

4. In-plane bending, out-of-plane bending, axial, and torsional displacements are each decoupled from the others.

The beam finite element used to model the frame is shown in Fig. 7.1. Note that the nodal degrees of freedom at each node are indicated in a local elemental coordinate system.

The element used has a total of 3 nodes, 2 nodes located at each end and 1 node located in the middle of the element. The nodes located at the ends are used to model the in-plane and out-plane bending and also torsional and axial deformations. The node located in the middle is used just for axial and torsional deformations. For each element there are 4 degrees of freedom for in-plane bending, 4 for out-of-plane bending, 3 for torsion, and 3 for axial displacements, for a total of 14 degrees of freedom. The vector of element local nodal degrees of freedom for one element is

$$x_L = [v_L\ v_{XL}\ v_R\ v_{XR}\ w_L\ w_{XL}\ w_R\ w_{XR}\ u_L\ u_C\ u_R\ \phi_L\ \phi_C\ \phi_R\ ]^T \tag{7.1}$$

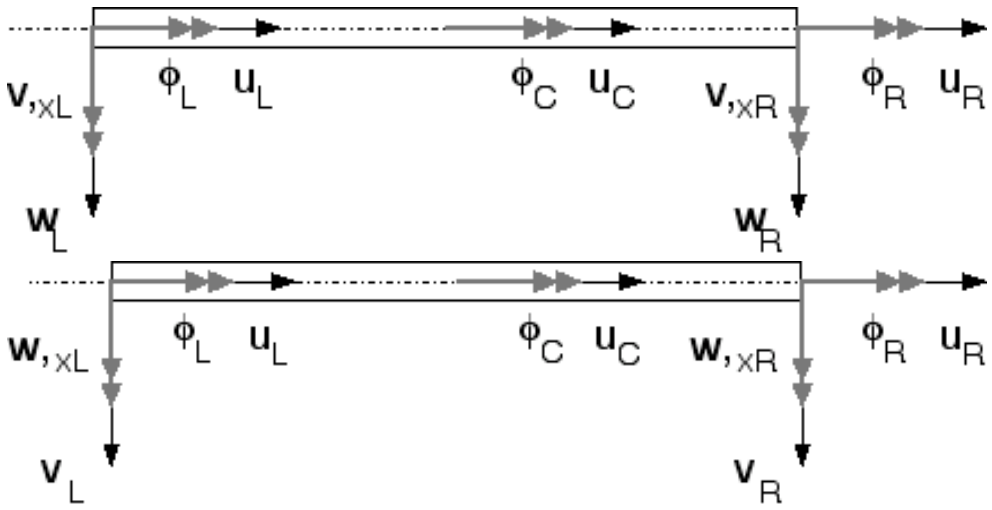

Figure 7.1: Beam finite element used to model the suspension frame; front view (top) and top view (bottom).

where V_L and V_R are the bending displacements out of the plane of the undeformed frame at the left and right ends of the element, and V_{XL} and V_{XR} are the corresponding slopes; W_L and W_R are the bending displacements in the plane of the undeformed frame, and W_{XR} and W_{XL} are the corresponding slopes; U_L, U_C, and U_R are the axial displacements at the left end, the mid-element, and the right end nodes of the element, respectively; and ϕ_L, ϕ_C, and ϕ_R are the torsional rotations at the left end, the mid-element, and the right end nodes of the element, respectively. It is important to note that vector x_L may consist of more than one elements local nodal degrees of freedom.

The element stiffness matrix $[K_L]$ for one element is given by

$$[K_L] = \begin{bmatrix} [K_{vv}] & 0 & 0 & 0 \\ 0 & [K_{ww}] & 0 & 0 \\ 0 & 0 & [K_{uu}] & 0 \\ 0 & 0 & 0 & [K_{\phi\phi}] \end{bmatrix} \tag{7.2}$$

It is important to note that the matrix $[K_L]$ shown above is just for one element, for the FEM analysis it is extended to include all elements in the structure.

The submatrix $[K_{vv}]$ is the element stiffness matrix for out-of-plane bending, and is given by

$$[K_{vv}] = \frac{EI_2}{\ell^3} \begin{bmatrix} 12 & 6\ell & -12 & 6\ell \\ 6\ell & 4\ell^2 & -6\ell & 2\ell^2 \\ -12 & -6\ell & 12 & -6\ell \\ 6\ell & 2\ell^2 & -6\ell & 4\ell^2 \end{bmatrix} \tag{7.3}$$

where EI_2 is the out-of-plane bending stiffness, and ℓ is the length of the finite element.

The submatrix $[K_{ww}]$ is the element stiffness matrix for in-plane bending, and is given by

$$[K_{ww}] = \frac{EI_3}{\ell^3} \begin{bmatrix} 12 & 6\ell & -12 & 6\ell \\ 6\ell & 4\ell^2 & -6\ell & 2\ell^2 \\ -12 & -6\ell & 12 & -6\ell \\ 6\ell & 2\ell^2 & -6\ell & 4\ell^2 \end{bmatrix} \tag{7.4}$$

where EI_3 is the in-plane bending stiffness.

The submatrix $[K_{uu}]$ is the element stiffness matrix for axial displacements, and is given by

$$[K_{uu}] = \frac{EA}{3\ell} \begin{bmatrix} 7 & -8 & 1 \\ -8 & 16 & -8 \\ 1 & -8 & 7 \end{bmatrix} \tag{7.5}$$

where EA is the axial stiffness.

Finally, the submatrix $[K_{\phi\phi}]$ is the element stiffness matrix for torsion, and is given by

$$[K_{\phi\phi}] = \frac{GJ}{3\ell} \begin{bmatrix} 7 & -8 & 1 \\ -8 & 16 & -8 \\ 1 & -8 & 7 \end{bmatrix} \tag{7.6}$$

where GJ is the torsional stiffness.

The finite element model used for the payload support structure is shown in Fig. 7.2. The model is composed of 10 finite elements and 20 nodes, the top torsion bar and the left and right vertical support structures are composed of three elements each and the bottom support structure one element. This is the simplest model possible to represent the payload support structure, more elements are required to achieve convergence of loads and stresses. The top torsion bar is shown to be supported at two locations corresponding to the arrangement in the actual aircraft. The left-and right-hand vertical support structures each have two roll hinges as shown. The roll hinges for the left and right vertical supports allow for free rotations in the roll degree of freedom. The final model, which results for are shown later, included a 28 element model.

The corresponding nodal degrees of freedom in the global (strut assembly) coordinate system are shown in Figs. 7.3 and 7.4 in a front view and a side view, respectively. The vector x_G of global degrees of freedom is given by

$$
\begin{aligned}
x_G \;=\; & [u_1\ u_3\ u_5\ u_7\ u_9\ u_{11}\ u_{13}\ u_{15}\ u_{17}\ u_{19}\ v_1\ v_2\ v_3\ v_4\ v_5\ v_6\ v_7\ v_8\ v_9\ v_{10}\ldots \\
& v_{11}\ v_{12}\ v_{13}\ v_{14}\ v_{15}\ v_{16}\ v_{17}\ v_{18}\ v_{19}\ v_{20}\ w_1\ w_3\ w_5\ w_7\ w_9\ w_{11}\ w_{13}\ldots \\
& w_{17}\ w_{19}\ \phi_1\ \phi_2\ \phi_3\ \phi_4\ \phi_{5A}\ \phi_{5B}\ \phi_6\ \phi_{7A}\ \phi_{7B}\ \phi_8\ \phi_9\ \phi_{10}\ \phi_{11}\ \phi_{12}\ \phi_{13A}\ \ldots \\
& \phi_{13B}\ \phi_{14}\ \phi_{15A}\ \phi_{15B}\ \phi_{16}\ \phi_{17}\ \phi_{18}\ \phi_{19}\ \phi_{20}\ \theta_1\ \theta_3\ \theta_5\ \theta_7\ \theta_9\ \theta_{11}\ \theta_{13}\ \theta_{15}\ \theta_{17}\ \ldots \\
& \theta_{19}\ \psi_1\ \psi_3\ \psi_5\ \psi_7\ \psi_9\ \psi_{11}\ \psi_{13}\ \psi_{15}\ \psi_{17}\ \psi_{19}]^T
\end{aligned} \tag{7.7}
$$

There are a total of 84 degrees of freedom. Note that at nodes 5, 7, 13, and 15, the rotational degree of freedom ϕ has two values, one for each side of the roll hinge.

The suspended load is modeled using two lumped masses located at the lower corners of the payload support structure at nodes 9 and 11. If there is zero roll angle, the problem is symmetric and only one half (left or right) of the frame needs to be modeled. The entire frame has been been modeled however, to be able to be used in non-zero roll angle conditions.

The transformation matrix T_{LG}, shown below, is used to transform the vector of global nodal degrees of freedom to the local nodal degrees of freedom coordinate system, i.e.,

$$X_L = [T_{LG}]X_G \tag{7.8}$$

A global stiffness matrix can then be defined as

$$[K_G] = [T_{LG}]^T K_L [T_{LG}] \tag{7.9}$$

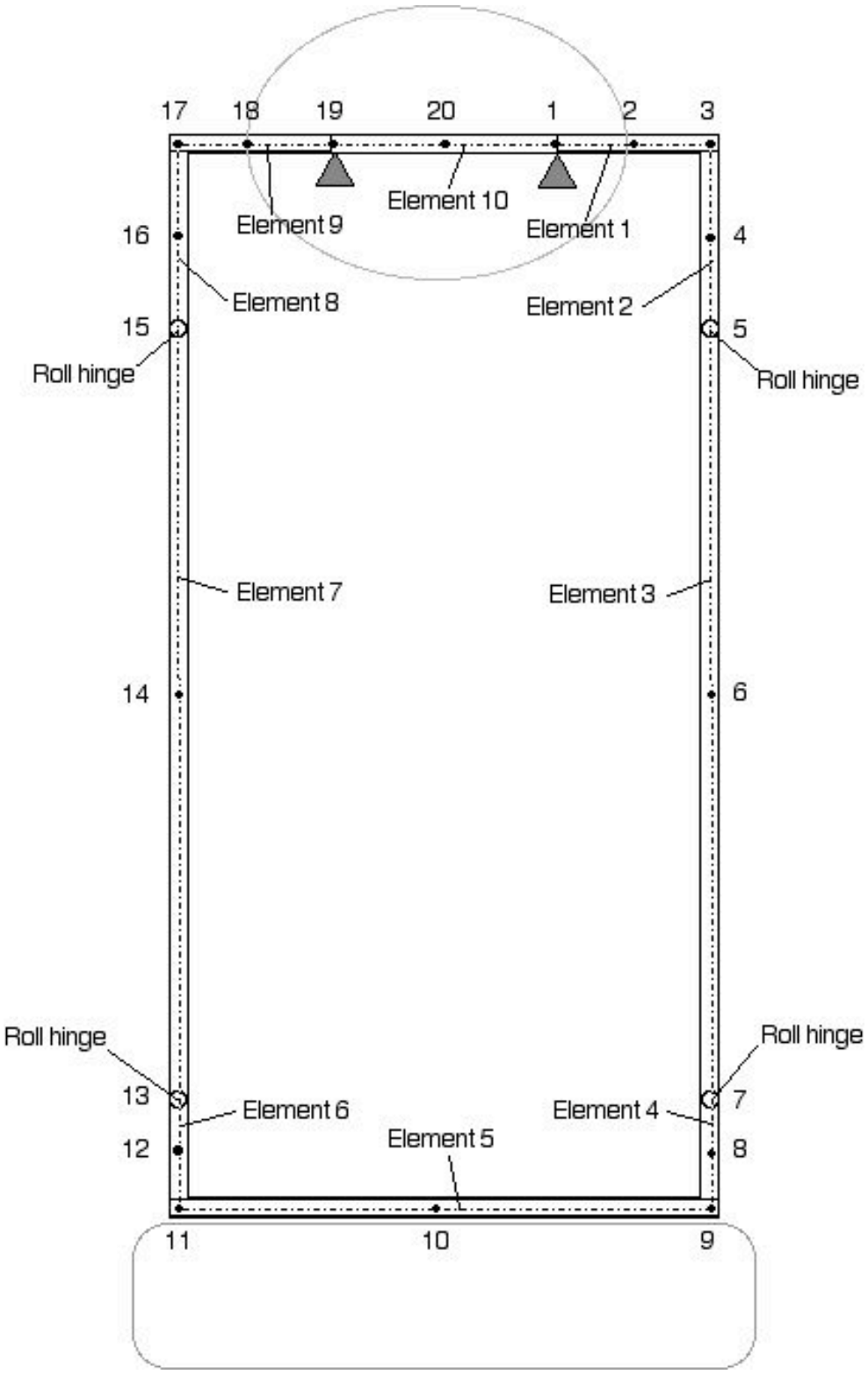

Figure 7.2: Basic finite element model of the strut assembly.

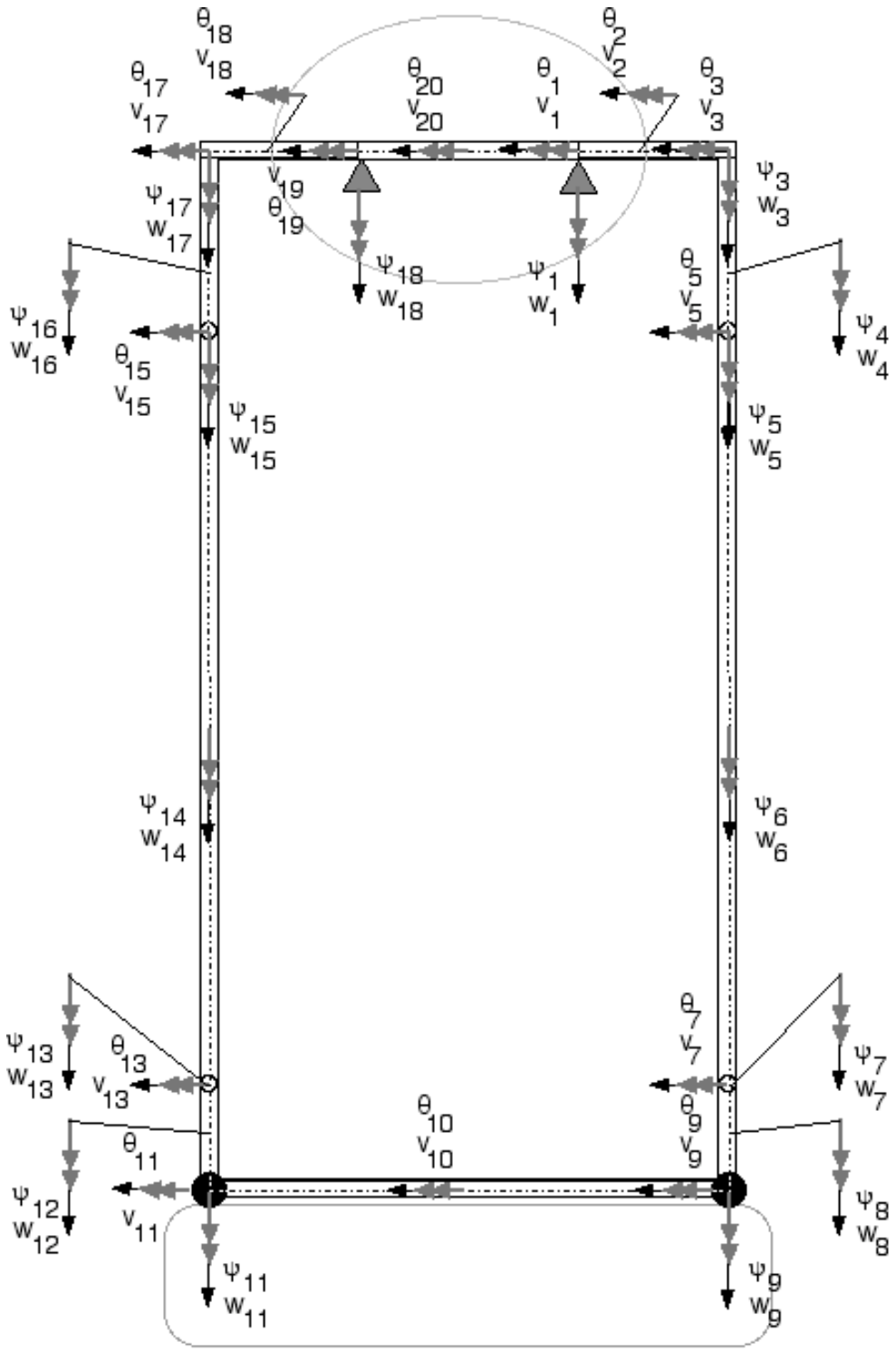

Figure 7.3: Global nodal degrees of freedom, front view.

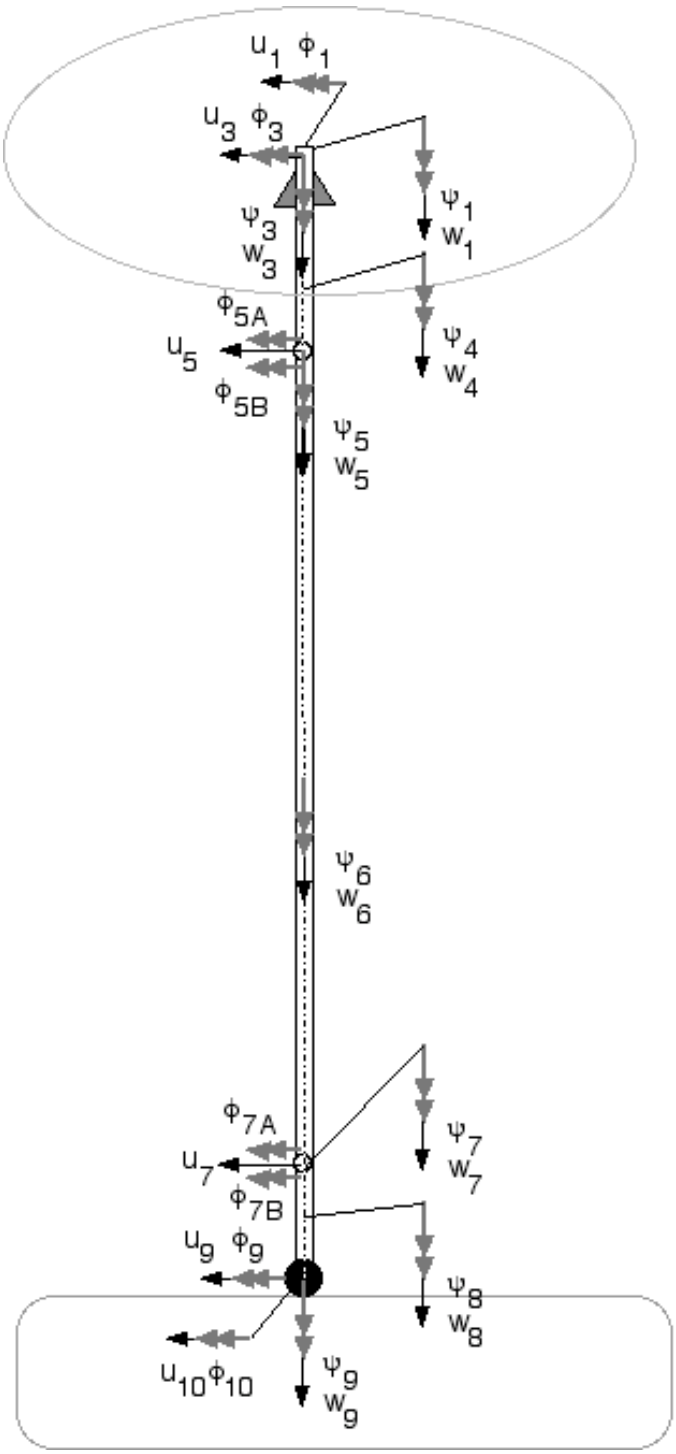

Figure 7.4: Global nodal degrees of freedom, side view (only the degrees of freedom of the right half of the assembly are shown).

To enforce constraints that are acting on the model, the particular row and column corresponding to that nodal degree of freedom was deleted. For instance, in the model the payload support structure is attached to the aircraft at nodes 1 and 19 and this inhibits any deformation in the plane and out plane bending directions at these nodes. Hence, the corresponding row and column that pertain to the in plane bending and out of plane bending displacements at nodes 1 and 19 are deleted from the global stiffness matrix. To ensure that no rigid bodies modes are present, torsional springs have been added at the roll joints. These springs are added by placing torsional spring constants k, and $-k$ at the corresponding ϕ_A and ϕ_B locations, respectively.

The global force vector, F_G, defines the force or moment that can be acting at each nodal degree of freedom in the global coordinate system. A moment in the global force vector represents any of the nodal degrees of freedom corresponding to angular displacements. A force corresponds to any nodal degree of freedoms that has a linear displacement. Using a LU decomposition method the global coordinate vector, X_G, can be solved for using

$$F_G = [K_G]X_G \tag{7.10}$$

The displacements, slopes, moments and forces at any point in a element were solved for using Hermite interpolation polynomials. Cubic interpolation polynomials were used for bending, and quadratic interpolation polynomials were used for torsion and axial displacements. The Hermite polynomials used are included in Appendix

C.

7.2 FEM Results

The model used in these results is a 28 element model. The left and right vertical supports contained 12 elements, each element being 12 inches in length. The top element has 3 elements each 12 inches in length and the bottom element 1 element, 36 inches in length. Therefore, there are a total of 228 nodal degrees of freedom. These dimensions represented a scaled version of the payload support structure to be used as an initial starting point for the analysis.

The suspended load was simulated by applying two 10,000 lb forces, in the vertical direction, onto the right and left ends of the lower horizontal bar. The structure was assumed to be constructed out of a Graphite Epoxy (IM-613501-6) composite. The modulus of rigidity and the modulus of elasticity depend on number of plies, ply orientation, and matrix/fiber ratios. Values of $1{\cdot}10^6$ $\mathrm{lb\,in^{-2}}$ and $34.1 \cdot 10^6 \mathrm{lb\,in^{-2}}$, respectively, were chosen for this material. The structure is composed of tubular hollow ellipse elements of constant cross section throughout the entire frame. The area moments of inertia about the local x- and y-axes were 0.118 in^4 and 0.6483 in^4, respectively. The cross sectional area was 0.28 in^2 and the polar moment of inertia was 0.3478 in^4.

The results are presented for each portion of the strut assembly. Figures 7.5 and 7.6 show the bending displacement and slope for the top beam of the payload support structure. The top beam is assumed to be supported by the fuselage of the

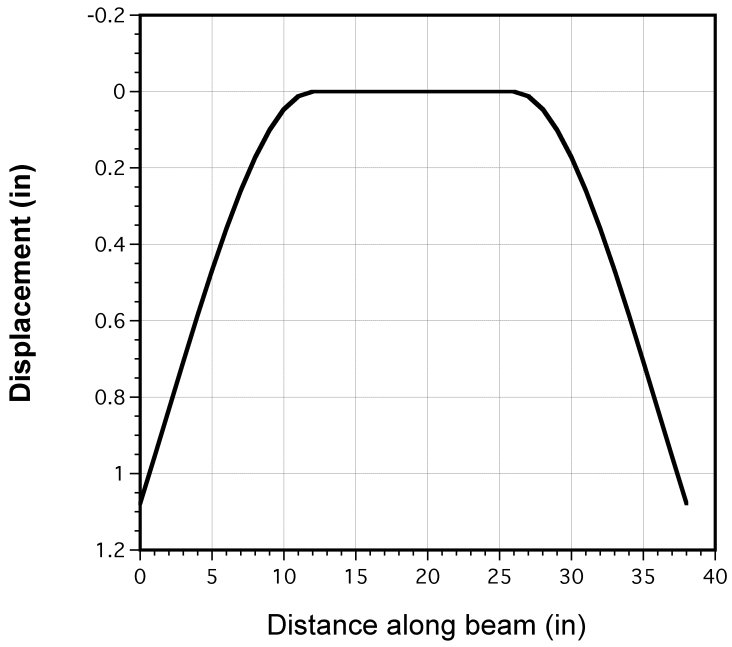

Figure 7.5: In-plane bending displacement for the top beam of the strut assembly.

aircraft with cantilever boundary conditions for in-plane and out-of-plane bending. The ends of the top beam are shown to deflect and bend downward, in-plane, 1.1 inches under the load. A non-zero slope is clearly shown at both ends, as a result, a bending moment is transmitted down, to the vertical portion of the struts.

The in-plane bending moment for the top beam is shown in Fig. 7.7. The largest moments are shown to occur at where the top beam is attached and supported to the fuselage of the aircraft. As expected excellent symmetry between both ends of the top beam is shown to exist. There is no displacement, slope or bending moment in the middle section of the beam, between the attachment points to the fuselage. No out-of-plane displacements were noted.

The axial displacement and force for the top beam are shown in Figs. 7.8 and 7.9 respectively. It is apparent that the top beam is in tension, and that both

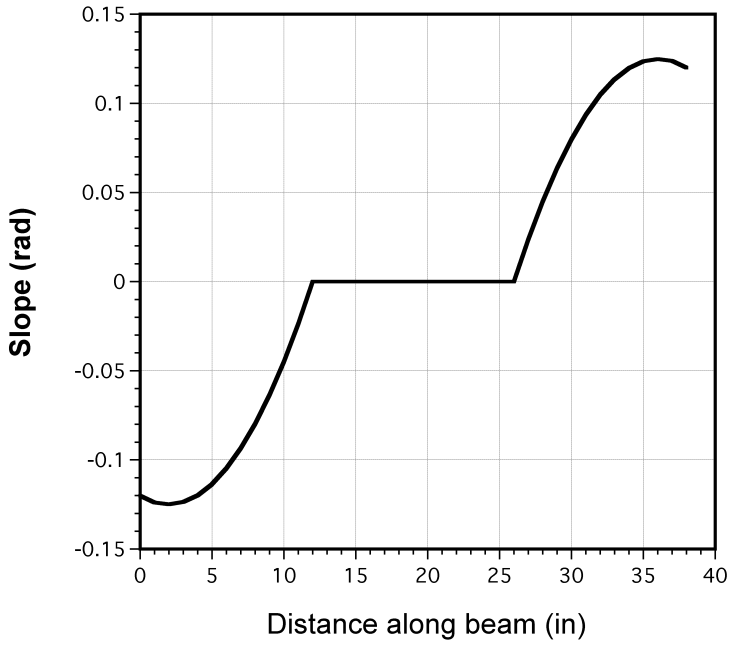

Figure 7.6: In-plane bending slope for the top beam of the strut assembly.

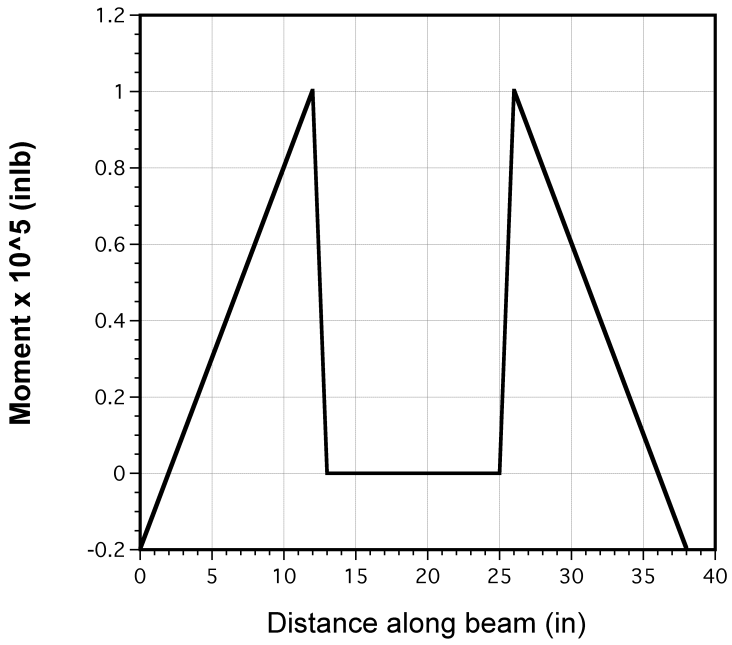

Figure 7.7: In-plane bending moment for the top beam of the strut assembly.

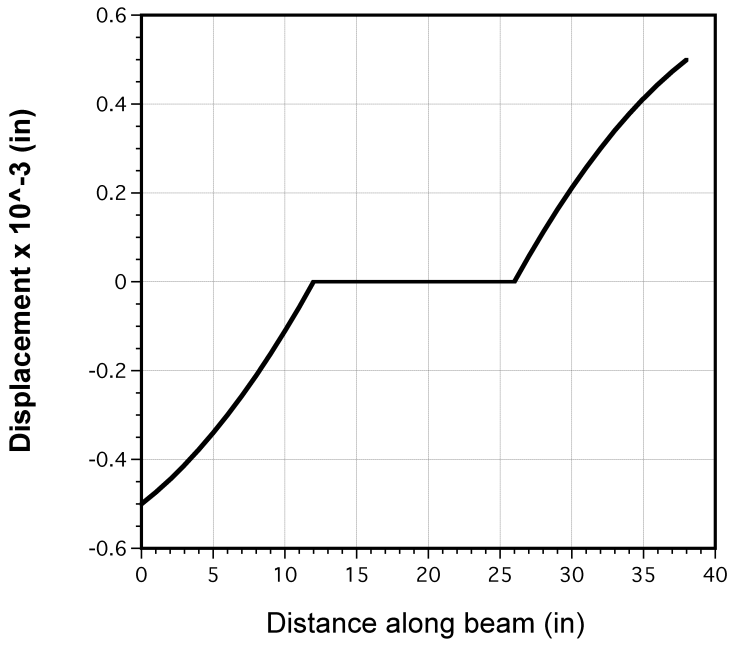

Figure 7.8: Axial displacement for the top beam of the strut assembly.

ends have been displaced 0.5 inches axially outward.

Figure 7.10 shows the bending displacements in the plane of the strut assembly for the right strut (top plot) and the left strut (bottom plot). Note that the x-axis of the left strut's bending displacement, slope and moment plots have been reversed to show the symmetry that exists between the left and right vertical beams. The figure clearly shows the effect of bending in the top portion of the struts (left portion of each plot). The displacements in the middle portion of the struts, between the roll hinges, and in the bottom portion, below the lower roll hinge, should be linear or nearly linear. The curvature visible in these portions is caused by artificial springs added at the hinges to remove the singularities in the stiffness matrix associated with rigid body modes.

Figure 7.12 shows the corresponding bending moments for the right strut (top

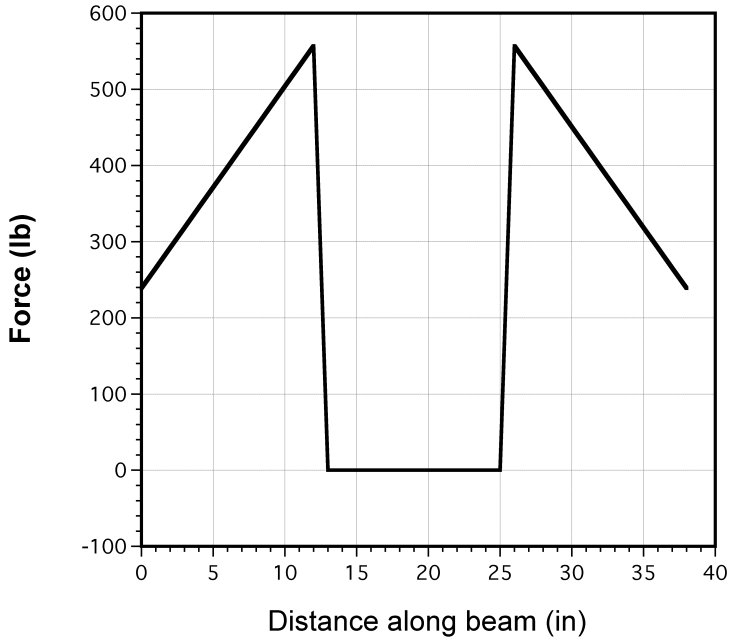

Figure 7.9: Axial force for the top beam of the strut assembly.

plot) and the left strut (bottom plot). The highest bending moments are at the top of the struts (left portion of each plot). Discontinuities are shown in the moment plots at where the roll hinges are located, these discontinuities are a result of the springs that have been added at the joints. Softer spring were tried, but they could not eliminate the singularities in the matrices. Modeling of the vertical struts without roll hinges eliminated the discontinuities all-together.

Figure 7.13 shows the axial displacements in the right and left vertical struts. The axial displacements are shown to increase linearly from the top of the vertical strut, where it joins the top bar, to the bottom of the vertical strut where it meets the bottom bar. The maximum axial displacement was 1.23 in.

Figure 7.14 shows the axial forces in the right and left vertical struts. As expected, the axial forces in the vertical struts are constant throughout the struts,

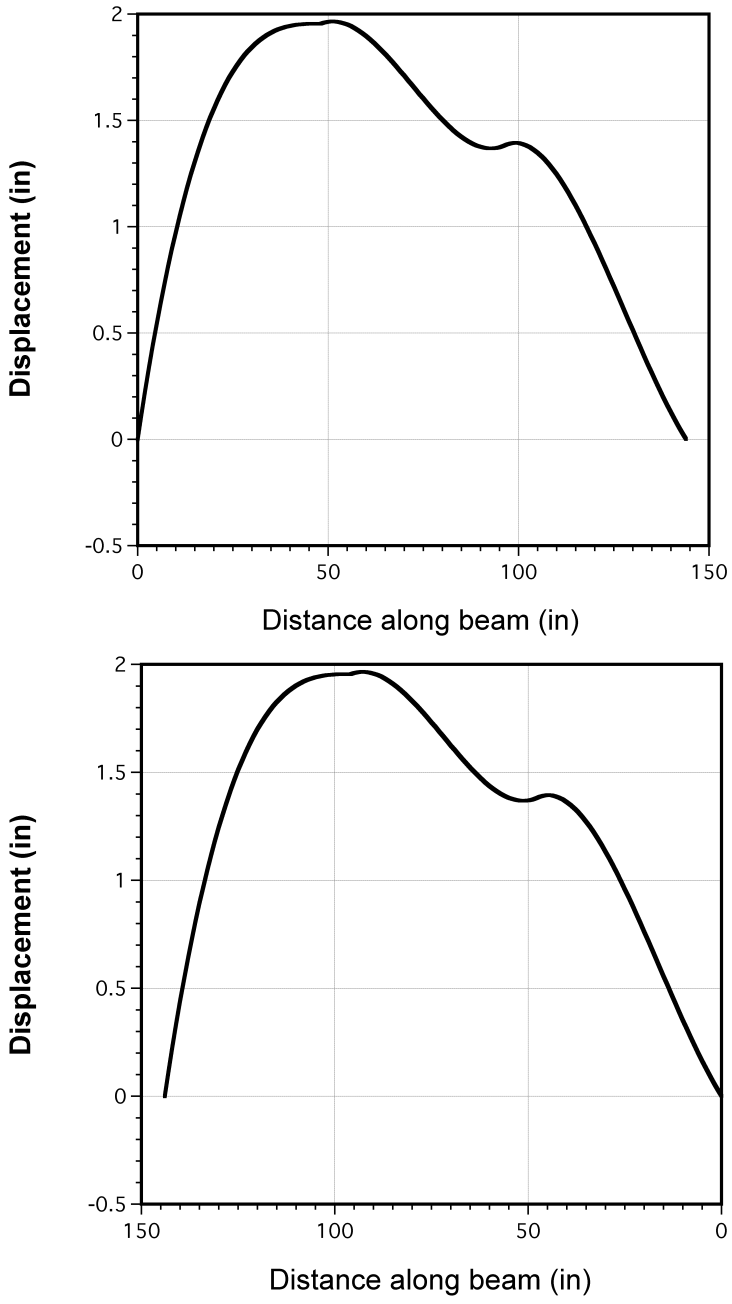

Figure 7.10: Bending displacements in the left and right beams.

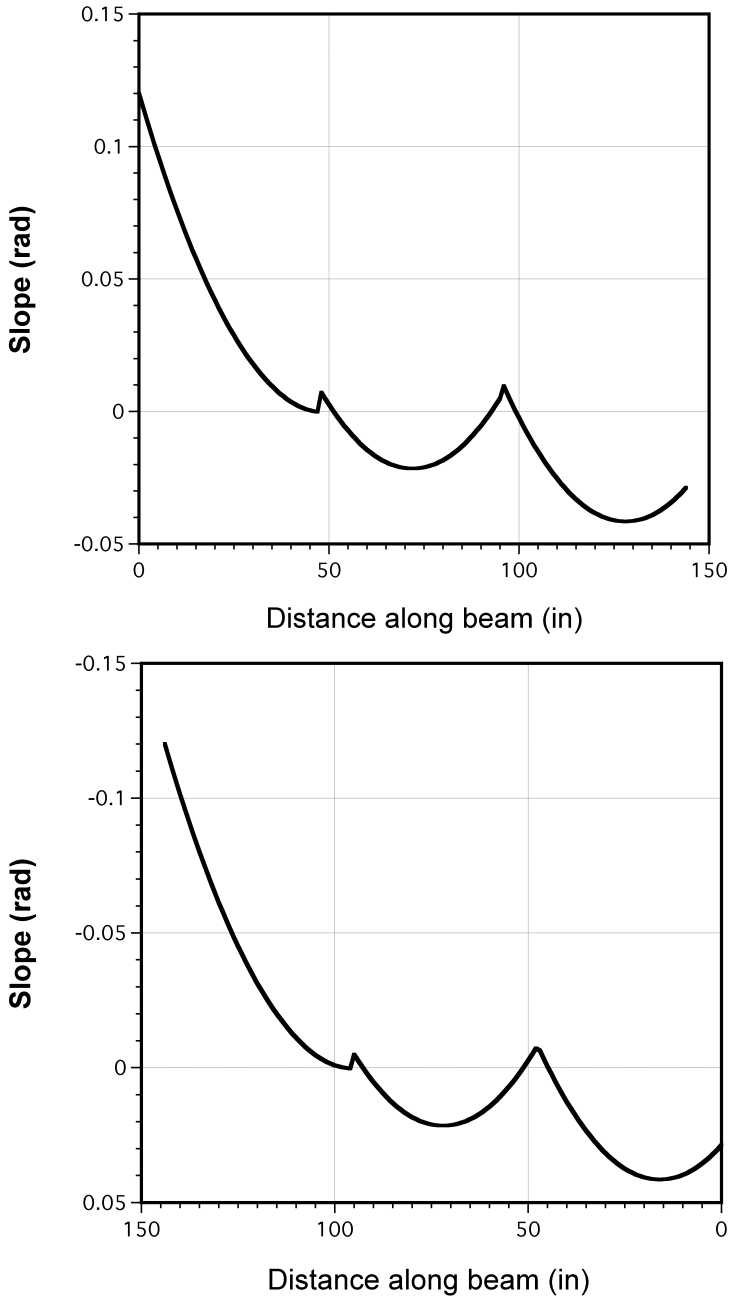

Figure 7.11: Slopes of the left and right beams.

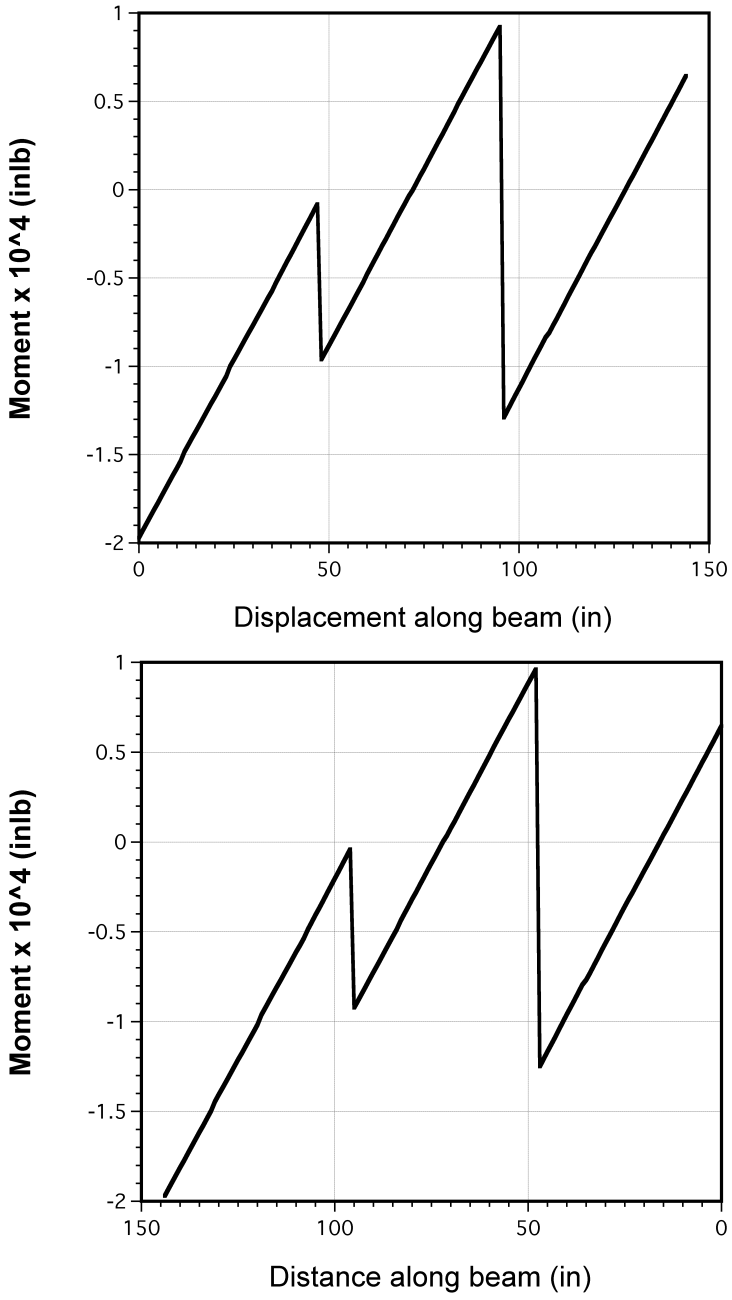

Figure 7.12: Bending moments in the right and left vertical struts.

and the axial force in each strut is equal to one of the two applied loads of 10,000 lb.

Figures 7.15, 7.16 and 7.17 show the in-plane bending displacement, slope and moment for the bottom beam, respectively. These figures show that the beam is subject to a constant bending moment, and hence a quadratic bending displacement occurs.

Figures 7.18 and 7.19 show the axial displacement and force for the bottom beam. The axial displacement is shown to be linear and a maximum displacement of 0.8 in. occurs at both ends of the bottom beam. The axial force is shown to be constant.

Overall, this FEM model is the first step in creating a comprehensive model to be eventually incorporated into a full dynamic model of the MTR. The next step in this model would be the calculation of the mass matrix to be used in calculating the time dependent response of the payload support structure to external forcing.

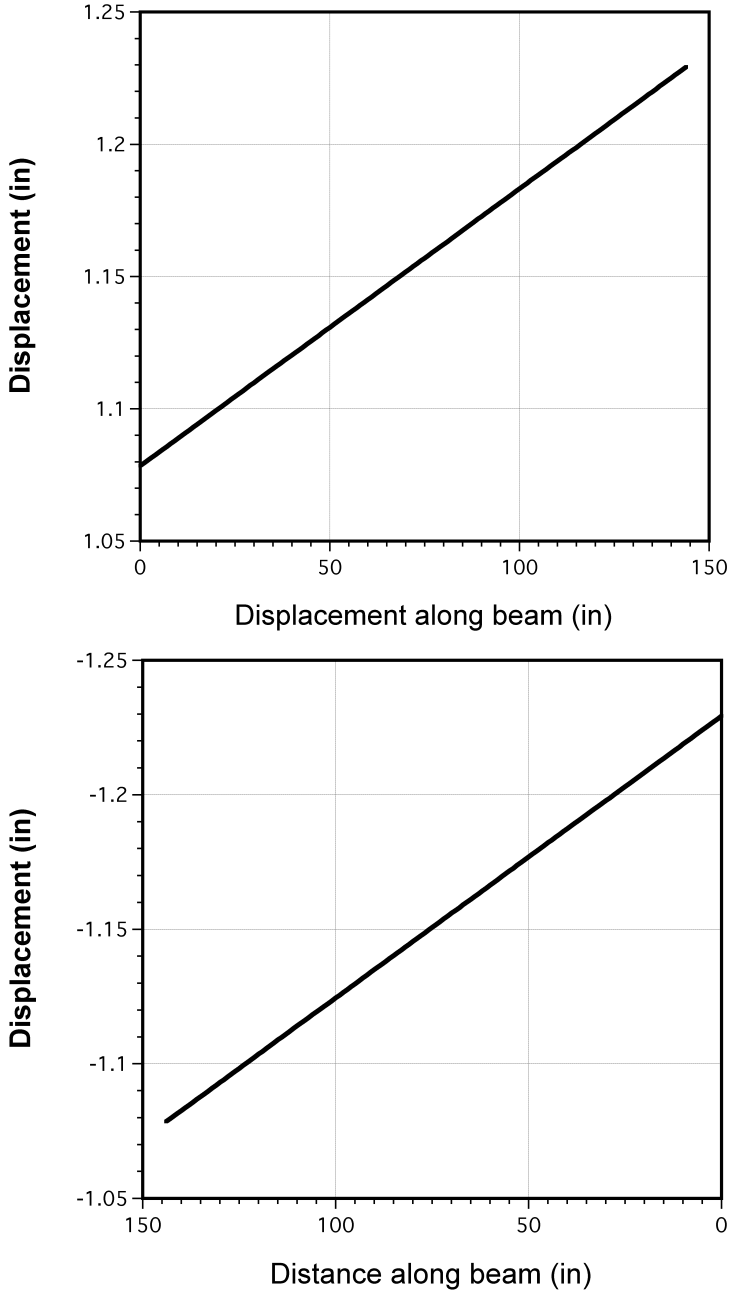

Figure 7.13: Axial displacements in the right (top plot) and left (bottom plot) vertical struts.

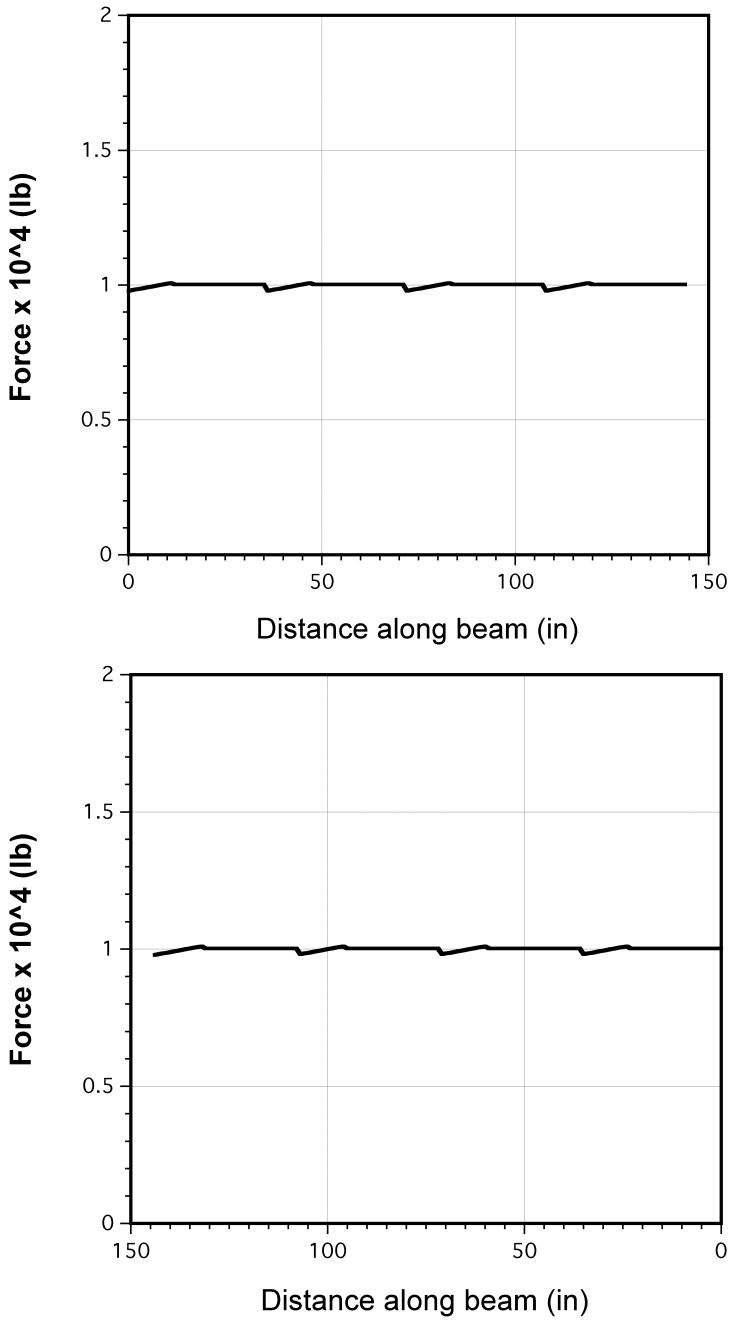

Figure 7.14: Axial forces in the right (top plot) and left (bottom plot) vertical struts.

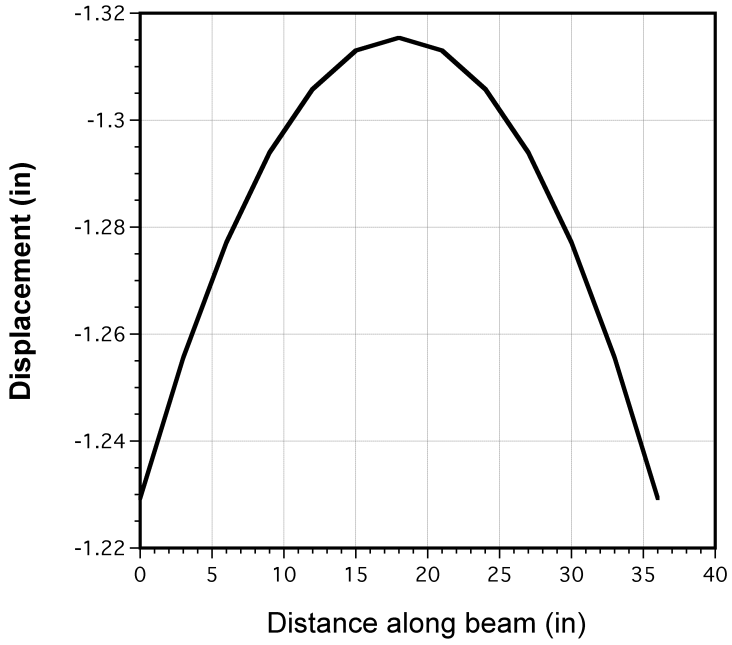

Figure 7.15: In-plane bending displacement for the bottom beam.

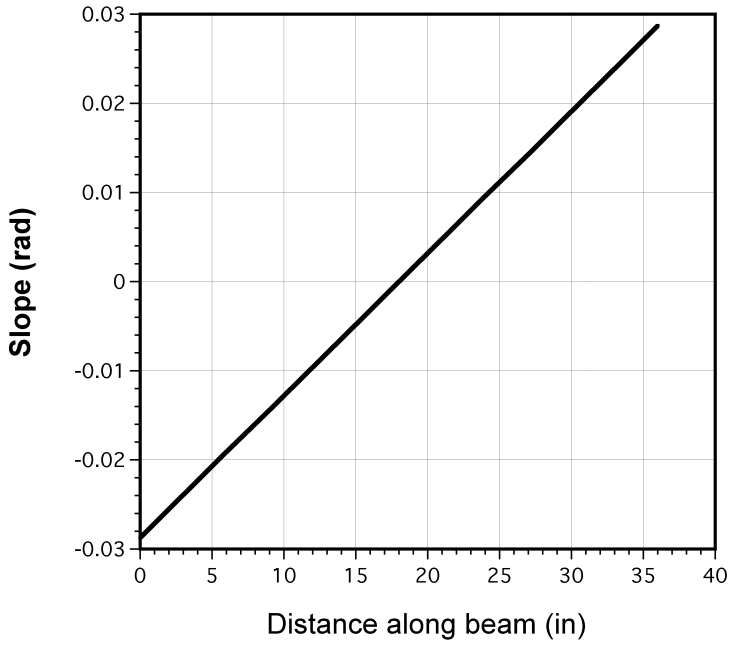

Figure 7.16: In-plane bending slope for the bottom beam.

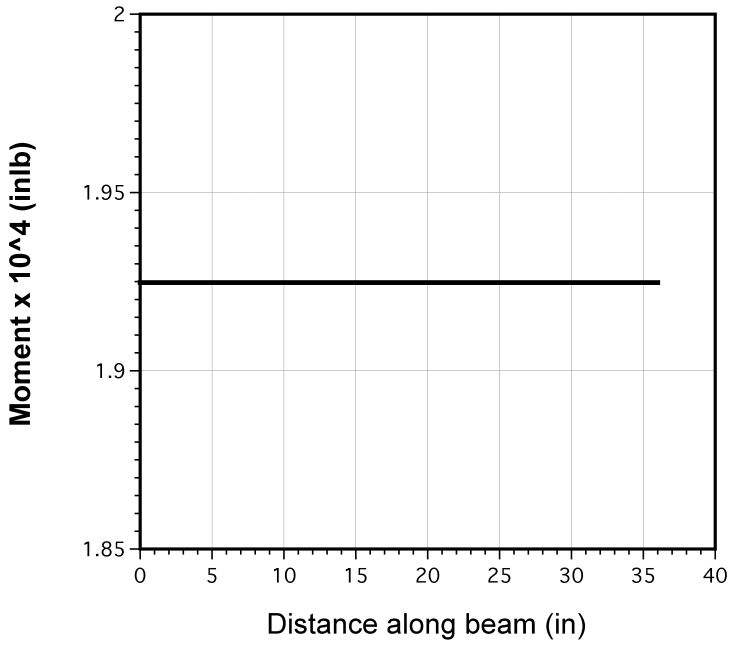

Figure 7.17: In-plane bending moment for the bottom beam.

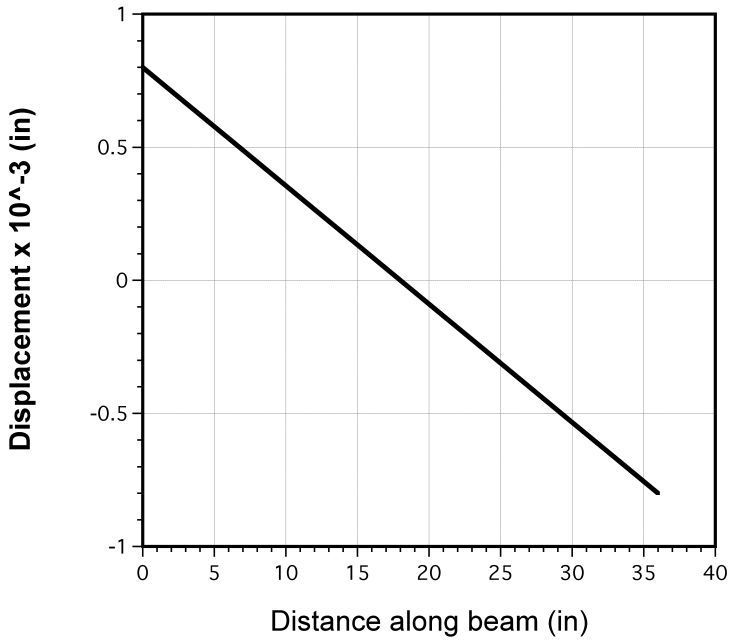

Figure 7.18: Axial displacement for the bottom beam.

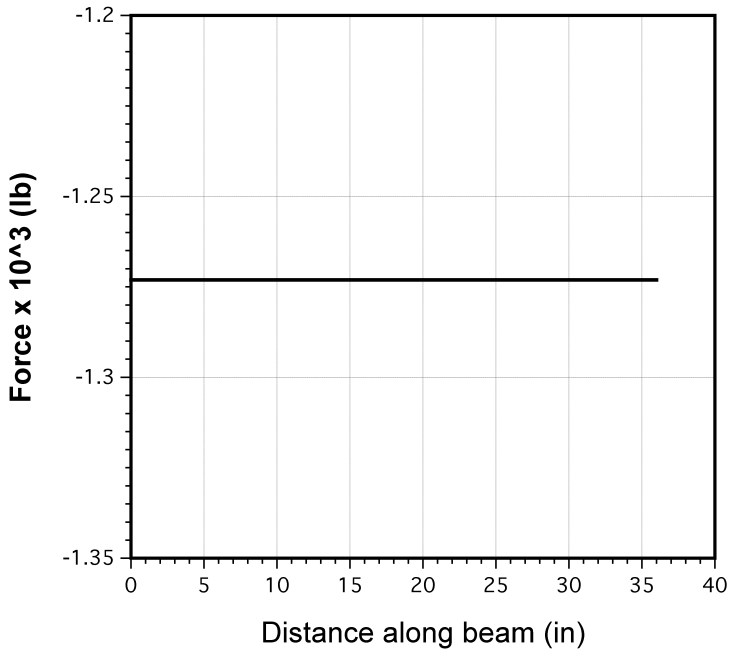

Figure 7.19: Axial force for the bottom beam.

Chapter 8

Conclusions and Recommendations for Future Work

A mathematical model was developed to calculate the static forces and dynamic behavior of the wings and tail of the MTR. Using the mathematical model an equilibrium analysis was conducted to predict the wing hinge angle geometry to produce aerodynamically deployable wings. A wind tunnel test was then conducted on a sub-scale model, which demonstrated successful wing deployment using the "most likely to succeed" wing hinge angle geometry predicted from the equilibrium analysis.

The mathematical model was further refined and shown to predict the lift, drag and moment forces on the MTR's wing and tail configurations with good correlation to the wind tunnel data. The predicted dynamic behavior of the wings during deployment also showed good agreement with the measurements from the wind tunnel study. The mathematical model was further shown to be capable of predicting the oscillatory behavior of the wings that was observed at certain tail boom positions during wind tunnel testing. An FEM model was developed to predict the forces, bending moments and displacements within the payload support structure under load. This FEM model was developed using 28 finite elements, additional FEM studies in future must include adding more finite elements to reach a convergence on calculated forces, bending moments, and displacements.

The following specific conclusions have been drawn from the work reported in this thesis

1. The mathematical model allowed for the determination of wing hinge angle configurations for wing self-deployment. The selected hinge geometries resulted in successful and repeatable wing deployments demonstrated in the wind tunnel study.

2. A successful wind tunnel study was conducted to show aerodynamic wing deployment is achievable in a controlled manner without oscillatory or divergent behavior. Wing deployment was obtained at several different combinations of wing hinge angles, wind speed, and tailboom angles, suggesting that there would be a relatively wide deployment envelope on the actual aircraft.

3. The mathematical model successfully predicted the lift, drag and moment forces on the MTR configuration with good correlation to measured wind tunnel data. However, the correlation was found to be less acceptable at higher angles of attack, most likely because of significant spanwise flow and three-dimensional interference effects created at the wing hinge.

4. The predicted dynamic behavior of the wings during deployment agreed reasonably well with the wind tunnel data. A wing hinge friction model was developed and used to better model dynamic wing deployment. The oscillatory wing behavior encountered in the wind tunnel at certain tail boom positions can be predicted with the mathematical model, and can be used in further studies to help avoid this behavior.

5. The FEM analysis has shown to be a useful tool in predicting the forces, moments and displacements in the payload support structure. An initial study has shown that bending moments may be present throughout the entire structure while under load with the vertical supports struts in tension. Bending moments present in the top beam support strut, where the suspended payload structure is attached to the MTR, will have to be taken into consideration during design of the actual aircraft.

Future work may include using the mathematical model to analyze the deployment of the wings with the addition of the downwash from the rotor. A wind tunnel study could then be conducted with a coaxial rotor to evaluate the deployment of the wings in the downwash. The mathematical model may also be used to study wing deployment on a full scale MTR to find at what flight speeds and tail positions wing deployment can be achieved. In addition a control system could be developed to control the rate of deployment of the wings using ailerons. The FEM model will be incorporated into a dynamic model of the MTR to analyze the flight stability while carrying a suspended payload. A model of the unsteady aerodynamics on the payload unit will have to be developed to model any unsteady aerodynamic forces that may occur at high flight speeds as well.

Appendix A

Additional Equilibrium Plots

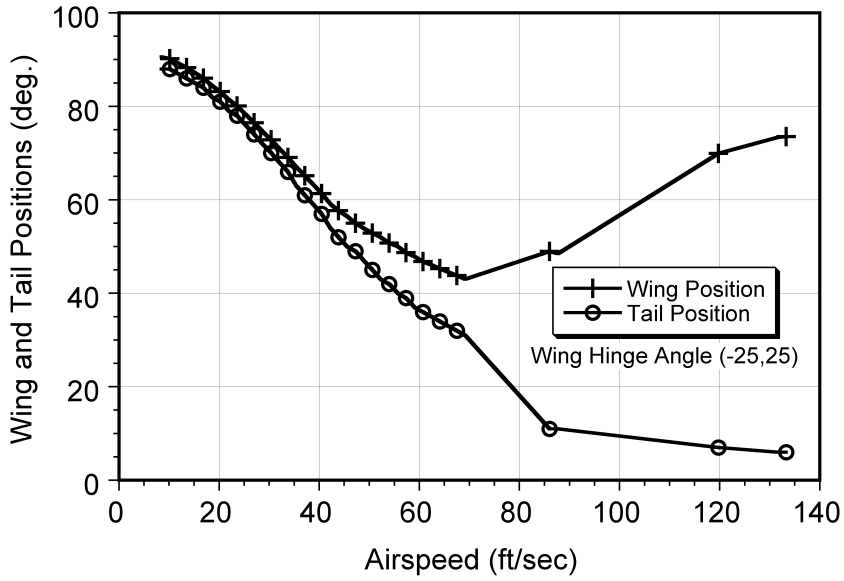

Figure A.1: Equilibrium positions of the wing and tail versus airspeed for wing hinge angle setting $(\phi_{\mathrm{H}}, \theta_{\mathrm{H}}) = (-25°, 25°)$.

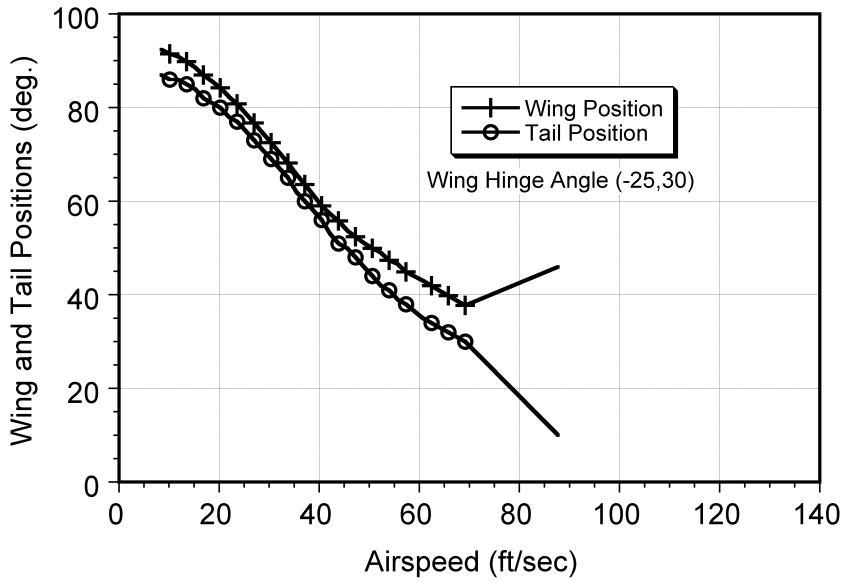

Figure A.2: Equilibrium positions of the wing and tail versus airspeed for wing hinge angle setting $(\phi_{\mathrm{H}}, \theta_{\mathrm{H}}) = (-25°, 30°)$.

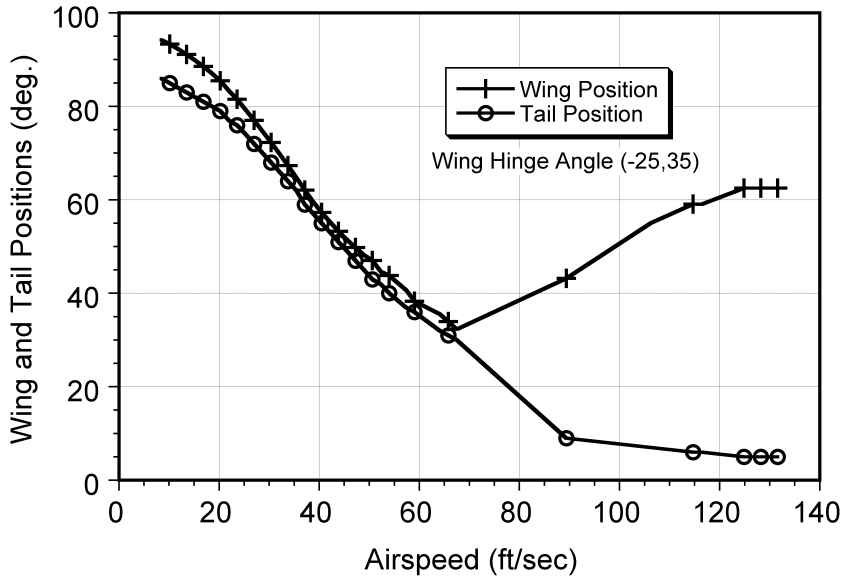

Figure A.3: Equilibrium positions of the wing and tail versus airspeed for wing hinge angle setting $(\phi_{\mathrm{H}}, \theta_{\mathrm{H}}) = (-25°, 35°)$.

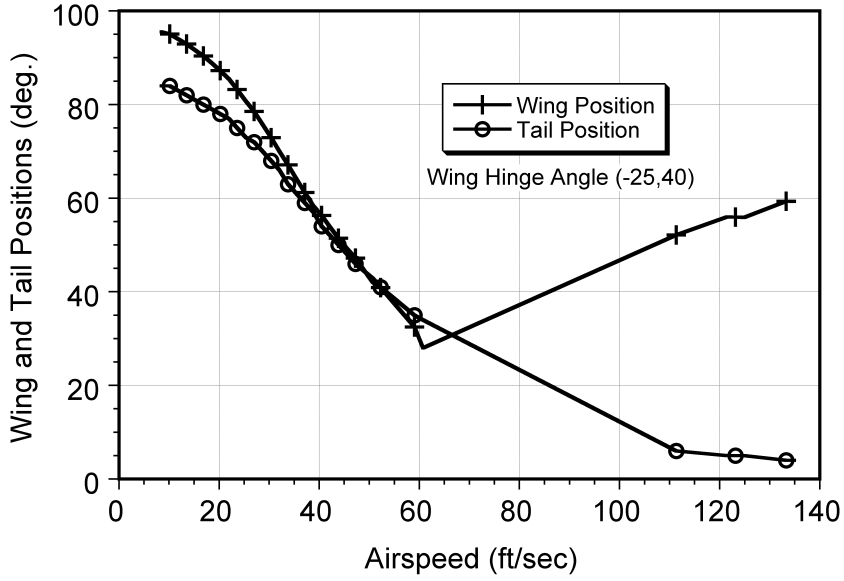

Figure A.4: Equilibrium positions of the wing and tail versus airspeed for wing hinge angle setting $(\phi_{\mathrm{H}}, \theta_{\mathrm{H}}) = (-25°, 40°)$.

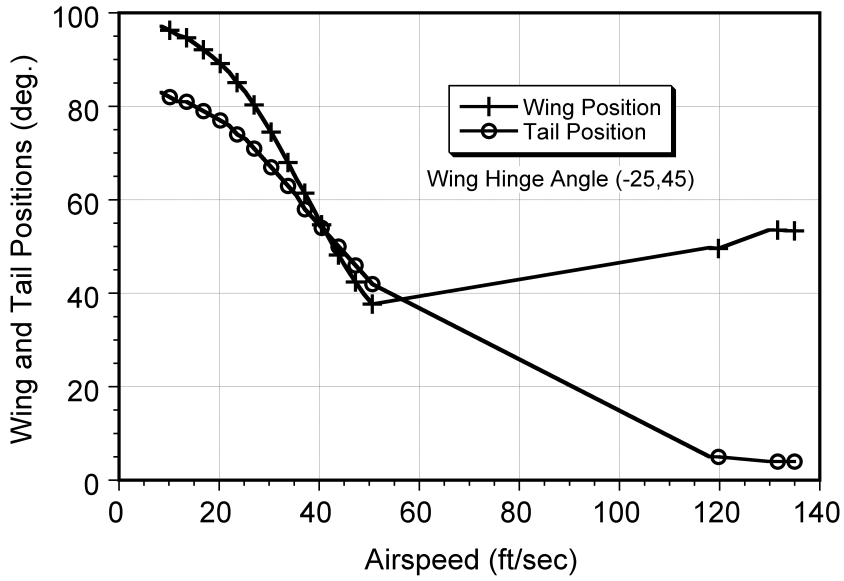

Figure A.5: Equilibrium positions of the wing and tail versus airspeed for wing hinge angle setting $(\phi_{\mathrm{H}}, \theta_{\mathrm{H}}) = (-25°, 45°)$.

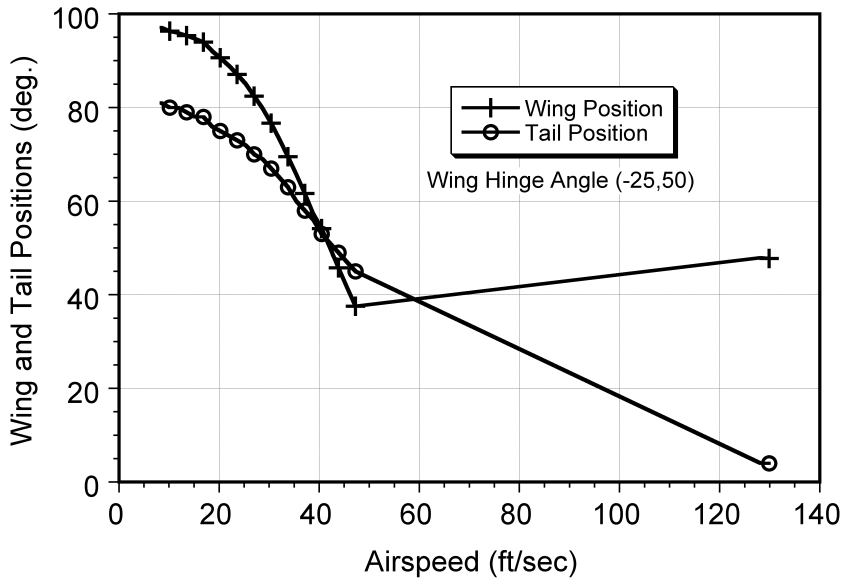

Figure A.6: Equilibrium positions of the wing and tail versus airspeed for wing hinge angle setting $(\phi_{\mathrm{H}}, \theta_{\mathrm{H}}) = (-25°, 50°)$.

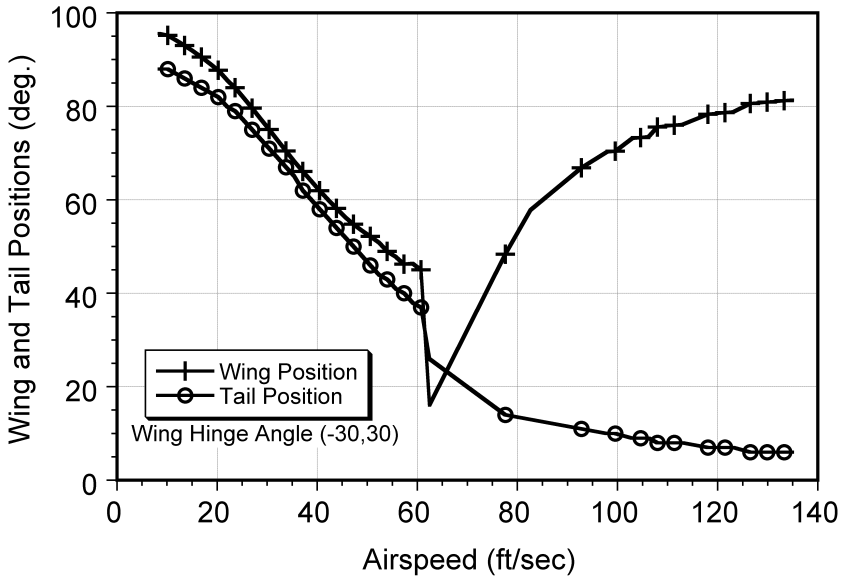

Figure A.7: Equilibrium positions of the wing and tail versus airspeed for wing hinge angle setting $(\phi_{\mathrm{H}}, \theta_{\mathrm{H}}) = (-30°, 30°)$.

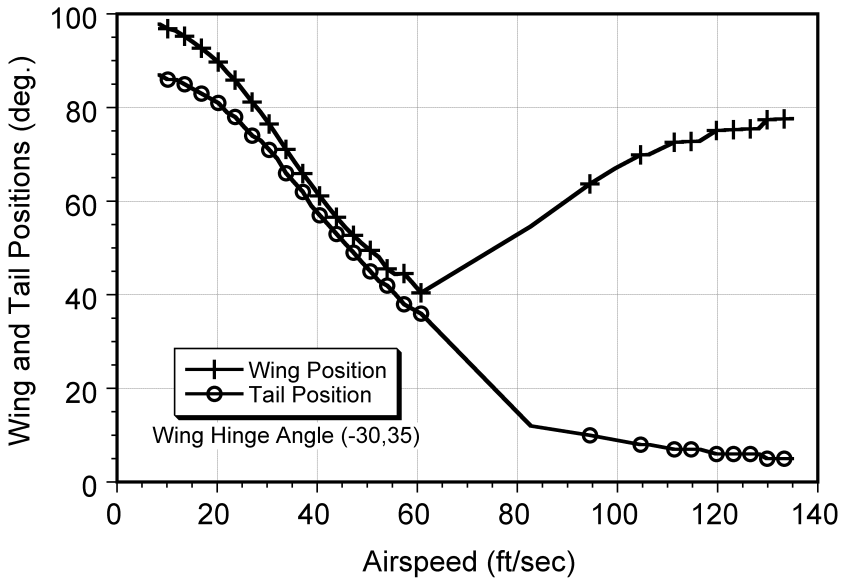

Figure A.8: Equilibrium positions of the wing and tail versus airspeed for wing hinge angle setting $(\phi_{\mathrm{H}}, \theta_{\mathrm{H}}) = (-30°, 35°)$.

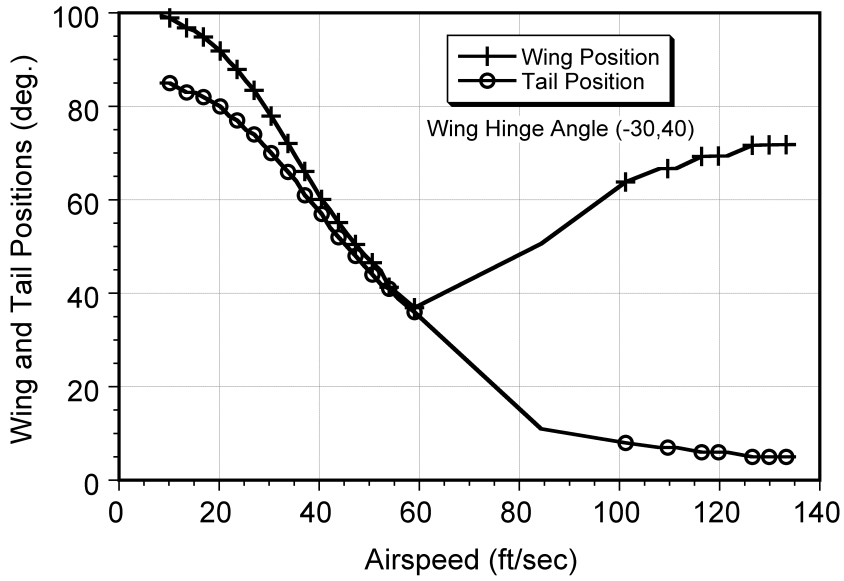

Figure A.9: Equilibrium positions of the wing and tail versus airspeed for wing hinge angle setting $(\phi_{\mathrm{H}}, \theta_{\mathrm{H}}) = (-30°, 40°)$.

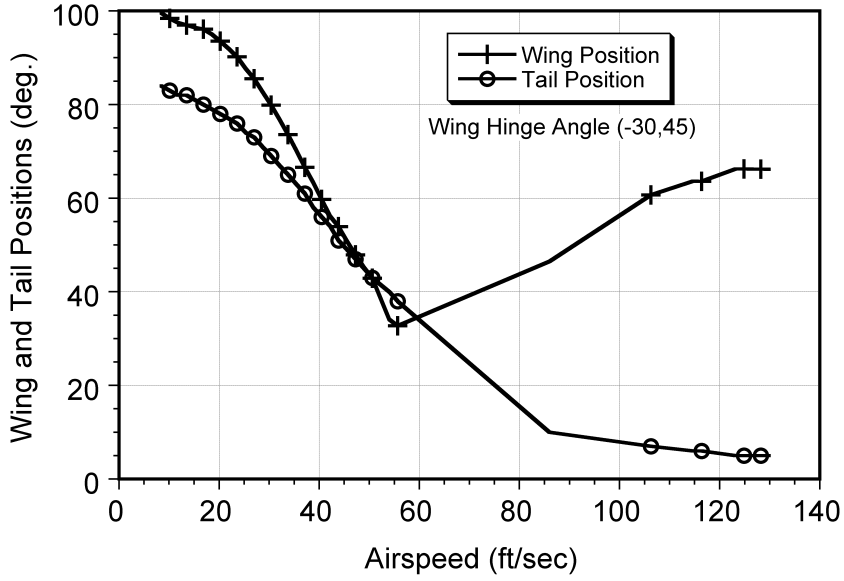

Figure A.10: Equilibrium positions of the wing and tail versus airspeed for wing hinge angle setting $(\phi_{\mathrm{H}}, \theta_{\mathrm{H}}) = (-30°, 45°)$.

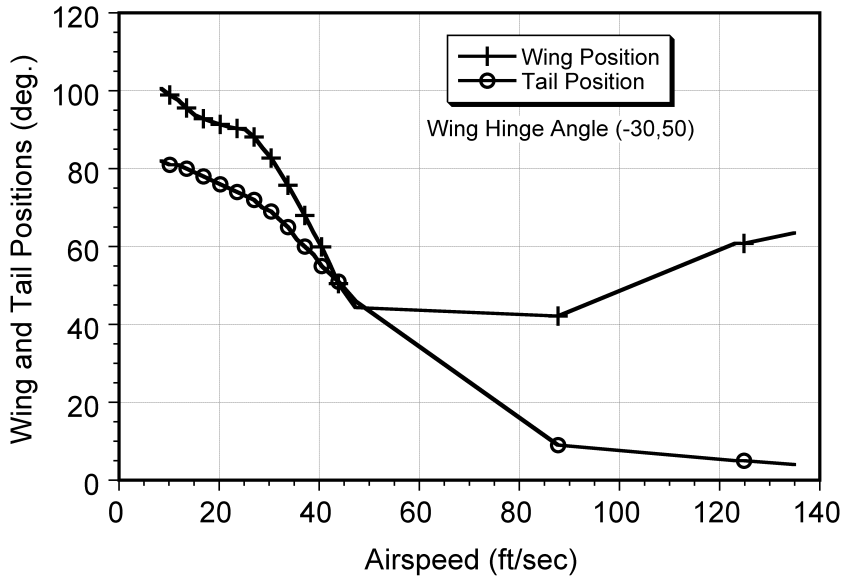

Figure A.11: Equilibrium positions of the wing and tail versus airspeed for wing hinge angle setting $(\phi_{\mathrm{H}}, \theta_{\mathrm{H}}) = (-30°, 50°)$.

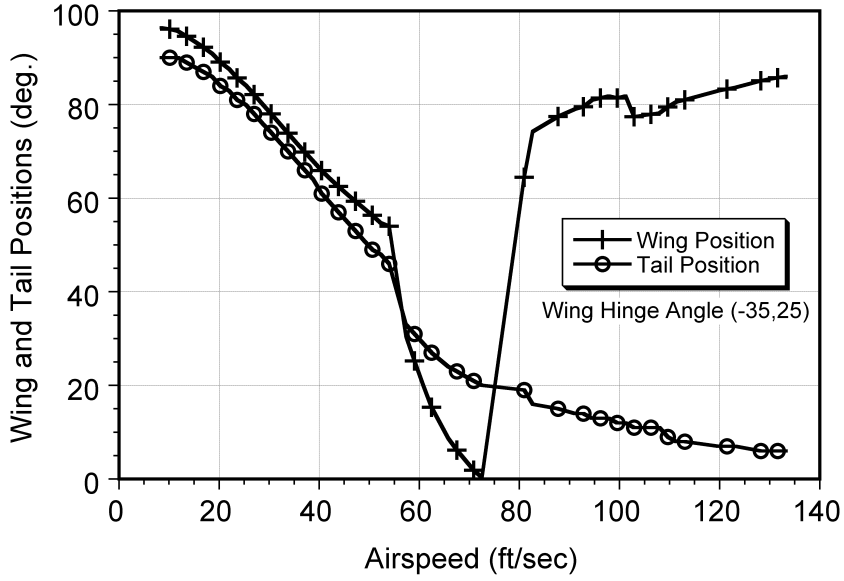

Figure A.12: Equilibrium positions of the wing and tail versus airspeed for wing hinge angle setting $(\phi_{\mathrm{H}}, \theta_{\mathrm{H}}) = (-35°, 25°)$.

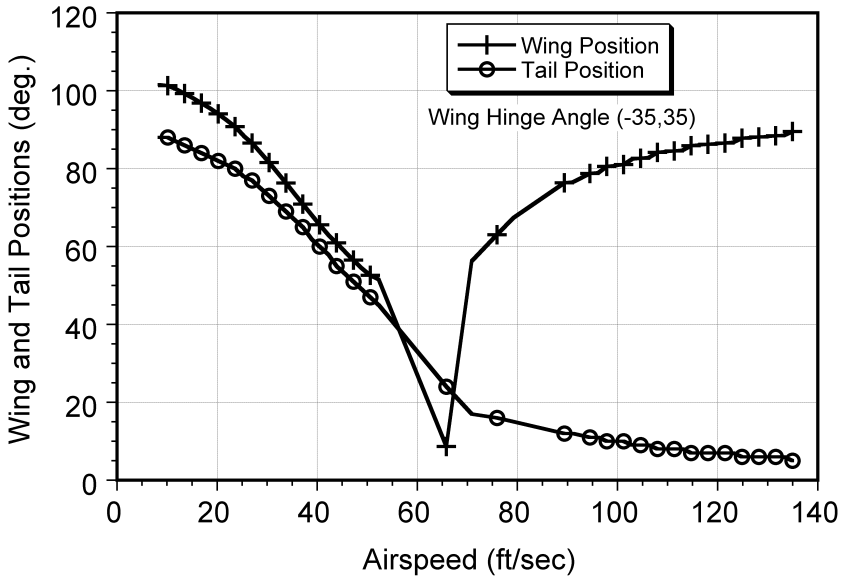

Figure A.13: Equilibrium positions of the wing and tail versus airspeed for wing hinge angle setting $(\phi_{\mathrm{H}}, \theta_{\mathrm{H}}) = (-35°, 35°)$.

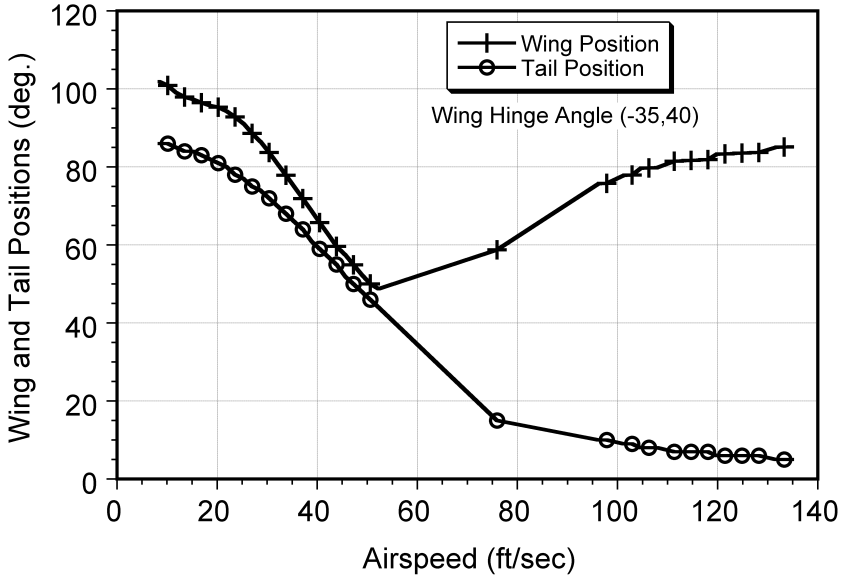

Figure A.14: Equilibrium positions of the wing and tail versus airspeed for wing hinge angle setting $(\phi_{\mathrm{H}}, \theta_{\mathrm{H}}) = (-35°, 40°)$.

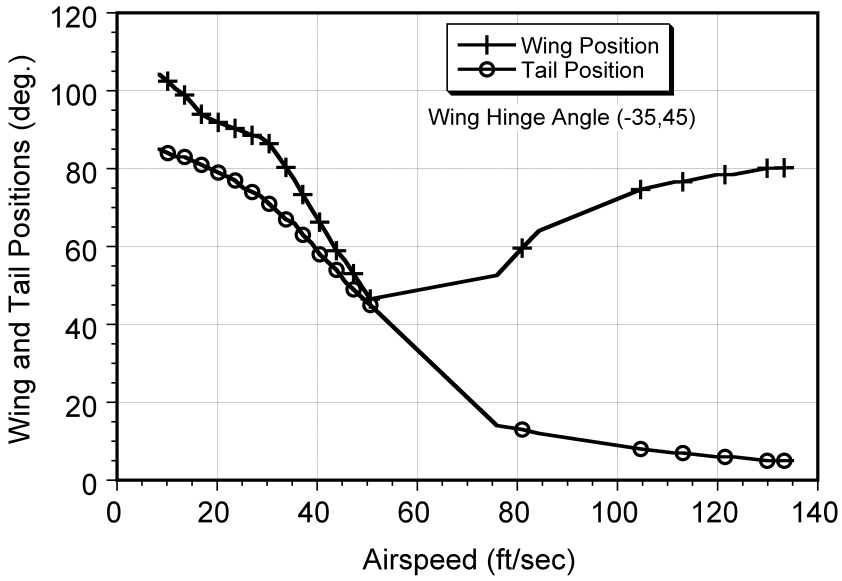

Figure A.15: Equilibrium positions of the wing and tail versus airspeed for wing hinge angle setting $(\phi_{\mathrm{H}}, \theta_{\mathrm{H}}) = (-35°, 45°)$.

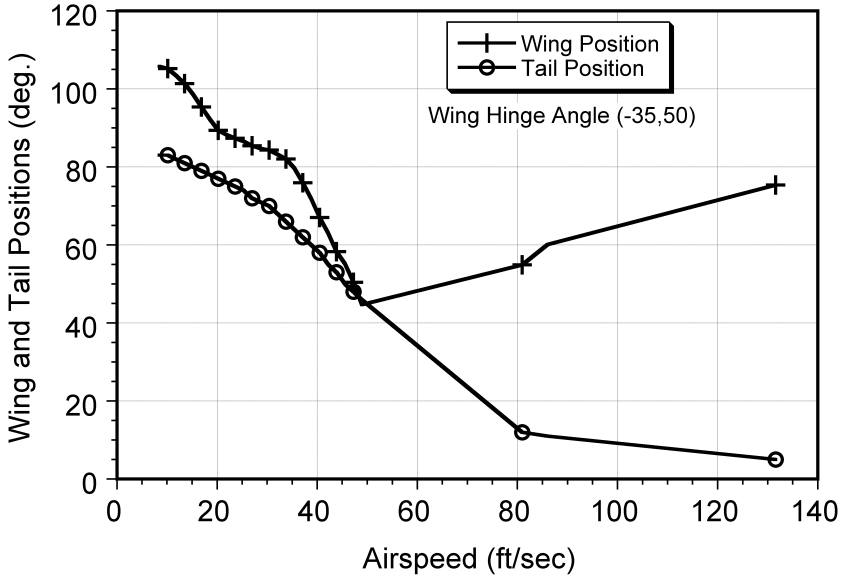

Figure A.16: Equilibrium positions of the wing and tail versus airspeed for wing hinge angle setting $(\phi_{\mathrm{H}}, \theta_{\mathrm{H}}) = (-35°, 50°)$.

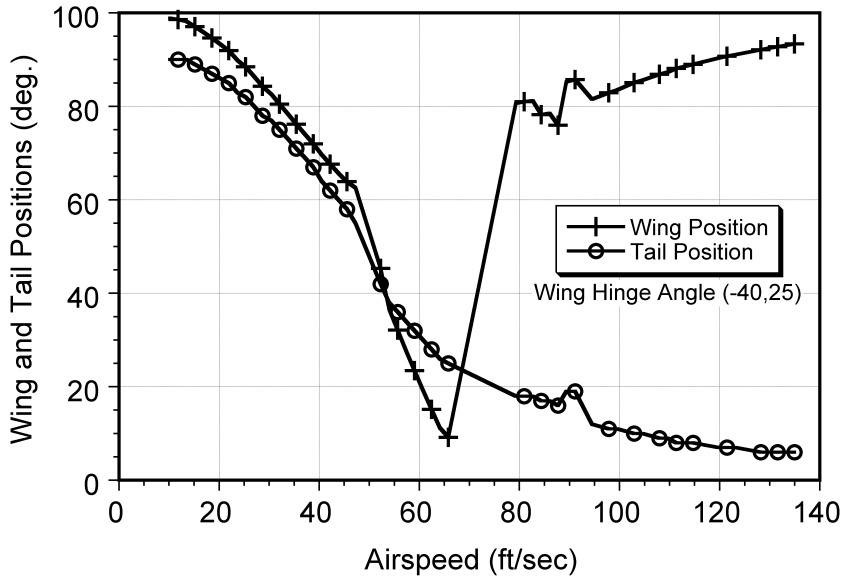

Figure A.17: Equilibrium positions of the wing and tail versus airspeed for wing hinge angle setting $(\phi_{\mathrm{H}}, \theta_{\mathrm{H}}) = (-40^{\circ}, 25^{\circ})$.

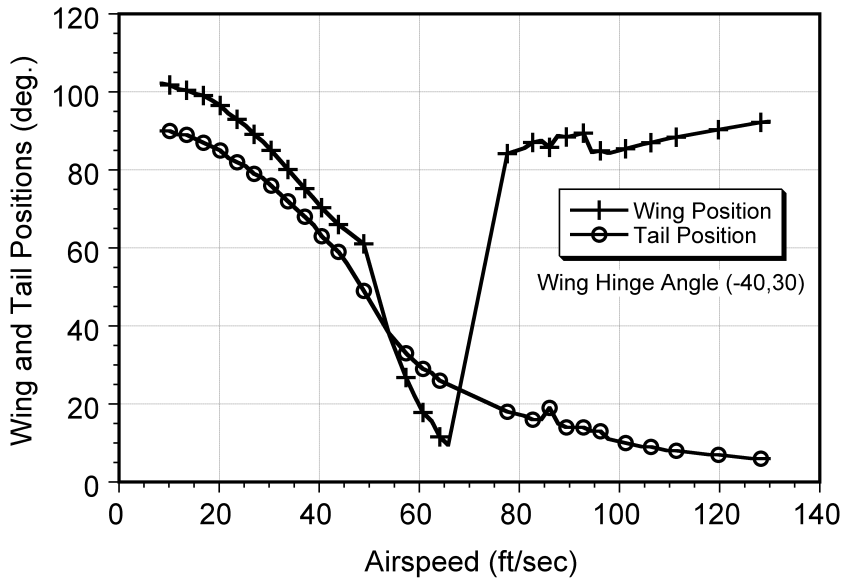

Figure A.18: Equilibrium positions of the wing and tail versus airspeed for wing hinge angle setting $(\phi_{\mathrm{H}}, \theta_{\mathrm{H}}) = (-40^{\circ}, 30^{\circ})$.

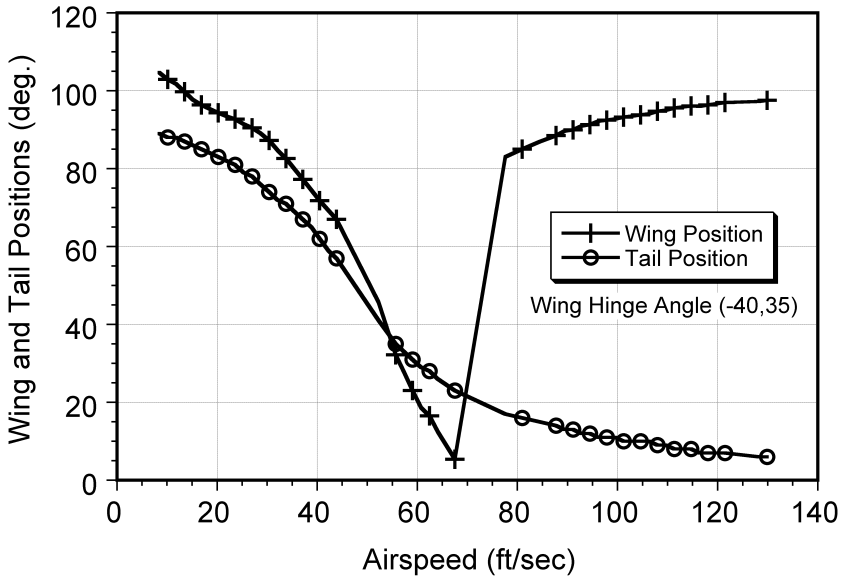

Figure A.19: Equilibrium positions of the wing and tail versus airspeed for wing hinge angle setting $(\phi_{\mathrm{H}}, \theta_{\mathrm{H}}) = (-40^{\circ}, 35^{\circ})$.

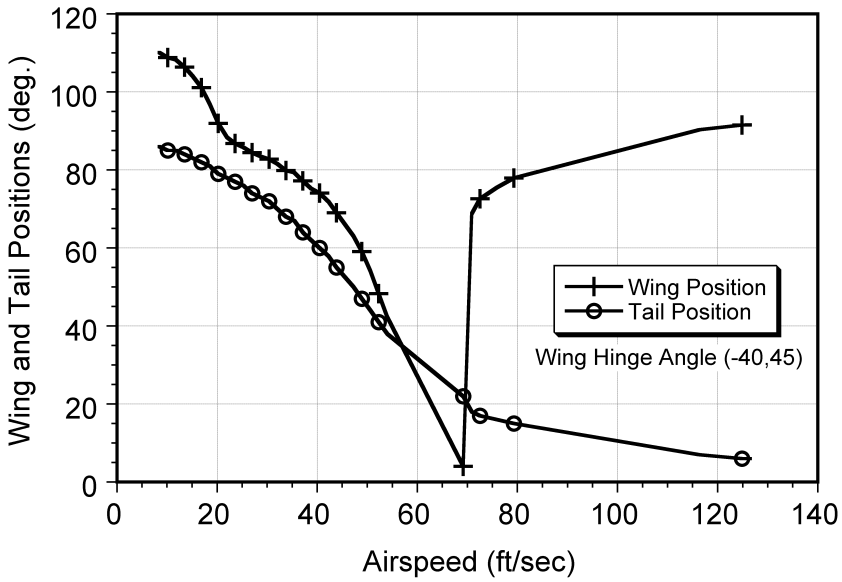

Figure A.20: Equilibrium positions of the wing and tail versus airspeed for wing hinge angle setting $(\phi_{\mathrm{H}}, \theta_{\mathrm{H}}) = (-40^{\circ}, 45^{\circ})$.

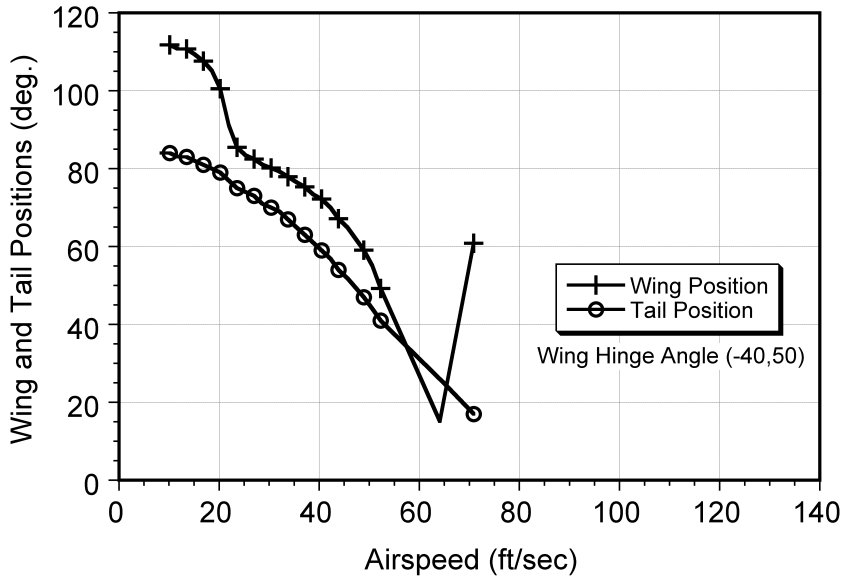

Figure A.21: Equilibrium positions of the wing and tail versus airspeed for wing hinge angle setting $(\phi_{\mathrm{H}}, \theta_{\mathrm{H}}) = (-40°, 50°)$.

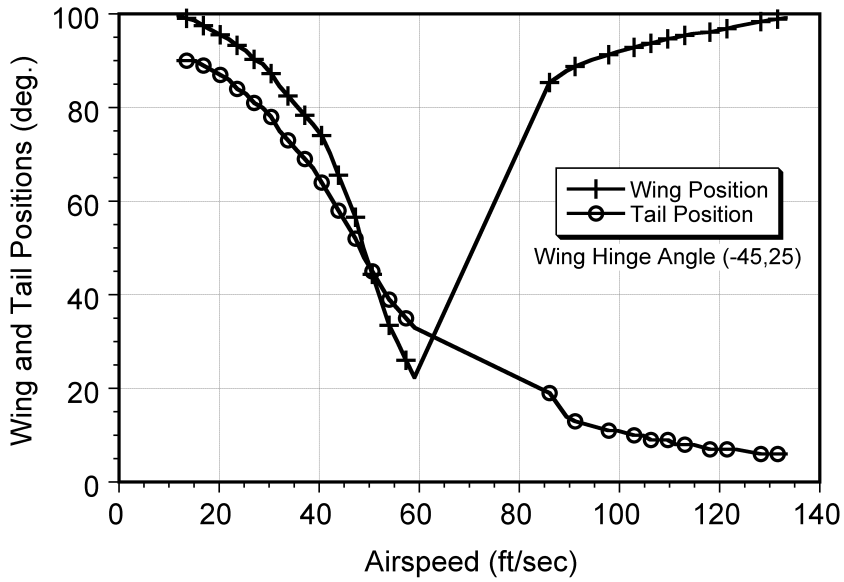

Figure A.22: Equilibrium positions of the wing and tail versus airspeed for wing hinge angle setting $(\phi_{\mathrm{H}}, \theta_{\mathrm{H}}) = (-45°, 25°)$.

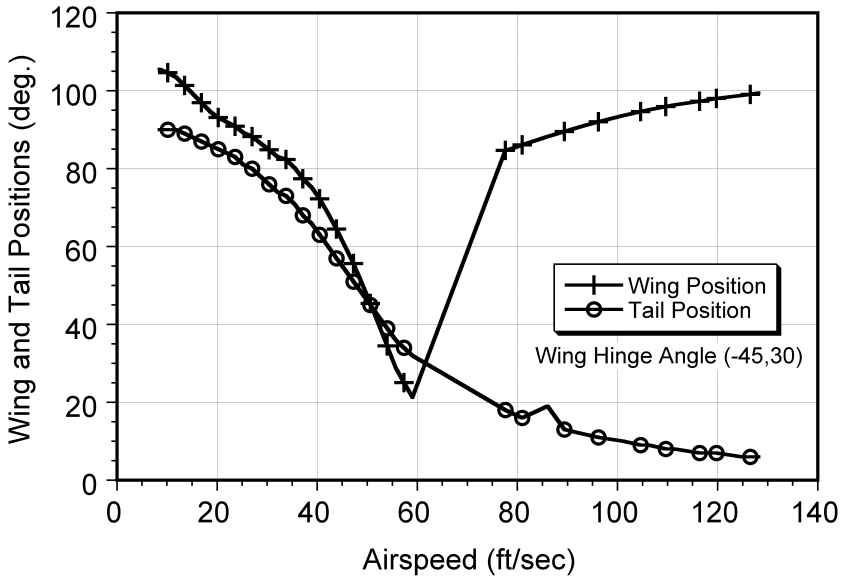

Figure A.23: Equilibrium positions of the wing and tail versus airspeed for wing hinge angle setting $(\phi_{\mathrm{H}}, \theta_{\mathrm{H}}) = (-45°, 30°)$.

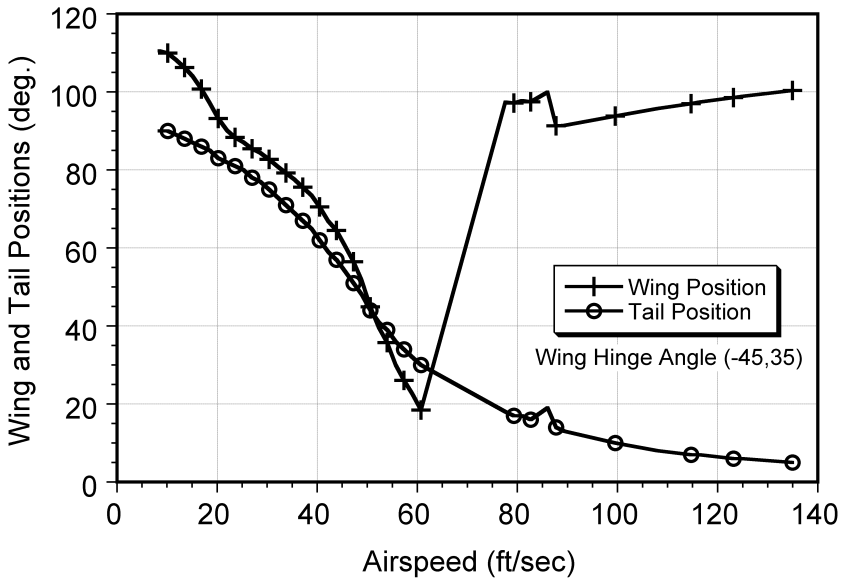

Figure A.24: Equilibrium positions of the wing and tail versus airspeed for wing hinge angle setting $(\phi_{\mathrm{H}}, \theta_{\mathrm{H}}) = (-45°, 35°)$.

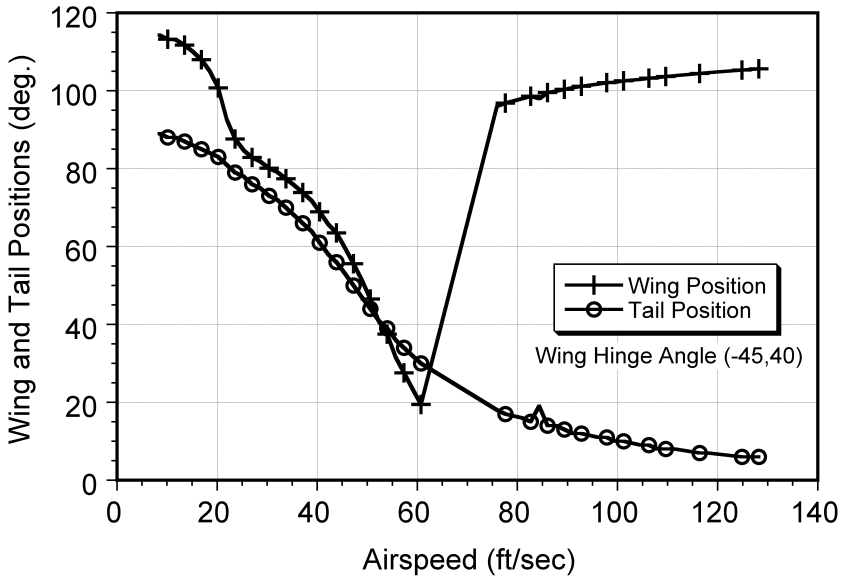

Figure A.25: Equilibrium positions of the wing and tail versus airspeed for wing hinge angle setting $(\phi_{\mathrm{H}}, \theta_{\mathrm{H}}) = (-45°, 40°)$.

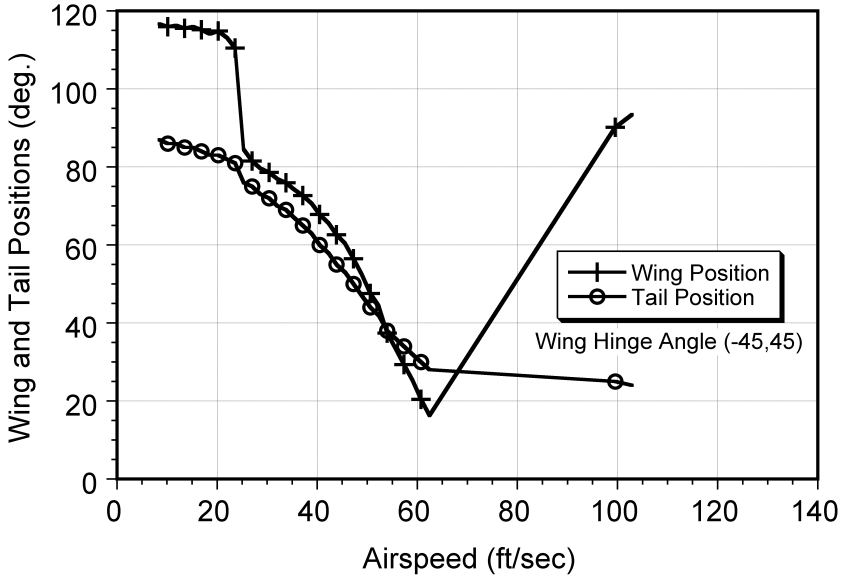

Figure A.26: Equilibrium positions of the wing and tail versus airspeed for wing hinge angle setting $(\phi_{\mathrm{H}}, \theta_{\mathrm{H}}) = (-45°, 45°)$.

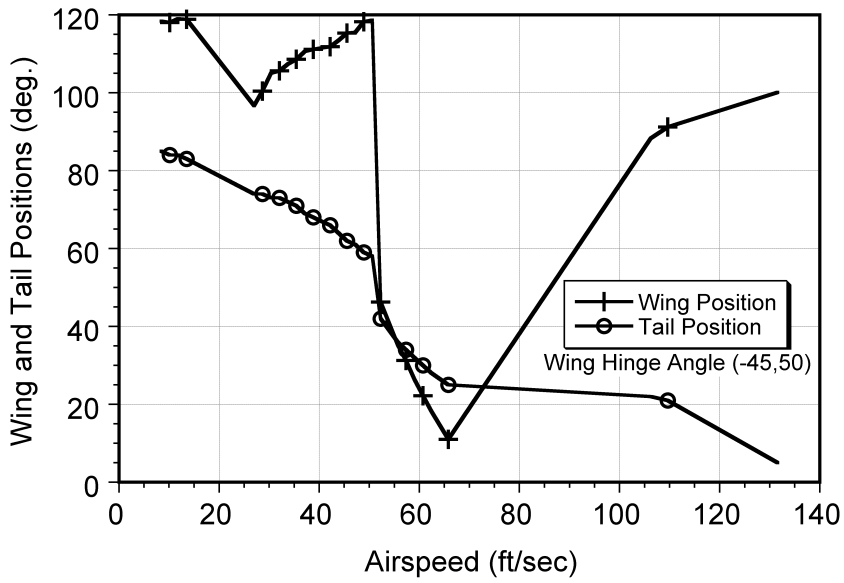

Figure A.27: Equilibrium positions of the wing and tail versus airspeed for wing hinge angle setting $(\phi_{\mathrm{H}}, \theta_{\mathrm{H}}) = (-45°, 50°)$.

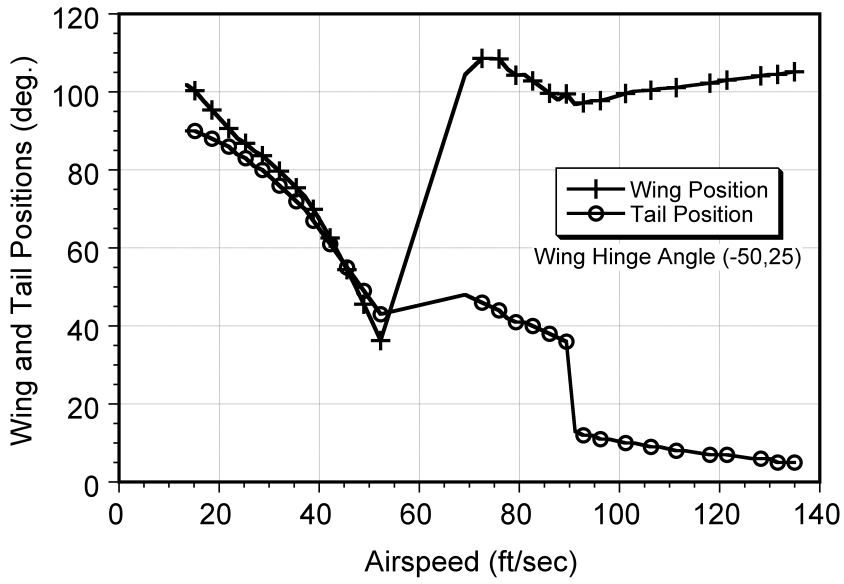

Figure A.28: Equilibrium positions of the wing and tail versus airspeed for wing hinge angle setting $(\phi_{\mathrm{H}}, \theta_{\mathrm{H}}) = (-50°, 25°)$.

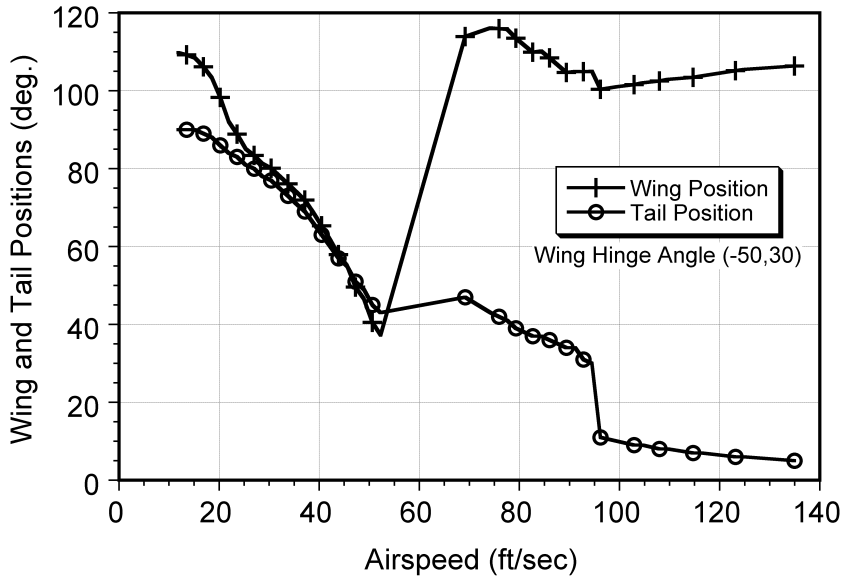

Figure A.29: Equilibrium positions of the wing and tail versus airspeed for wing hinge angle setting $(\phi_{\mathrm{H}}, \theta_{\mathrm{H}}) = (-50°, 30°)$.

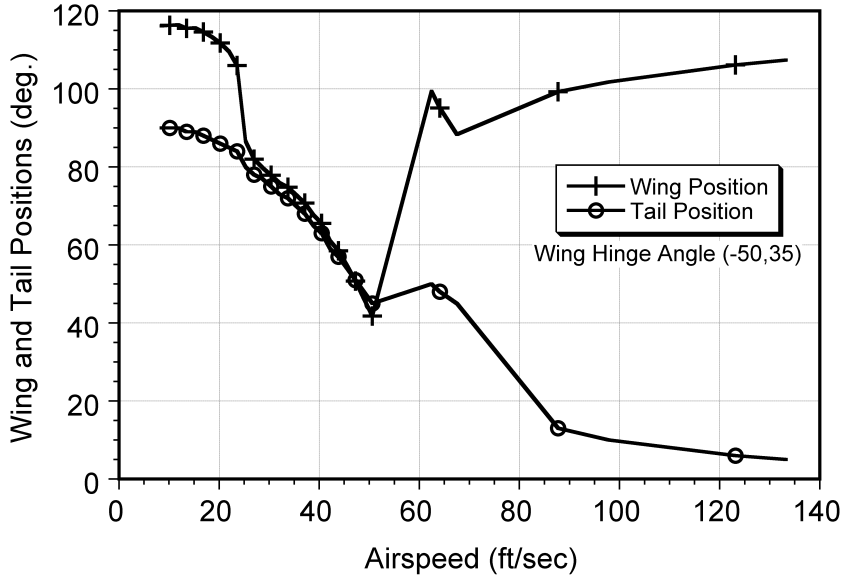

Figure A.30: Equilibrium positions of the wing and tail versus airspeed for wing hinge angle setting $(\phi_{\mathrm{H}}, \theta_{\mathrm{H}}) = (-50°, 35°)$.

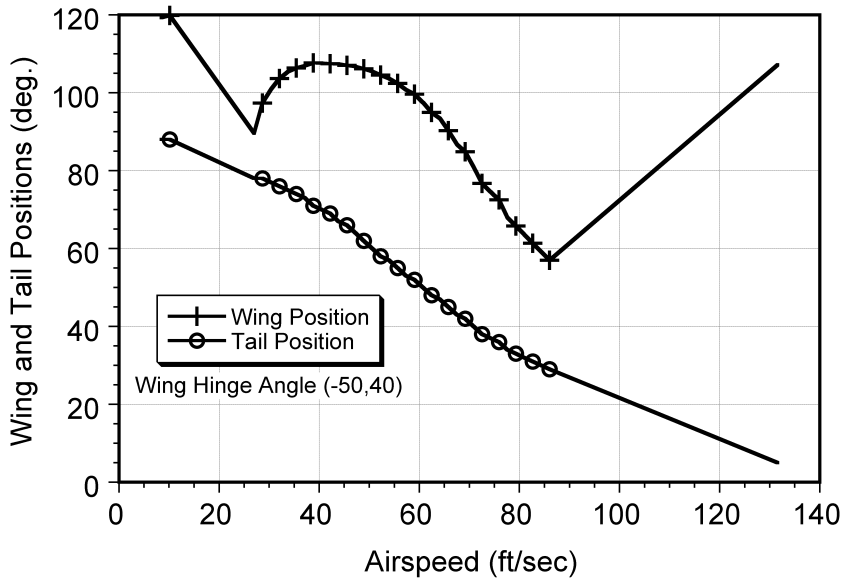

Figure A.31: Equilibrium positions of the wing and tail versus airspeed for wing hinge angle setting $(\phi_{\mathrm{H}}, \theta_{\mathrm{H}}) = (-50°, 40°)$.

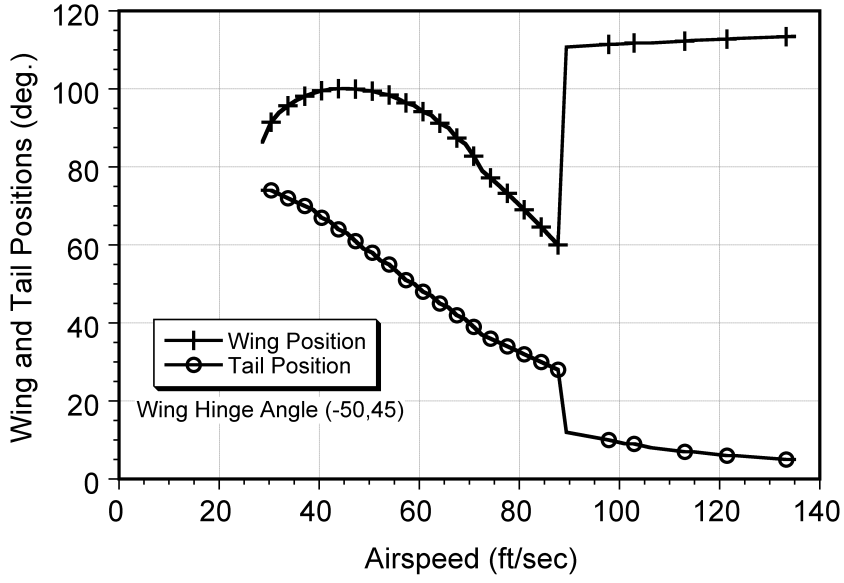

Figure A.32: Equilibrium positions of the wing and tail versus airspeed for wing hinge angle setting $(\phi_{\mathrm{H}}, \theta_{\mathrm{H}}) = (-50°, 45°)$.

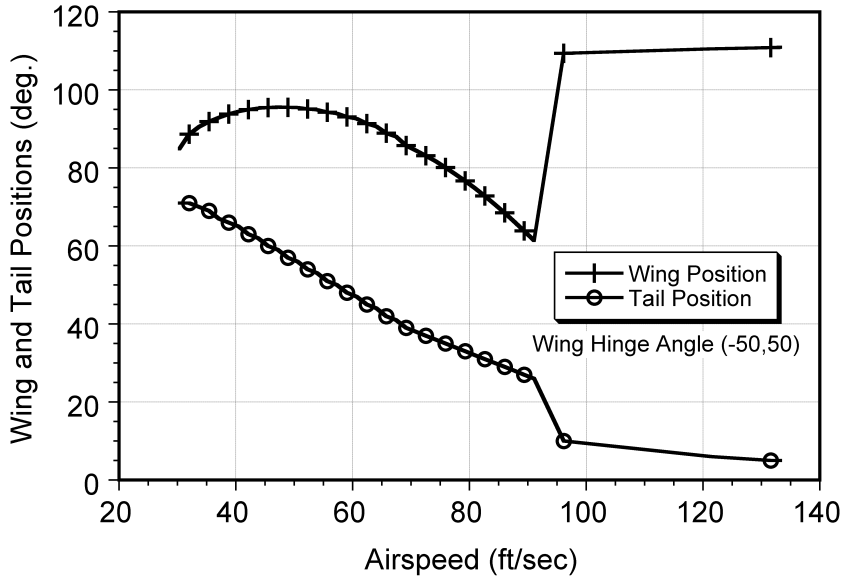

Figure A.33: Equilibrium positions of the wing and tail versus airspeed for wing hinge angle setting $(\phi_{\mathrm{H}}, \theta_{\mathrm{H}}) = (-50^{\circ}, 50^{\circ})$.

Appendix B

Additional Lift, Drag and Moment Plots

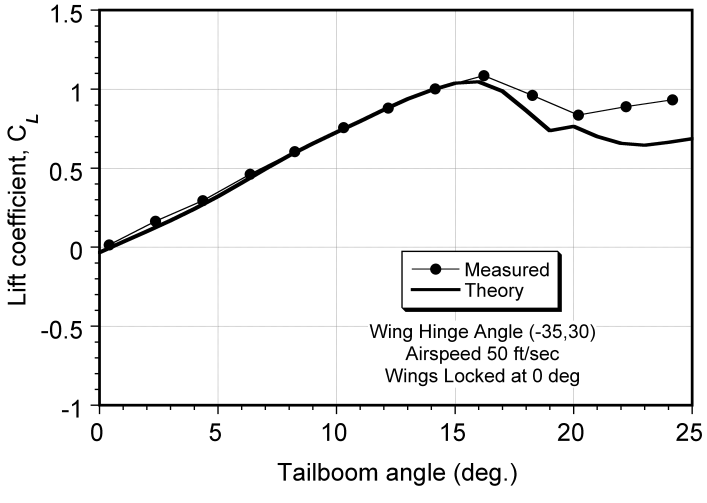

(a)

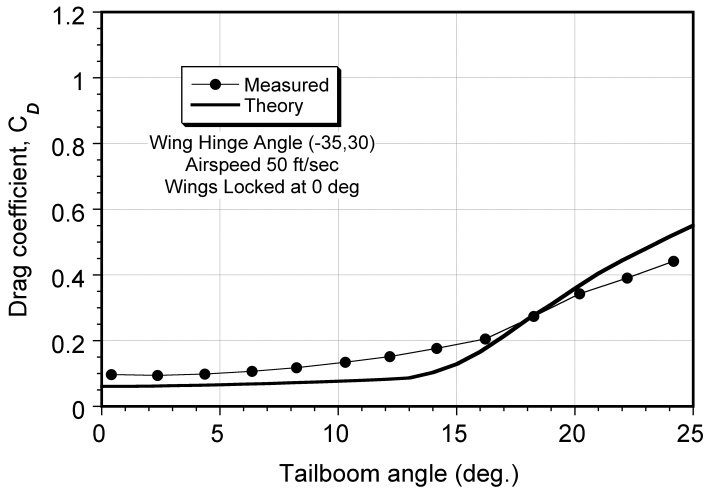

(b)

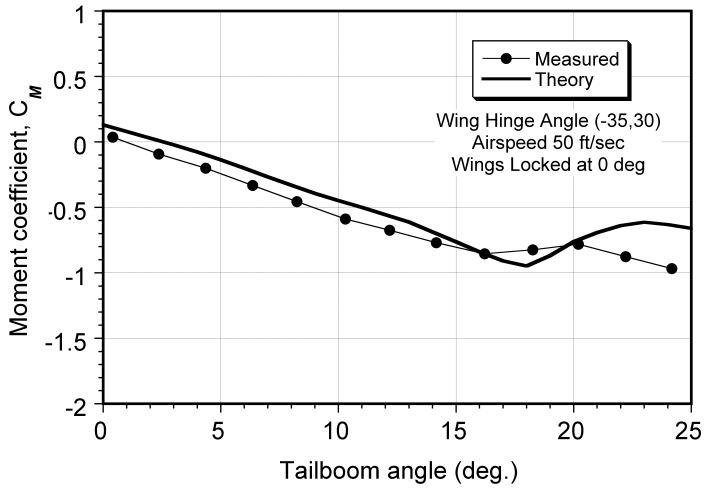

(c)

Figure B.1: Lift, drag and pitching moment versus tail boom position. Wings locked at 0°, wing hinge angle $(\phi, \theta) = (-35°, 30°)$

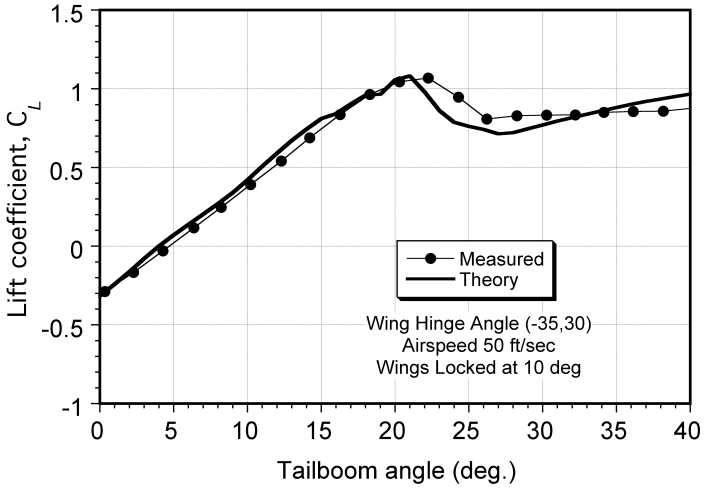

(a)

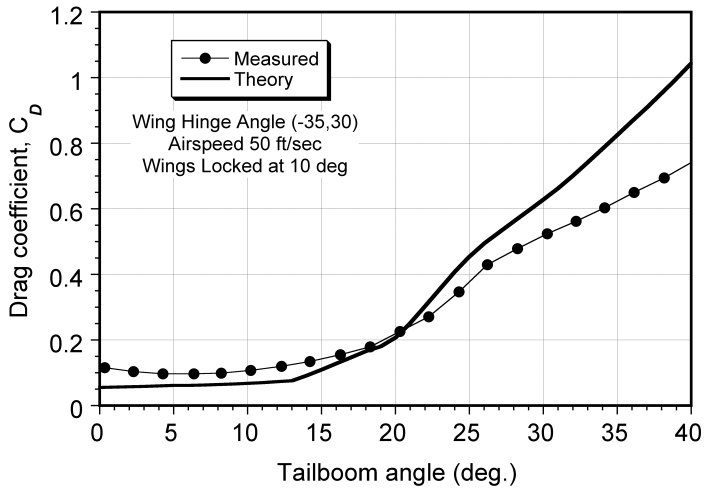

(b)

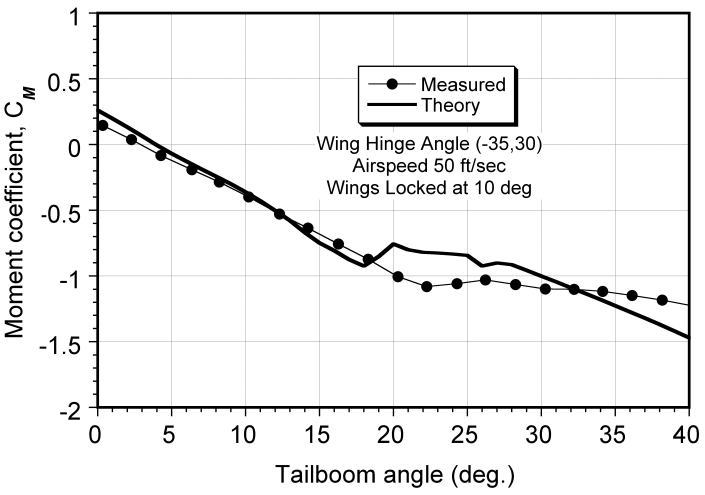

(c)

Figure B.2: Lift, drag and pitching moment versus tail boom position. Wings locked at 10°, wing hinge angle $(\phi, \theta) = (-35°, 30°)$

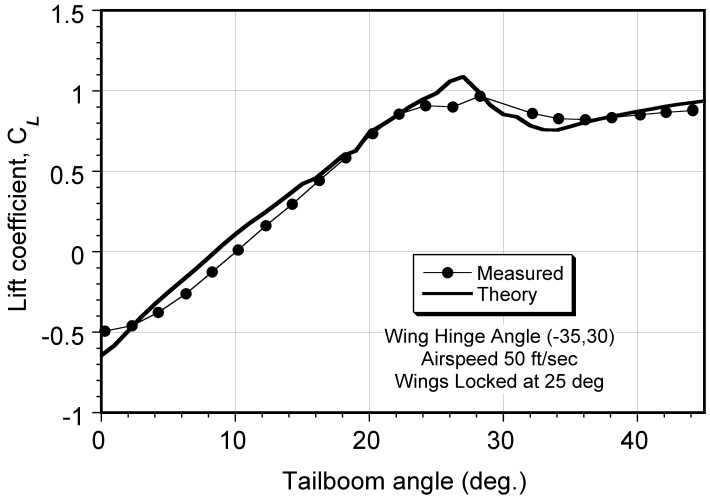

(a)

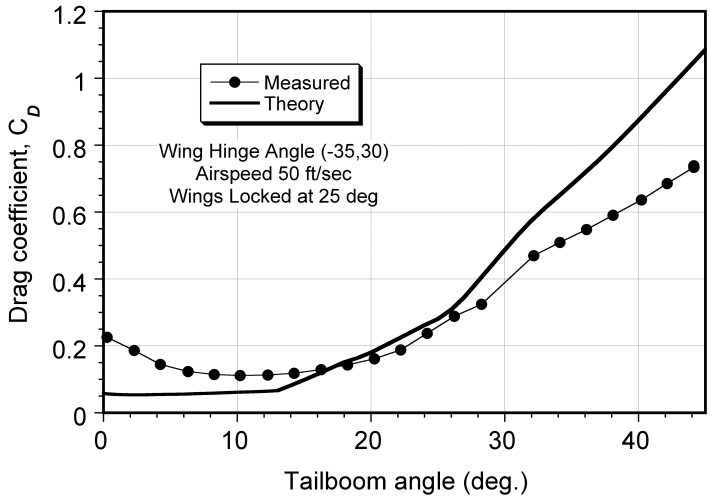

(b)

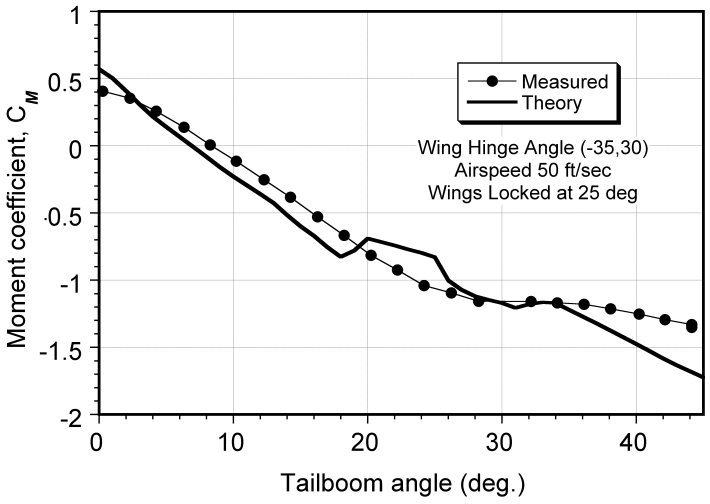

(c)

Figure B.3: Lift, drag and pitching moment versus tail boom position. Wings locked at 25°, wing hinge angle $(\phi, \theta) = (-35°, 30°)$

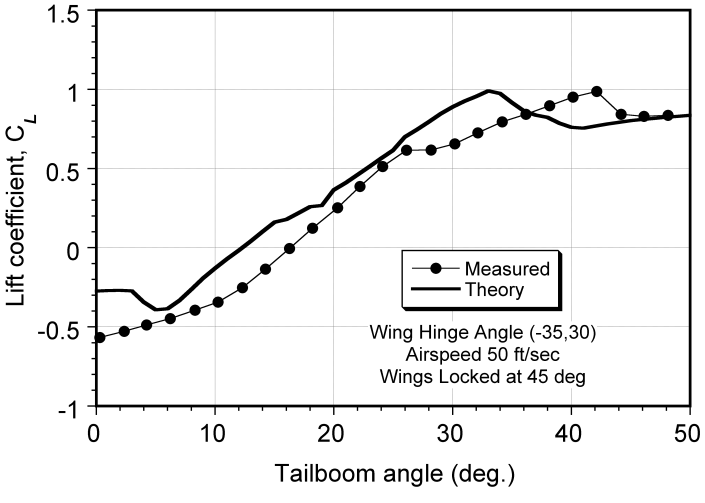

(a)

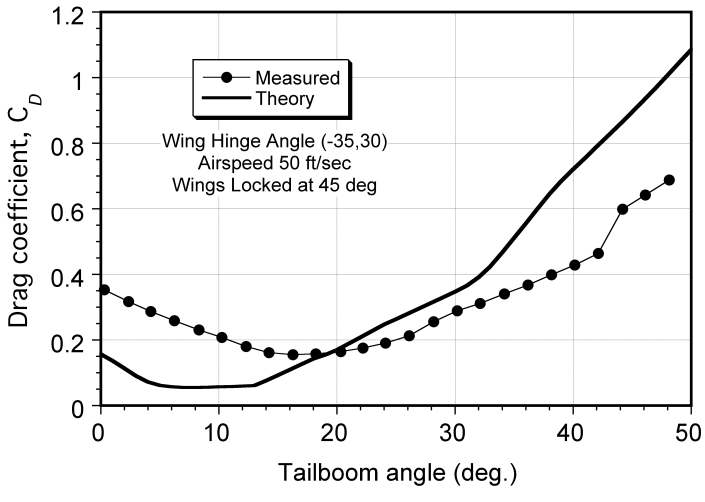

(b)

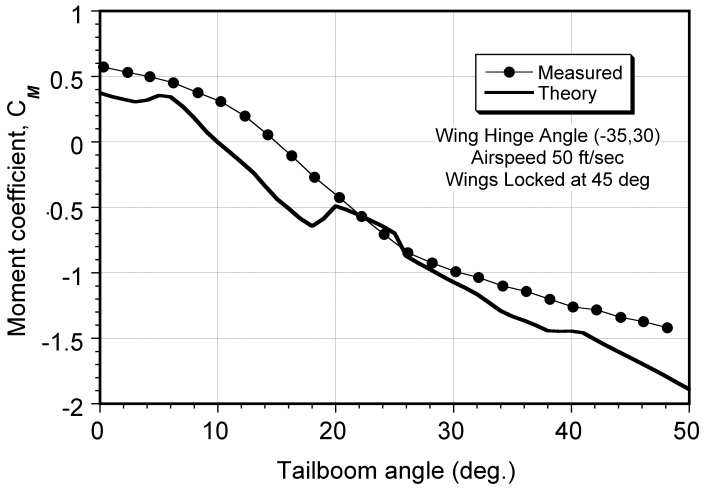

(c)

Figure B.4: Lift, drag and pitching moment versus tail boom position. Wings locked at 45°, wing hinge angle $(\phi, \theta) = (-35°, 30°)$

Appendix C
Hermite Interpolation Polynomials

The term η can be defined as

$$\eta = \frac{x}{\ell} \tag{C.1}$$

where x is the distance from the inboard (left-side) of the element to a point inside the element, and ℓ is the total length of the element.

The Hermite interpolation polynomial used in calculating the out of plane and in plane bending displacements is

$$H_v(x_e) = H_w(x_e) = \left\{ \begin{array}{c} 1 - 3\eta^2 + 2\eta^3 \\ \eta(1 - 2\eta + \eta^2)\ell \\ 3\eta^2 - 2\eta^3 \\ \eta(-\eta + \eta^2)\ell \end{array} \right\} \tag{C.2}$$

The Hermite interpolation polynomial used in calculating the out of plane and in plane bending slopes is

$$H_{v,x}(x_e) = H_{w,x}(x_e) = \frac{1}{\ell} \left\{ \begin{array}{c} -6\eta + 6\eta^2 \\ (1 - 4\eta + 3\eta^2)\ell \\ 6\eta - 6\eta^2 \\ (-2\eta + 3\eta^2)\ell \end{array} \right\} \tag{C.3}$$

The Hermite interpolation polynomial used in calculating the out of plane and in plane bending moments is

$$H_{v,xx}(x_e) = H_{w,xx}(x_e) = \frac{1}{\ell^2}\begin{Bmatrix} -6+12\eta \\ (-4+6\eta)\ell \\ 6-12\eta \\ (-2+6\eta)\ell \end{Bmatrix} \tag{C.4}$$

The Hermite interpolation polynomial used in calculating the axial displacement and torsional angular displacement is

$$H_u(x_e) = H_\phi(x_e) = \begin{Bmatrix} 1-3\eta+2\eta^2 \\ 4\eta-4\eta^2 \\ -\eta+2\eta^2 \end{Bmatrix} \tag{C.5}$$

The Hermite interpolation polynomial used in calculating the axial force and torsional moment is

$$H_u, x(x_e) = H_{\phi,x}(x_e) = \frac{1}{\ell}\begin{Bmatrix} -3+4\eta \\ 4-8\eta \\ -1+4\eta \end{Bmatrix} \tag{C.6}$$

A vector corresponding to an elements local nodal degrees of freedom for out of plane bending displacements and slopes is defined as

$$y_v = \begin{Bmatrix} v_L \\ v_{xL} \\ v_R \\ v_{xR} \end{Bmatrix} \tag{C.7}$$

A vector corresponding to an elements local nodal degrees of freedom for in plane bending displacements and slopes is defined as

$$y_w = \begin{Bmatrix} w_L \\ w_{xL} \\ w_R \\ w_{xR} \end{Bmatrix} \tag{C.8}$$

A vector corresponding to an elements local nodal degrees of freedom for axial displacements is

$$y_u = \begin{Bmatrix} u_L \\ u_C \\ u_R \end{Bmatrix} \tag{C.9}$$

A vector corresponding to an elements local nodal degrees of freedom for torsional angular displacements is

$$y_\phi = \begin{Bmatrix} \phi_L \\ \phi_C \\ \phi_R \end{Bmatrix} \tag{C.10}$$

The out of plane bending displacement for a point on an element can be defined by

$$v(x_e) = H_v(x_e) y_v \tag{C.11}$$

The out of plane bending slope for a point on an element can be defined by

$$v_{,x}(x_e) = H_{v,x}(x_e)y_v \tag{C.12}$$

The out of plane bending moment for a point on an element can be defined by

$$M_v(x_e) = EI_2H_{v,xx}(x_e)y_v \tag{C.13}$$

The in plane bending displacement for a point on an element can be defined by

$$w(x_e) = H_w(x_e)y_w \tag{C.14}$$

The in plane bending slope for a point on an element can be defined by

$$w_{,x}(x_e) = H_{w,x}(x_e)y_w \tag{C.15}$$

The in plane bending moment for a point on an element can be defined by

$$M_w(x_e) = EI_3H_{w,xx}(x_e)y_w \tag{C.16}$$

The axial displacement for a point on an element can be defined by

$$u(x_e) = H_u(x_e)y_u \tag{C.17}$$

The axial force for a point on an element can be defined by

$$F_u(x_e) = EAH_{u,x}(x_e)y_u \tag{C.18}$$

The torsional angular displacement for a point on an element can be defined by

$$\phi(x_e) = H_\phi(x_e) y_\phi \tag{C.19}$$

The torsional moment for a point on an element can be defined by

$$M_\phi(x_e) = GJH_{\phi,x}(x_e) y_\phi \tag{C.20}$$

Bibliography

[1] Gillmore, K. B., Schneider, J. J., "Design Considerations of the Heavy Lift Helicopter," *Journal of the American Helicopter Society*, Vol. 8, No. 1, 1963, pp. 31–37.

[2] Wax, C. M. and Torci, R. C., "Study of the Heavy-Lift Helicopter Rotor Configuration," USAAVLABS Technical Report 66-61, Nov. 1966.

[3] Schneider, J. J., "The Influence of Propulsion Systems on Extremely Large Helicopter Design," *Journal of the American Helicopter Society*, Vol. 15, No. 1, Jan. 1970.

[4] Schneider, J. J., "The Developing Technology and Economics of Large Helicopters," Paper No. 3, Proceedings of the Sixth European Rotorcraft and Powered Lift Aircraft Forum, Bristol, England, Sept. 16–18, 1980.

[5] Schrage, D.P., Costello, M. F., Mittlevden, D. N., "Design Concepts for an Advanced Cargo Rotorcraft," Paper AIAA-88-4496, Proceedings of the AIAA/AHS/ASEE Aircraft Design, Systems and Operations Meeting, Atlanta, Georgia, Sept. 1988.

[6] Preator, R., Leishman, J. G., and Baldwin, G. D., "Performance and Trade Studies of Mono Tiltrotor Design," Proceedings of the 61st Annual Forum of the American Helicopter Society International, Grapevine, TX, June 1–3, 2005.

[7] Preator, R., Leishman, J. G., and Baldwin, G. D., "Conceptual Design Studies of a Mono Tiltrotor (MTR) Architecture," Proceedings of the 60th Annual Forum of the American Helicopter Society International, Baltimore, MD, June 7–11, 2004.

[8] Preator, R., "Conceptual Design Studies Of A Mono Tiltrotor," Masters Thesis, University of Maryland, College Park, Maryland, September 2005.

[9] Pamadi, B., *Performance, Stability, Dynamics, and Control of Airplanes*, America Institute of Aeronautics and Astronautics, Inc., Virgina, 2004, pp. 50, 324–332.

[10] Hibbeler, R.C., *Dynamics*, Prentice-Hall, New Jersey, 2001, pp. 354–358, 386–388.

[11] Leishman, J.G., *Principles of Helicopter Aerodynamics*, Cambridge University Press, New York, 2000, pp. 323–326.

[12] Hoerner, S., *Fluid Dynamic Drag*, Hoerner Fluid Dynamics, Vancouver, WA, 1965.

[13] Sharf, I., Gilardi, G., Crawford, C., "Identification of Friction Coefficient for Constrained Robotic Tasks," *Journal of Dynamic Systems, Measurement, and Control*, Vol. 124, No. 4, 2002, pp. 529–538.

[14] Meirovitch, L. *Fundamentals of Vibrations*, McGraw-Hill International, New York, 2001, pp. 549–612.

[15] Celi, R., Fusato, D., and Guhlieri, G., "Fligh Dynamics of an Articulated Rotor Helicopter with an External Slung Load" *Journal of American Helicopter Society*, Vol. 46, Jan. 2001.

[16] Poli, C., and Cromack, D., "Dynamics of Slung Bodies Using a Single-Point Suspension System," *Journal of Aircraft*, Vol. 10, (2), Feb. 1973.

[17] Cliff, E. M., and Bailey, D. B., "Dynamic Stability of a Translating Vehicle with a Simple Sling Load, " *Journal of Aircraft*, Vol. 12, (10), Oct. 1975.

[18] B.B., "Low-Speed Stability Characteristics of a Helicopter With a Sling Load," *Vertica*, Vol. 9, 1985.

[19] Cicolani *et. al*, Proceedings of the 62nd Annual Forum of the American Helicopter Society International, Phoenix, AZ, May 2006.

[20] Meirovitch, L. *Fundamentals of Vibrations*, McGraw-Hill International, New York, 2001, pp. 549–612.